Control of Structures and Electronic States in Self-assembled Multinuclear Complexes

Hiroki Sato

February 2016

Control of Structures and Electronic States in Self-assembled Multinuclear Complexes

Hiroki Sato

Doctoral Program in Nano-Science and Nano-Technology

Submitted to the Graduate School of
Pure and Applied Sciences
in Partial Fulfillment of the Requirement
for the Degree of Doctor of Philosophy in
Science

at the
University of Tsukuba

INDEX

CHAPTER 1

General Introduction

1.1 Aim of This Thesis

Chemistry has considerably contributed to human life, and developments of chemistry will give fruitful social life. Especially, the research and development of advanced functional molecular materials is a burgeoning field, with significant innovations contributing to all aspects of modern life. In early times, inorganic compounds were the center of research in functional materials. However, in recent decades, coordination compounds have increasingly been the focus of study for the development of advanced materials, due their inherent capacity for compositional control, tunable physical properties and relative ease of construction; traits accessed through the considered combination of inorganic and organic moieties. Complexes consisting of transition metal ions and organic ligands can show unique physical characteristics, such as molecular magnetism, electric conductivity, dielectric response and unusual optical behavior, properties which can be difficult to access in pure inorganic and organic compounds.[1] These physical properties of metal complexes can be controlled by careful molecular design. Due to their designability and tunability, metal complexes attract attention in complimentary research fields, such as quantum physics, spintronics, and enzymology.

In particular, multinuclear metal complexes, in which metal ions are arranged in close proximity, can show unique physical properties and cooperative functions owing to their intermetallic interactions. For example, there are multinuclear metal complexes with bistability based on electron transfer between neighboring metal ions, which show several stable states, accessible through the application of external stimuli, such as light or temperature. These compounds may have applications as molecular devices and switches. In addition, multinuclear metal complex centers in enzymes can act as effective reaction sites for small molecule conversions, functionality based on the synergistic interaction of metal ions, ligands and substrate. In order to build such molecular devices and functional molecular catalysts, it is critical that molecular systems have desirable, ordered arrangements of metal ions and controllable structures and electronic states.

Controlling the range of interactions and driving forces that play a role in cluster synthesis is a key goal in coordination chemistry. Self-assembly methods can be a very effective technique for the construction of higher order structures, and many multinuclear complexes and high-dimensional network coordination compounds have been reported. In section 1.2, well-known self-assembled multinuclear complexes are introduced. Hetero-metallic complexes are one of the important classes of functional materials due to their interactions between neighboring metal ions and the cooperative effects of different metal ions. Some enzymes have specific reaction sites, the particular reactivities of which are directly dependent on their unique combination of different metal ions. Likewise, tailored combinations of transition metal ions can allow chemists to access new classes of magnetic materials, whose electronic structure is derived from their constituents. Although hetero-metallic systems are important for their molecular functionality, rational synthetic methods are not well established, albeit that many different approaches to the synthesis of hetero-metallic multinuclear complexes have been reported. In section 1.3, some examples of hetero-metallic complexes and their synthetic strategies are described. Among self-assembled systems, grid-type molecules are a highly attractive class of compound, from the viewpoint of specific structures and unique physical properties. In section 1.4, recent results obtained from multinuclear grid systems and their applications are presented. In general, research into the physical properties of multinuclear complexes, where such properties are based on intermetallic interactions and cooperative effects, is a very important area of work. Well-

designed multinuclear systems show specific properties such as magnetism, optical properties, permittivity, conductivity, electrochemistry, catalytic reactions, and host-guest chemistry. In section 1.5 and 1.6, mixed-valence phenomena and multi-step spin-crossover phenomena are introduced, respectively.

In this study, grid-type compounds were selected for the construction of multinuclear molecular grids, which have potentially manipulable structures and electronic states. In order to develop functional compounds with specific physical properties, the electronic and magnetic interactions between metal ions in the grid molecules should be precisely controlled. In this research, grid-type complexes with a polypyridine multidentate ligand have been selected for the construction of self-assembled functional molecules, which have homo and hetero-metal grid structures and exhibit specific physical properties (both magnetic and electrochemical). Below this CHAPTER more details about the self-assembled systems of multinuclear metal complexes (CHAPTER 1.2), assembly and arrangement of hetero-metal ions (CHAPTER 1.3) and physical properties and potential applications of the grid-type complexes (CHAPTER 1.4) are presented

1.2 Self-Assembled Multinuclear Complexes

Multinuclear complexes may show unique magnetic and electrochemical properties based on their structures and electronic states[2] and it is expected that these complexes may have application in functional materials[3] and molecular catalysts.[4] While the use of appropriate bridging ligands is required to synthesize such assembled metal complexes, previous methods using simple bridging ligands like flexible alkoxide and acetate ions are difficult to control and thus forecast the structure.[5] Based on this background, development of effective synthetic methods towards an ordered arrangement of metal ions is important for the development of functional molecular devices.[6]

Self-assembly is one of the approaches, which enables us to make accurate arrangements of metal ions in a molecule. Major driving forces for self-assembly are coordination bonds, which allow for some degree of flexibility in the design of molecules.[7] Pioneering examples were reported by J. M. Lehn, *et al.* and other research groups.[8] Double or triple helical complexes were constructed by polypyridine ligands and metal ions. Reasonable selection of metal ions and bridging ligands leads various structures as shown in Figure 1.1.[9] Pd (II) ions and Pt (II) ions display square planar coordination geometry of which *cis* coordination positions make a coordination angle of about 90°. M. Fujita, *et al.* reported many coordination architectures by using the Pd(II) complex units.[10] An M_6L_4 octahedral complex (Figure 1.2.)[11] and M_4L_6 tetrahedral complex[12] have been studied for guest molecule recognition and catalytic ability of their void space.[13] Moreover, cube-type complexes[14] and triangular prism shaped complexes[15] were reported. Molecular wire type complexes, in which metal ions were arranged linearly, were constructed with multidentate ligands binding in the trans positions of transition metals at an angle of approx. 180° (Figure 1.3.).[16]

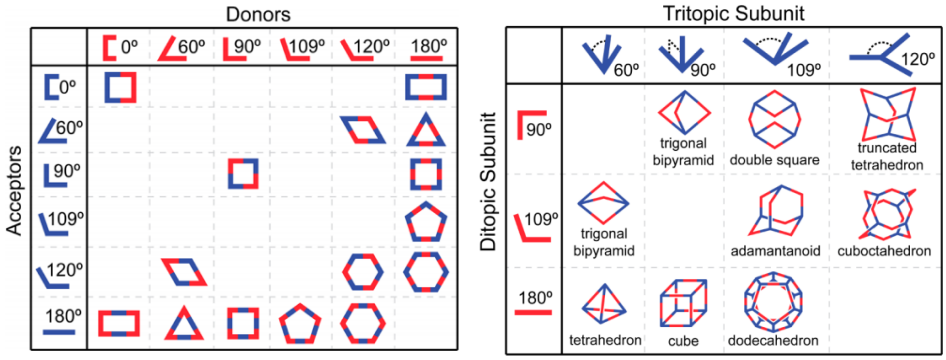

Figure 1.1. The expected various structure based on the combination with metal ions and bridging ligands. (left: 2D polygons, right: 3D polygons)

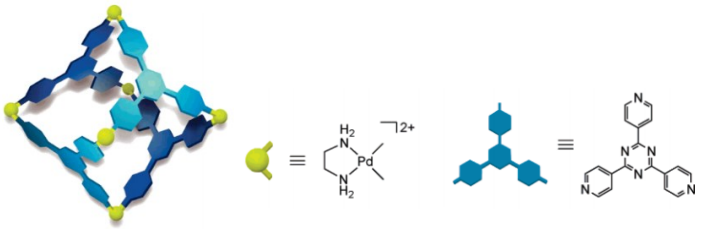

Figure 1.2. M_6L_4 caged complex.

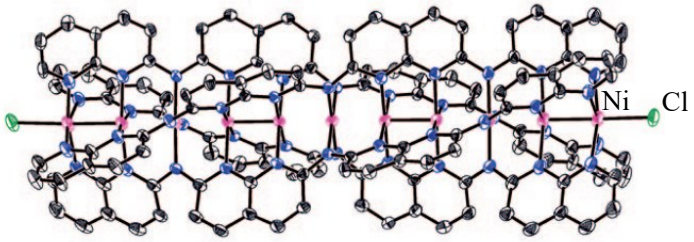

Figure 1.3. molecular wire.

1.3 Hetero-Metallic Systems

Hetero-metal complexes[17], which include more than two types of metal ions in one complex, show unique physical properties based on the specific interactions between hetero-metal ions. For example, a Mn-Cu dinuclear complex, $[Mn^{III}Cu^{II}Cl(5\text{-Br-sap})_2(MeOH)]$ (5-Br-sap = 5-bromo-2-salicylideneamino-1-propanol) shows ferromagnetic interactions between metal ions and single-molecule magnet (SMMs) behavior because of interactions between the different magnetic orbitals (Figure 1.4. (a), (b)).[18] On the other hand, a thiolate-bridged Fe-Ni dinuclear complex, $(PPh_4)[(CO)_2(CN)_2Fe(\mu\text{-pdt})Ni(S_2CNEt_2)]$ (pdt = 1,3-propanedithiolate), is a research target for understanding the hydrogenase enzyme which catalyzes the reversible interconversion of protons and molecular hydrogen (Figure 1.4. (c)).[19]

As stated above, hetero-metal multinuclear complexes are an important class of compounds showing unique properties and functions which homo-metal complexes can't achieve. By selecting, designing and controlling the type of metal ions in these arrangements, targeted physical properties can be achieved. To assemble hetero-metal ions in one molecule, however, rational synthetic strategies are required. For example, a reasonable approach for the construction of hetero-metal complexes is a stepwise complexation method. One such approach is stepwise complexation with a macrocyclic ligand which has different coordination sites

to enable the introduction of hetero-metal ions depending on the affinity between metal ions and coordination sites (Scheme 1.1.).[20]

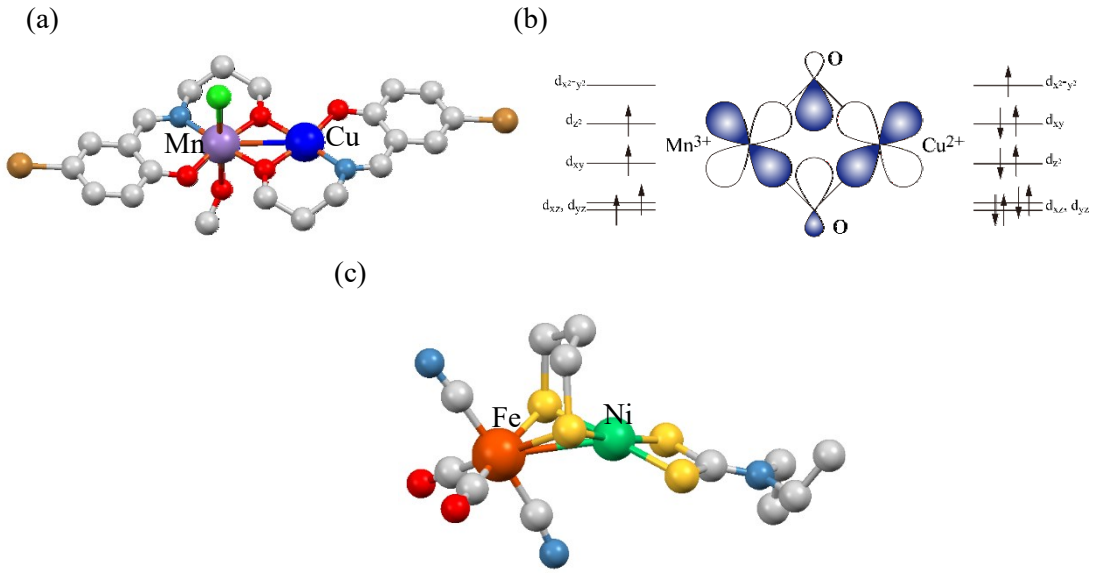

Figure 1.4. (a) Molecular structure of Mn-Cu complex, and (b) strict orthogonality of magnetic orbitals of between Mn^{3+} and Cu^{2+} ions. (c) Molecular structure of Fe-Ni complex.

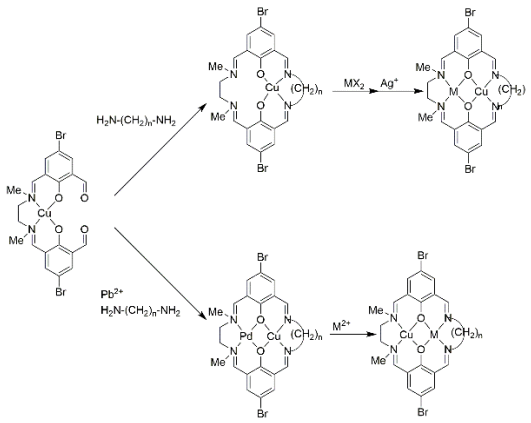

Scheme 1.1. Synthetic scheme of hetero-metallic dinuclear complexes with macrocycle ligands.

1.4 Grid-Type Complexes

Grid-type complexes can be constructed by self-assembly using polypyridine multidentate ligands and metal ions.[21] In grid-type complexes, the planar polypyridine ligands form a grid-like framework and metal ions are located on the cross points of the grid at even intervals. The grid framework may be considered as an addressable nanosystem. Moreover, grid-type complexes may be considered as logic elements in molecular devices such as quantum cellular automata or as quantum bits. These applications are based on delocalization of electrons on the grid corners and coulomb interactions between grids and thus it is important to control electronic states of metal ions in grid-type complexes.

The first [3 x 3] grid-type complex, $[Ag_9(L)_6](CF_3SO_3)_9$ was reported by J. M. Lehn, *et al.* at 1994 (Figure 1.5. (a)).[22] In recent years, the largest [5 x 5] grid-type complex, $[Mn_{25}(L)_{10}](ClO_4)_{20}\cdot 65H_2O$ was synthesized and characterized with current-imaging tunneling spectroscopy (CITS) imagery on a HOPG surface (Figure 1.5. (b)).[23] This CITS result suggested that an electron injection into metal ions may lead to controlled modification of the physical properties on a substrate.

Some interesting research on the physical properties of grid-type complexes have been reported as described below. The tetranuclear cobalt [2 x 2] complex, $[Co^{II}_4(L)_6](BF_4)_8$ showed twelve-step redox behavior (Figure 1.6.).[24] This multi-redox behavior suggested that the grid-type complex has the ability to serve as an electron reservoir, receiving and emitting a number of electrons and lending itself to potential application as a homogeneous catalyst. On the other hand, the tetranuclear iron [2 x 2] grid-type complex, $[Fe^{II}_4(L)_4](BF_4)_4$ and $[Fe^{II}_2Fe^{III}_2(L)_4](BF_4)_6$ showed multi-step spin crossover (SCO) behavior and site selective light-induced excited spin-state trapping (LIESST) (Figure 1.7.).[25]

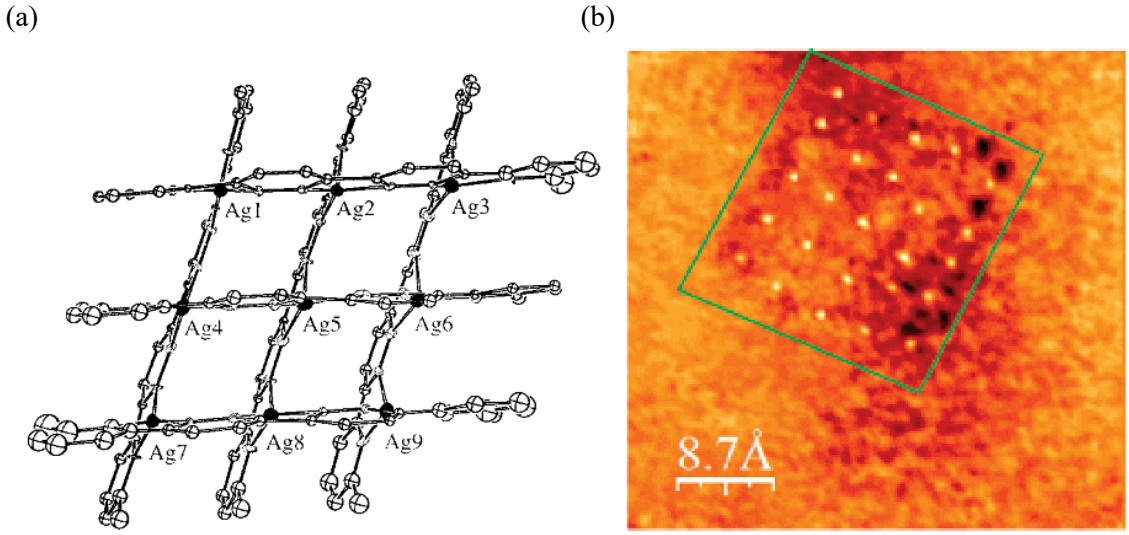

Figure 1.5. (a) The first [3 x 3] grid-type complex, and (b) the largest [5 x 5] grid-type complex on HOPG.

(a) (b)

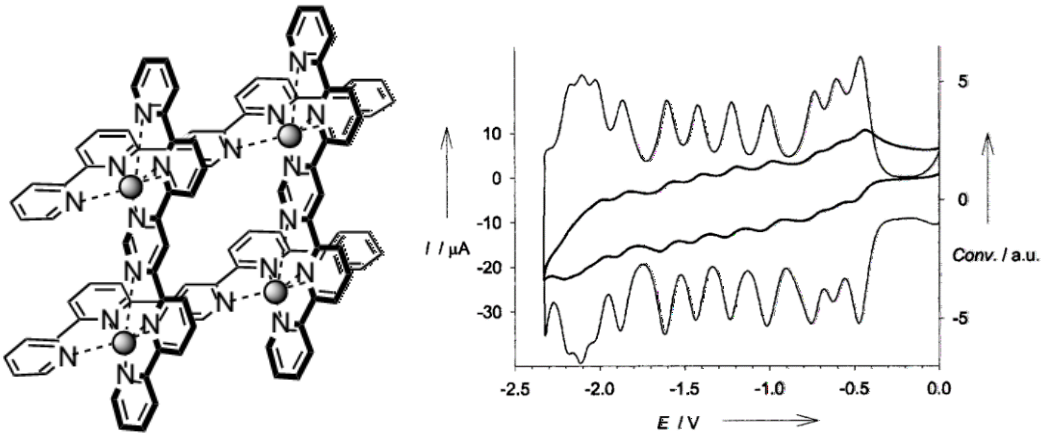

Figure 1.6. (a) Schematic structure of a Co [2 x 2] grid-type complex, and (b) its 12-step redox behavior.

(a) (b)

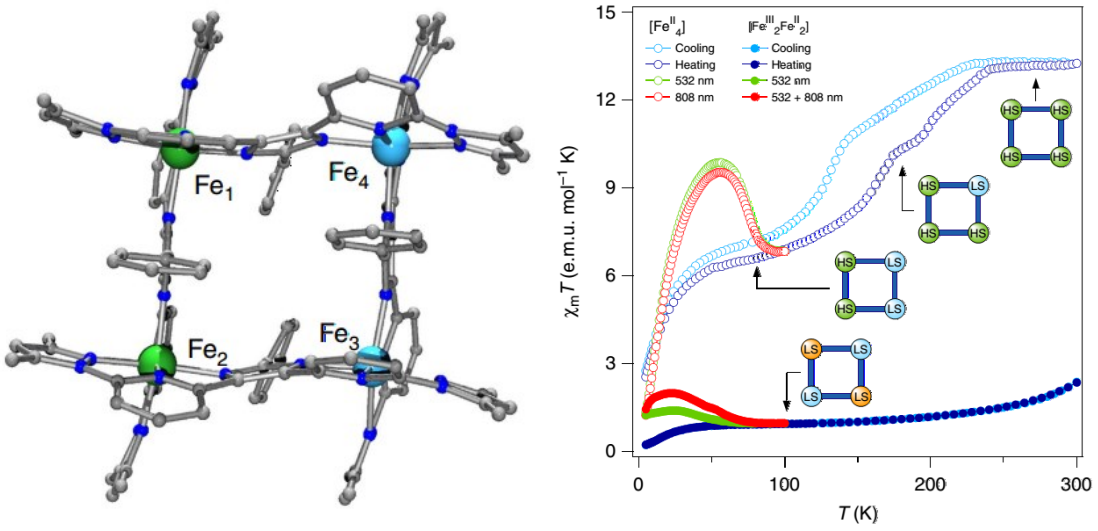

Figure 1.7. (a) Molecular structure of the Fe [2 x 2] grid-type complex $[Fe^{II}_4]$, and (b) its multistep SCO and LIESST behavior.

1.5 Mixed-Valence Complexes

Multinuclear complexes, which contain transition metals in different oxidation states, are called mixed-valence complexes. Such complexes can switch physical properties by electron transfer processes, if the complex shows relatively strong electronic interactions and physical properties based on delocalized electronic states. In UV-Vis absorption spectra, mixed-valence complexes can show inter-valence charge transfer (IVCT) bands in the near infrared region. This band originates from the charge transfer between different valence state of the metal ions. The magnitude of the electronic interaction between metal ions in a mixed-valence complex can be estimated from an analysis of the IVCT band, so called Hash's model.[26] The magnitude of the electronic interaction is expressed as an electronic coupling parameter (H_{AB}) and a degree of electron delocalization (α^2).[27]

$$H_{AB} = 2.06 \times 10^{-2}(\varepsilon_{max} \nu_{max} \Delta\nu_{1/2})^{1/2} / r$$

$$\alpha^2 = (H_{AB} / \nu_{max})^2$$

where ε_{max} ($M^{-1}cm^{-1}$), ν_{max} (cm^{-1}), $\Delta\nu_{1/2}$ (cm^{-1}), and r (Å) are the maximum molar absorption coefficients of the IVCT, the maximum energy of the IVCT, the full width at half maximum of the IVCT, and the distance between the metal centers, respectively. Such mixed-valence complexes are classified into three categories by Robin and Day, on the basis of electronic interactions between metal ions (Figure 1.8.).[28]

Class I

The interaction between metal ions is negligibly weak and electrons are localized on each metal ion. Their physical properties are sum of independent metal ions are observed. ($\alpha^2 = 0$)

Class II

The interaction between metal ions is stronger than those in Class I, and valence electrons are substantially delocalized. Metal ions are able to be distinguished. ($0 < \alpha^2 < 0.5$)

Class III

The interaction between metal ions is very strong, and electrons are completely delocalized. The valence of metal ions cannot be distinguished. ($\alpha^2 = 0.5$)

The amplitude of the electronic interactions between metal ions in mixed-valence states are measured by their comproportionation constant, K_c. If the class II mixed-valence complex has the equilibrium states as shown below, K_c is an equilibrium constant, expressing the stability of the mixed-valence complex in solution. The K_c value is calculated from a redox potential difference, $\Delta E_{1/2}$, based on the Nernst equation.

$$[M^{Z+1}\text{-}M^{Z+1}] + [M^{Z}\text{-}M^{Z}] \overset{K_c}{\rightleftarrows} 2\,[M^{Z+1}\text{-}M^{Z}]$$

(M: metal ion, Z: oxidation number)

$$K_c = \exp\left(\Delta E_{1/2}\ F/RT\right)$$

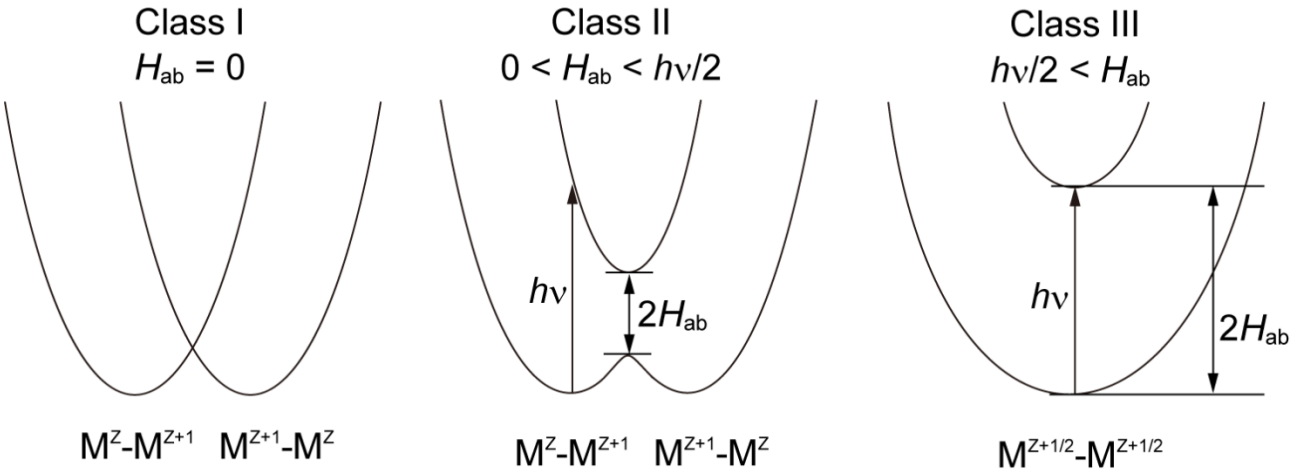

Figure 1.8. The symmetric potential surface of di-nuclear mixed-valence complex.

For example, a carboxylate bridged trinuclear iron complex, $[Fe_3O(O_2CCH_2CN)_6(H_2O)_3]$ is one of the mixed-valence complexes, consisted of two Fe(III) ions and one Fe(II) ion (Figure 1.9.).[29] This iron complex is a class III delocalized system in room temperature. At low temperature, structural phase transition from $R\bar{3}$ to $P\bar{1}$ occurred, and the mixed-valence state changes into a class II delocalized system. This phase transition is confirmed by the Mössbauer spectra and heat capacity measurements.

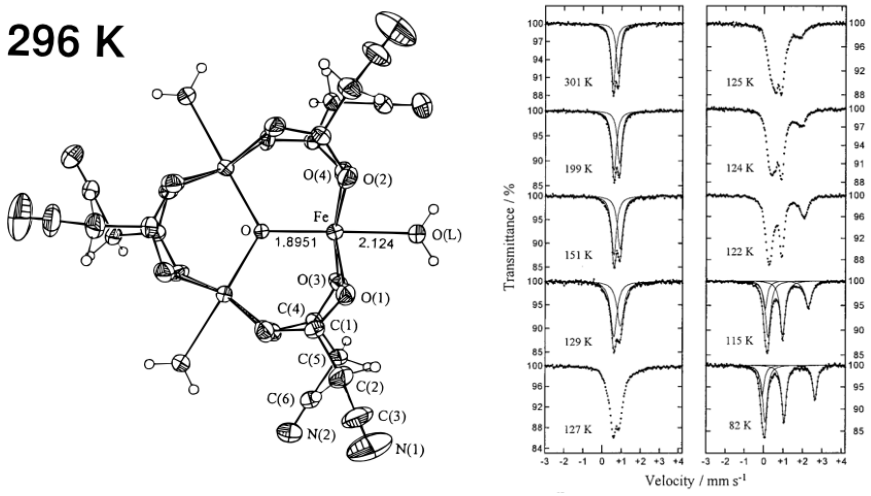

Figure 1.9. The molecular structure of $[Fe_3O(O_2CCH_2CN)_6(H_2O)_3]$ at 296 K (left), and the temperature dependent Mössbauer spectra (right).

Polyferrocenyl compounds[30] are further examples of mixed-valence complexes. A tetranuclear square-shaped complex, $[Fe_4(\eta^4\text{-}C_4)CoCp]$ (Fc = ferrocenyl, Cp = η^5-cyclopentadienyl anion) was reported by Fehlner *et al*. (Figure 1.10.).[31] This ferrocenyl complex showed multi-step redox behavior, and its one-electron oxidized state exhibited class III delocalized behavior. The two electron oxidized state was also mixed-valence state, and two redox isomers; *cis* and *trans* were supposed. This system is considered as a quantum bit (= qubit) or a quantum cellular automata (= QCA)[32].

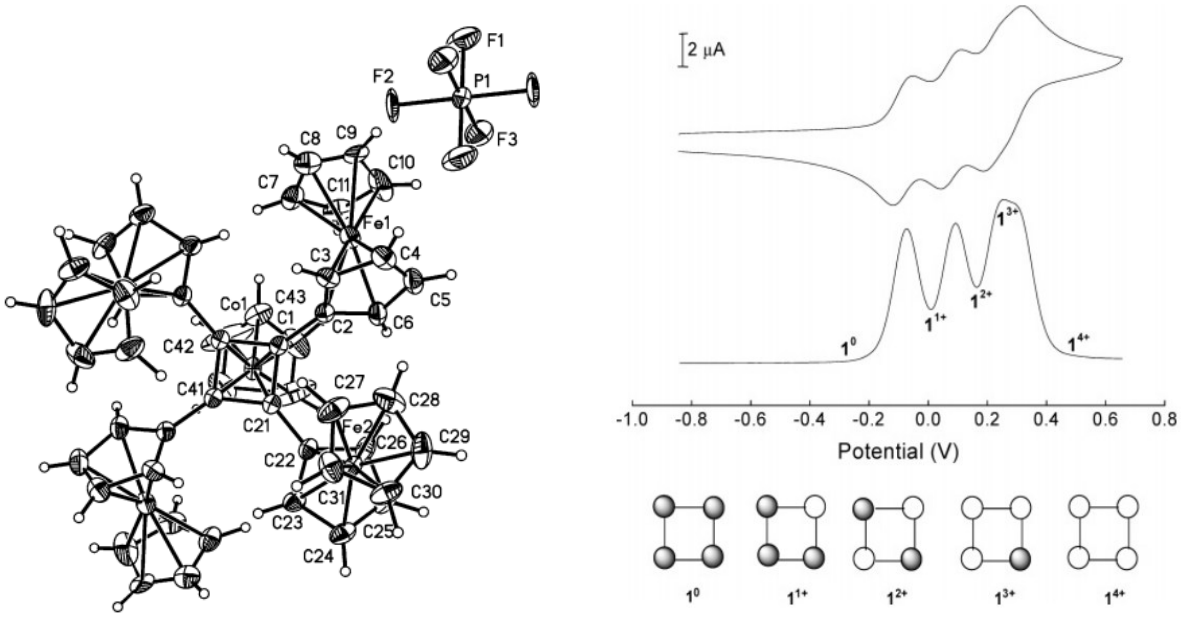

Figure 1.10. The X-ray structure of a one electron oxidized state of $[Fe_4(\eta^4\text{-}C_4)CoCp]$ (left), and the electrochemical properties with the supposed oxidation state model (right).

1.6 Spin-Crossover Complexes

The degeneracy of the *d* orbitals of first row transition metal complexes with six-coordinate octahedral geometry is split into t_{2g} orbitals and e_g orbitals whose energy gap is described as $10D_q$. The $10D_q$ value depend on not only the properties of the metal ions but also of the ligands and their coordination bond lengths. Generally, first row transition metal complexes with electron configurations from d^4 to d^7 can take either high-spin (HS) or low-spin (LS) states, due to the ligand field splitting ($10D_q$) and spin pairing energy (P). In the case of $10D_q << P$, the HS state with maximum spin multiplicity is the ground state following Hund's rule. In the reverse situation, spin pairs are formed in preference and the LS state is the ground state. When the $10D_q$ and P values are close, the HS and LS states can be interchanged reversibly through the application of external stimuli like temperature, pressure, magnetic field, and light (Figure 1.11.). This phenomenon is called spin-crossover (SCO) behavior. Some SCO complexes are bistable compounds which have potential applications as molecular switches.[33]

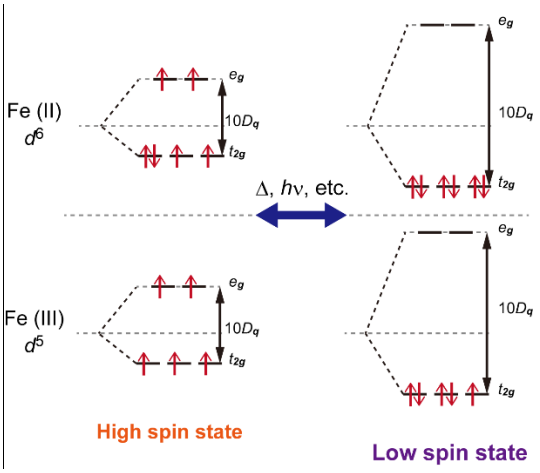

Figure 1.11. High spin (left) and low spin (right) state of iron(II) and iron(III) ions.

Iron (II) complexes are the most common SCO complexes.[34] The spin states of iron (II) SCO complexes are converted from paramagnetic HS ($S = 2$) to diamagnetic LS ($S = 0$) states, reversibly with large structural changes. Coordination bond lengths extend from about 1.9 Å to 2.1 Å with transition from the LS to the HS state. Such large structural changes were firstly reported in $[Fe(phen)_2(NCS)_2]$ (phen = 1, 10-phenanthroline) and $[Fe(bipy)_2(NCS)_2]$ (bipy = 4, 4'-bipyridine) by Baler and Bobonich at 1964.[35]

Iron (III) SCO complexes have been also reported.[36] An iron (III) SCO complex with three bidentate ligands of N, N-dithiocarbamato was discovered in 1931.[37] The iron (III) ion had S_6 coordination geometry in this first example, but other examples of iron (III) SCO complexes with Schiff base multidentate ligands and N_4O_2 geometries were subsequently reported, with the iron (III) SCO behavior tuned by chemical modification of the Schiff base ligands. A dinuclear iron (III) SCO complex, [(*R-salten*)Fe(bpy)Fe(*R*-salten)]$(BPh_4)_2$ (bpy = 4,4' -bipyridine) was also reported (Figure 1.12.).[38] Iron (III) complexes typically show gradual spin transitions from the LS state ($S = 1/2$) to the HS state ($S = 5/2$).

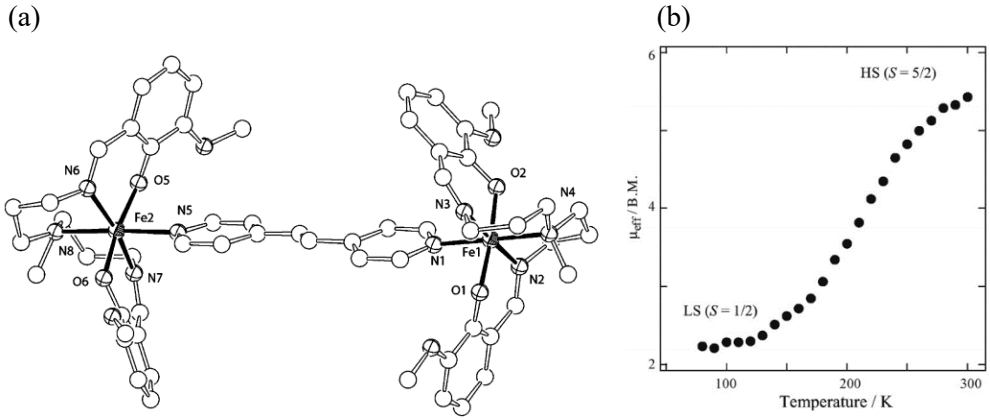

Figure 1.12. The dinuclear Fe(III) SCO complex (a), and its SCO behavior (b).

1.7 Contents

In this thesis, the structures and physical properties of self-assembled multinuclear complexes were studied. In CHAPTER 1 (this chapter), the outline of the important topics for this thesis are introduced. Consideration of the synthetic conditions and molecular structures of novel self-assembled complexes using a well-defined precursor are shown in CHAPTER 2. In CHAPTER 3, the electronic states of Cu-Fe heterometallic [3 x 3] grid-type complexes were controlled electrochemically. The structures and magnetic properties of redox isomers were compared. In CHAPTER 4, with the aim of moving towards applications in switching devices or molecular catalysis, a Ru [2 x 2] grid-type complex was synthesized and its electrochemical properties were revealed. To enhance the electronic interactions between metal ions, ruthenium ions were chosen and a system with four equivalent binding environments was designed.

---

[1] F. A. Cotton, *J. Chem. Soc. Dalton, Trans.*, **2000**, 1961-1968.

[2] (a) M. P. Shores, J. J. Sokol, and J. R. Long, *J. Am. Chem. Soc.*, **2002**, *124*, 2279-2292. (b) R. Sessoli, D. Gatteschi, A. Caneschi, and M. A. Novak, *Nature*, **1993**, *365*, 141-143. (c) H. Oshio, N. Hoshino, and T. Ito, *J. Am. Chem. Soc.*, **2000**, *122*, 12602-12603. (d) S. Koizumi, M. Nihei, T. Shiga, M. Nakao, H. Nojiri, R. Bircher, O. Waldmann, S. T. Ochsenbein, H. U. Güdel, F. Feranandez-Alonso, and H. Oshio, *Chem. Eur. J.*, **2007**, *13*, 8445-8453. (e) A. J. Tasiopoulos, A. Vinslava, W. Wernsdorfer, K. A. Abboud, and G. Christou, *Angew. Chem. Int. Ed.*, **2004**, *43*, 2117-2121. (f) M. T. Pope and A. Müller, *Angew. Chem. Int. Ed.*, **1991**, *30*, 34-48. (g) L. Lisnard, P. Mialane, A. Dolbecq, J. Marrot, J. M. Clemente-Juan, E. Coronado, B. Keita, P. Oliveira, L. Nadjo, and F. Sécheresse, *Chem. Eur. J.*, **2007**, *13*, 3525-3536. (h) R. Sakamoto, S. Katagiri, H. Maeda, and H. Nishihara, *Coord. Chem. Rev.*, **2013**, *257*, 1493-1506. (i) M. Haga, K. Kobayashi, K. Terada, *Coord. Chem. Rev.*, **2007**, *251*, 2688-2701.

[3] (a) S. Ghosh and P. S. Mukherjee, *Organometallics*, **2008**, *27*, 316–319. (b) M. J. E. Resendiz, J. C. Noveron, H. Disteldorf, S. Fischer, and P. J. Stang, *Org. Lett.*, **2004**, *6*, 651-653. (c) S. Ghosh, R. Chakrabarty, and P. S. Mukherjee, *Inorg. Chem.*, **2009**, *48*, 549-556. (d) S. Shanmugaraju, S. A. Joshi, and P. S. Mukherjee, *Inorg. Chem.*, **2011**, *50*, 11736–11745. (e) V. Vajpayee, Y. H. Song, M. H. Lee, H. Kim, M. Wang, P. J. Stang, and K.-W. Chi, *Chem. Eur. J.*, **2011**, *17*, 7837–7844. (f) S. Shanmugaraju, A. K. Bar, S. A. Joshi, Y. P. Patil, and P. S. Mukherjee, *Organometallics*, **2011**, *30*, 1951–1960. (g) W. Zhang, W. Jin, T. Fukushima, A. Saeki, S. Seki, T. Aida, *Science*,

2011, *334*, 340-342. (h) K. S. Wimbush, W. F. Reus, W. G. van der Wiel, D. N. Reinhoudt, G. M. Whitesides, C. A. Nijhuis, and A. H. Velders, *Angew. Chem.*, **2010**, *122*, 10374 –10378. (i) D. Fiedler, D. H. Leung, R. G. Bergman, and K. N. Raymond, *Acc. Chem. Res.*, **2005**, *38*, 351-360. (j) M. D. Pluth, R. G. Bergman, and K. N. Raymond, *Acc. Chem. Res.*, **2009**, *42*, 1650-1659. (k) V. Maurizot, M. Yoshizawa, M. Kawano and M. Fujita, *Dalton Trans.*, **2006**, 2750–2756. (l) R. Chakrabarty, P. S. Mukherjee, and P. J. Stang, *Chem. Rev.*, **2011**, *111*, 6810–6918.

[4] (a) M. Yagi, and M. Kaneko, *Chem. Rev.*, **2001**, *101*, 21-35. (b) W. Ruettinger, M. Yagi, K. Wolf, S. Bernasek, and G. C. Dismukes, *J. Am. Chem. Soc.*, **2000**, *122*, 10353-10357. (c) M. Okamura, M. Kondo, R. Kuga, Y. Kurashige, T. Yanai, S. Hayami, V. K. K. Praneeth, M. Yoshida, K. Yoneda, S. Kawata, and S. Masaoka, *Nature*, **2016**, *530*, 465-468. (d) C. Zhang, C. Cheng, H. Dong, J-R. Sheng, H. Dau, and J. Zhao, *Science*, **2015**, *348*, 690-693. (e) J. Y. Lee, O. K. Farha, J. Roberts, K. A. Scheidt, S. T. Nguyen, and J. T. Hupp, *Chem. Soc. Rev.*, **2009**, *38*, 1450-1459.

[5] (a) N. Hoshino, A. M. Ako, A. K. Powell, and H. Oshio, *Inorg. Chem.,* **2009**, *48*, 3396-3407. (b) R. Bagai, and G. Christou, *Chem. Soc. Rev.*, **2009**, *38*, 1011-1026. (c) A. K. Powell, S. L. Heath, D. Gatteschi, L. Pardi, R. Sessoli, G. Spina, F. D. Giallo, and F. Pieralli, *J. Am. Chem. Soc.*, **1995**, *117*, 2491-2502.

[6] (a) B. J. Holliday, and C. A. Mirkin, *Angew. Chem. Int. Ed.*, **2001**, *40*, 2022-2043. (b) M. M. J. Smulders, I. A. Riddell, C. Browne, and J. R. Nitschke, *Chem. Soc. Rev.*, **2013**, *42*, 1728-1754.

[7] G. M. Whitesides, J. P. Mathias, S. T. Seto, *Science*, **1991**, *254*, 1312.

[8] (a) J. –M. Lehn, A. Rigault, J. Siegel, J. Harrowfield, B. Chevier, D. Moras, *Proc. Natl. Acad. Sci. USA*, **1987**, *84*, 2565. (b) E. C. Constable, *Tetrahedron*, **1992**, *48*, 10013. (c) R. Krämer, J. –M. Lehn, A. D. Cian, J. Fischer, *Angew. Chem. Int. Ed. Engl.*, **1993**, *32*, 703. (d) B. Hasenknopf, J. –M. Lehn, B. O. Kneisel, G. Baum, D. Fenske, *Angew. Chem. Int. Ed. Engl.*, **1996**, *35*, 1838.

[9] T. R. Cook, Y.-R. Zheng, and P. J. Stang, *Chem. Rev.*, **2013**, *113*, 734−777.

[10] (a) M. Fujita, J. Yazaki, K. Ogura, *J. Am. Chem. Soc.*, **1990**, *112*, 5645. (b) S. Sato, J. Iida, K. Suzuki, M. Kawano, T. Ozeki, M. Fujita, *Science*, **2006**, *313*, 1273. (c) K. Suzuki, J. Iida, S. Sato, M. Kawano, M. Fujita, *Angew. Chem. Int. Ed.*, **2008**, *47*, 5780.

[11] N. Takeda, K. Umemoto, K. Yamaguchi, M. Fujita, *Nature*, **1999**, *398*, 794. S. Hiraoka, K. Harano, M. Shiro, Y. Ozawa, N. Yasuda, K. Toriumi, M. Shionoya, *Angew. Chem. Int. Ed.*, **2006**, *45*, 6488.

[12] (a) P. Mal, B. Breiner, K. Rissanen, and J. R. Nitschke, *Science*, **2009**, *324*, 1697-1699. (b) T. K. Ronson, S. Zarra, S. M. Black, and J. R. Nitschke, *Chem. Commun.*, **2013**, *49*, 2476-2490.

[13] (a) M. Yoshizawa, J. K. Klosterman, and M. Fujita, *Angew. Chem. Int. Ed.*, **2009**, *48*, 3418-3438. (b) M. J. Wiester, P. A. Ulmann, and C. A. Mirkin, *Angew. Chem. Int. Ed.*, **2011**, *50*, 114-137.

[14] (a) Y. Liu, V. Kravtsov, R. D. Walsh, P. Poddar, H. Srikanth, M. Eddaoudi, *Chem. Commun.*, **2004**, 2806. (b) R.-Q. Zou, L. Jiang, H. Senoh, N. Takeichi, Q. Xu, *Chem. Commun.*, **2005**, *3526*. (c) S. Roche, C. Haslam, H. Adams, S. L. Heath, and J. A. Thomas, *Chem. Commun.*, **1998**, 1681.

[15] (a) A. K. Bar, R. Chakrabarty, G. Mostafa, P. S. Mukherjee, *Angew. Chem., Int. Ed.*, **2008**, *47*, 8455. (b) M. Yoshizawa, M. Nagao, K. Kumazawa, M. Fujita, *J. Organomet. Chem.*, **2005**, *690*, 5383. (c) A. K. Bar, G. Mostafa, P. S. Mukherjee, *Inorg. Chem.*, **2010**, *49*, 7647. (d) M. Yoshizawa, J. Nakagawa, K. Kumazawa, M. Nagao, M. Kawano, T. Ozeki, M. Fujita, *Angew. Chem., Int. Ed.*, **2005**, *44*, 1810.

[16] R. H. Ismayilov, W. Z. Wang, G. H. Lee, C. Y. Yeh, S. A. Hua, Y. Song, M. M. Rohmer, M. Bénard, and S. M. Peng, *Angew. Chem. Int. Ed.*, **2011**, *50*, 2045-2048.

[17] (a) M. Andruh, J. P. Costes, C. Diaz, and S. Gao, *Inorg. Chem.*, **2009**, *48*, 3342-3359. (b) P. Chaudhuri, *Coord. Chem. Rev.*, **2003**, *243*, 143-190.

[18] H. Oshio, M. Nihei, A. Yoshida, H. Nojiri, M. Nakano, A. Yamaguchi, Y. Karaki, and H. Ishimoto, *Chem. Eur. J.*, **2005**, *11*, 843-848.

[19] Z. Li, Y. Ohki, and K. Tatsumi, *J. Am. Chem. Soc.*, **2005**, *127*, 8950-8951.

[20] (a) H. Okawa, H. Furutachi, and D. E. Fenton, *Coord. Chem. Rev.*, **1998**, *174*, 51-75. (b) M. Yonemura, Y. Matsumura, H. Furutachi, M. Ohba, and H. Okawa, *Inorg. Chem.*, **1997**, *36*, 2711-2717. (c) M. Yonemura, Y. Nakamura, N. Usui, and H. Okawa, *J. Chem. Sci.*, **2000**, *112*, 291-310.

[21] (a) M. Ruben, J. Rojo, F. J. Romero-Salguero, L. H. Uppadine, and J. M. Lehn, *Angew. Chem. Int. Ed.*, **2004**, *43*, 3644-3662. (b) B. L. Schottel, H. T. Chifotides, M. Shatruk, A. Chouai, L. M. Pérez, J. Bacsa, and K. R. Dunbar, *J. Am. Chem. Soc.*, **2006**, *128*, 5895-5912. (c) M. Ruben, J. M. Lehn, and P. Müller, *Chem. Soc. Rev.*, **2006**, *35*, 1056-1067.

[22] P. N. W. Baxter, J. M. Lehn, J. Fischer, and M. T. Youinou, *Angew. Chem. Int. Ed. Engl.*, **1994**, *33*, 2284-2287.

[23] S. K. Dey, T. S. M. Abedin, L. N. Dawe, S. S. Tandon, J. L. Collins, L. K. Thompson, A. V. Postnikov, M. S. Alam, and P. Müller, *Inorg. Chem.*, **2007**, *46*, 7767-7781.

[24] M. Ruben, E. Breuning, M. Barboiu, J. P. Gisselbrecht, and J. M. Lehn, *Chem. Eur. J.*, **2003**, *9*, 291-299.

[25] T. Matsumoto, G. N. Newton, T. Shiga, S. Hayami, Y. Matsui, H. Okamoto, R. Kumai, Y. Murakami, and H. Oshio, *Nature Commun.*, **2014**, *5*, 3865/1-3865/8.

[26] N. S. Hash, *Prog. Inorg. Chem.*, **1967**, *8*, 391.

[27] D. M. D'Alessandro, and F. R. Keen, *Chem. Rev.*, **2006**, *106*, 2270-2298.

[28] M. B. Robin, and P. Day, *Adv. Imorg. Chem. Radiochem.*, **1967**, *10*, 247.

[29] T. Nakamoto, M. Hanaya. M. Katoda, K. Endo, S. Kitagawa, and H. Sano, *Inorg. Chem.*, 1997, *36*, 4347-4359.

[30] (a) A. Hilderbrandt, T. Rüffer, E. Erasmus, J. C. Swarts, and H. Lang, *Organometallics*, **2010**, *29*, 4900. (b) A. Hilderbrandt, D. Schaarschmidt, and H. Lang, *Organometallics*, **2011**, *30*, 556. (c) Y. Yu, A. D. Bond, P. W. Leonard, U. J. Lorenz, T. V. Timofeeva, K. P. C. Vollhard, D. W. Glenn, and A. A. Yakovenko, *Chem. Commun.*, **2006**, *24*, 2572. (d) R. Djeda, A. Rapakousiou, L. Liang, N. Guidolin, J. Ruiz, and D. Astruc, *Angew. Chem. Int. Ed.*, **2010**, *49*, 8152. (e) A. K. Diallo, J.-C. Daran, F. Varret, J. Ruiz, and D. Astruc, *Angew. Chem. Int. Ed.*, **2009**, *48*, 3141. (f) A. K. Diallo, C. Absalon, J. Ruiz, and D. Astruc, *J. Am. Chem. Soc.*, **2011**, 133, 629.

[31] (a) J. Jiao, G. J. Long, F. Grandjean, A. M. Beatty, and T. P. Fehlner, *J. Am. Chem. Soc.*, **2003**, *125*, 7522-7523. (b) J. Jiao, G. J. Long, L. Rebbouh, F. Grandjean, A. M. Beatty, and T. P. Fehlner, *J. Am. Chem. Soc.*, **2005**, *127*, 17819-17831.

[32] (a) C. S. Lent, B. Isaksen, and M. Lieberman, *J. Am. Chem. Soc.*, **2003**, *125*, 1056-1063. (b) J. Jiao, G. J. Long, and F. Grandjean, *J. Am. Chem. Soc.*, **2003**, *125*, 7522-7523. (c) C. S. Lent, *Science*, **2000**, *288*, 1597-1599.

[33] (a) K. S. Murray, *Eur. J. Inorg. Chem.*, **2008**, 3101-3121. (b) O. Sato, J. Tao, and Y.-Z. Zhang, *Angew. Chem. Int. Ed.*, **2007**, *46*, 2152-2187.

[34] (a) P. Gütlich, A. Hauser, and H. Spiering, *Angew. Chem. Int. Ed. Engl.*, **1994**, *33*, 2024-2054. (b) P. Gütlich, Y. Garcia, and H. A. Goodwin, *Chem. Soc. Rev.*, **2000**, *29*, 419-427.

[35] (a) W. A. Baker, and H. M. Bobonich, *Inorg. Chem.*, 1964, *3*, 1184-1188. (b) E. König, and K. Madeja, *Inorg. Chem.*, **1967**, *6*, 48-55.

[36] (a) O. Sato, *Acc. Chem. Res.*, **2003**, *36*, 692-700. (b) P. J. Koningsbruggen, Y. Maeda, and H. Oshio, *Top. Curr. Chem.*, **2004**, *233*, 259-324. (c) M. Nihei, T. Shiga, Y. Maeda, and H. Oshio, *Coord. Chem. Rev.*, **2007**, *251*, 2606-2621.

[37] (a) L. Cambi, and L. Szegö, *Ber.*, **1931**, *10*, 2591. (b) L. Cambi, and L. Szegö, *Ber.*, **1933**, *66*, 656.

[38] R. Boča, Y. Fukuda, M. Gembický, R. Herchel, R. Jaroščiak, W. Linert, F. Renz, and J. Yuzurihara, *Chem. Phys. Lett.*, **2000**, *325*, 411-419.

CHAPTER 2

Control of Structures

2.1 Introduction

Self-assembled multinuclear metal complexes may afford the functionalities that underpin the next generation of nano-scale molecular devices and technologies.[1] Multinuclear complexes with a wide variety of topologies and structures, such as grid, ring, wheel, wire, helix, and cage, have been synthesized through the considered combination of metal ions and ligands.[2] The choice of multidentate ligand is key, when considering the construction of functional multinuclear complexes. For example, manganese clusters, have often been isolated with combinations of simple bridging ligands such as carboxylates and alkoxy groups[3]. Many such clusters have been shown to exhibit single molecule magnet (SMM) behavior[4] and biomimetic catalytic activity[5]. From the viewpoint of molecular design, exerting control over the coordination of single donor bridging groups such as oxido and alkoxido anions can be challenging and often relies heavily on serendipity. Although flexible bridging ligands provide unexpected polynuclear complexes, rigid ligands with distinct bridging directions and bridging numbers are useful for the development of well-programmed multinuclear complexes with regular arrays of metal ions. Such systems offer a controlled approach toward the generation of functional molecular materials.

The important factors when controlling the structure of self-assembled multinuclear complexes can be considered as follows: i) using the coordination geometry of metal ions (square planer, octahedral, etc.) and the angle of the bridging multidentate ligands, ii) noncovalent interactions, and iii) controlling synthetic conditions such as a concentration, solvents, and counter ions. In the case of i), square, cage and capsule type complexes were reported by Stang *et al.*[6] and M. Fujita *et al.*[7] which were constructed using directing building units with strictly oriented binding sites. Platinum ions and palladium ions are suitable for building units because they form stable square planar complexes. When coordinated by bidentate capping ligands in the *cis* position, the metal center is left with two free binding sites at an angle of 90° to each other. The combination of these building blocks with a linear bridging ligand leads to square-type complexes, while reaction with a tritopic ligand allows for the construction of octahedral cage complexes.[8] Using method ii), noncovalent interactions, such as hydrogen bonding, van der Waals forces, electrostatic, π-π stacking and anion-π interactions stabilize the target complexes selectively. Dunbar *et al.* reported the controlled synthesis of ring shaped structures; the square tetranuclear complex, $[M_4(bptz)_4(CH_3CN)_8][X]_8$ and pentagonal pentanuclear complex, $[M_5(bptz)_5(CH_3CN)_{10}][Y]_{10}$ (M = Ni, Fe; X = BF_4^-, ClO_4^-; Y = SbF_6^-, AsF_6^-, PF_6^-; bptz = 3,6-bis(2-pyridyl)-1,2,4,5-tetrazine) with anion-π interactions between counter anions and the π system of the ligands (Figure 2.1.).[9] In this research, method iii), in particular the choice of counter anion coordination behavior was used to exert control of the self-assembly process.

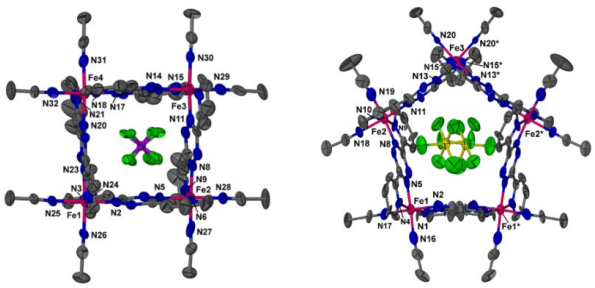

Figure 2.1. Structure controlling with anion-π interactions.
(left: tetranuclear complex with BF_4^-, right: pentanuclear complex with SbF_6^-,)

In previous research, various self-assembled multinuclear complexes with the polypyridine-type multidentate ligand, H_2L1 (=2,6-bis-[5-(2-pyridinyl)-1H-pyrazol-3-yl]-pyridine), were reported (Scheme 2.1.). The rigidity, planarity and multiple coordination sites (one tridentate and two bidentate) of the ligand are necessary to construct self-assembled multinuclear complexes. The shape of the obtained complexes may also depend on variety of metal ions and counter anions. When Fe(II) ions react with H_2L1 under the existence of non-coordinating tetrafluoroborate (BF_4^-) anions under ambient conditions, helix-type complexes are formed with a triangular oxo core.[10] In the case of Co(II), Cu(II) and Zn(II) ions, [3 x 3] grid-type complexes are the most stable products.[11] The iron heptanuclear helix-type complex, $[Fe^{II}_4Fe^{III}_3(HL1)(H_2L1)_5(\mu_2\text{-}OH)_6(OH)_6](BF_4)_4$ and copper nonanuclear [3 x 3] grid-type complex, $[Cu^{II}_9(L1)_6](BF_4)_6$ showed multi-step redox activity; five-step seven electron and four-step four electron redox processes, respectively. The cobalt nonanuclear [3 x 3] grid-type complex, $[Co^{II}_8Co^{III}(L1)_6](BF_4)_7$ showed single molecule magnet (SMM) behavior. However, metastable species such as an octanuclear ring-type complex, $[Co^{II}_8(L1)_4Cl_4(OAc)_4(H_2O)_4(MeOH)_4]$ can also be obtained in the presence of coordinating chloride anions.

Based on this knowledge, structural control of multinuclear clusters was investigated using non-innocent chloride anions. [3 x 3] grid-type complex was obtained by the reaction of copper ions and furthermore, several new self-assembled multinuclear complexes were synthesized by the reaction of the obtained chloride complex with Ag(I) ions, introduced to remove the chloride anions. In a similar manner, many other type of iron and manganese clusters were constructed with trinuclear oxo cores.[12]

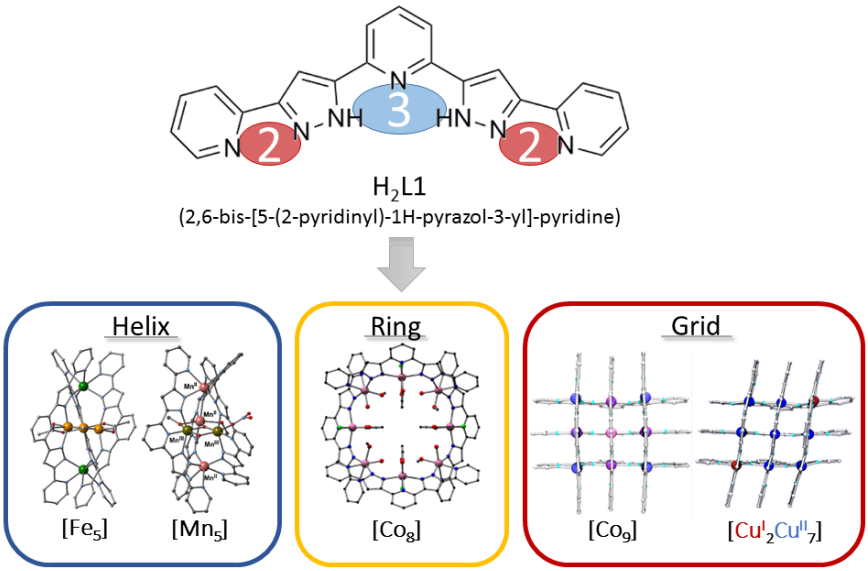

Scheme 2.1. A variety of self-assembled multinuclear complexes with H_2L1.

2.2 Experiments

Solvents were of reagent grade and used without further purification. The multidentate ligand H_2L (H_2L = 2,6-bis[5-(2-pyridinyl)-1*H*-pyrazole-3-yl]-pyridine) was obtained as described previously.[9, 10]

2.2.1. Synthesis of $[Cu_3(L1)Cl_4(MeOH)_2]$ ($[Cu^{II}_3]$)

A MeOH mixture (10 mL) of H_2L1 (36.8 mg, 0.10 mmol) and Et_3N (27.9 μL, 0.20 mmol) was added to a MeOH solution (10 mL) of $CuCl_2{\cdot}2H_2O$ (86.3 mg, 0.5 mmol). After adding CH_3CN (10 mL), the green needle-like crystal of **$[Cu_3]$** were crystallized by slow evaporation. These crystals were collected by filtration. Yield 8.4 mg, (11.1 %).

2.2.2. Synthesis of $[Cu^{II}_{12}(L1)_6(\mu_3\text{-}OH)_4(\mu_2\text{-}OH)_2](PF_6)_5(BF_4)$ ($[Cu^{II}_{12}]$)

A MeOH solution (10 mL) of $AgPF_6$ (31.4 mg, 0.12 mmol) was added to a MeOH solution (10 mL) of **$[Cu_3]$** (31.62 mg, 0.028 mmol). Chloride anions were removed as AgCl by filtration. A MeOH solution (5 mL) of $Cu(BF_4)_2{\cdot}nH_2O$ (6.56 mg, 0.028 mmol) and a MeOH mixture (10 mL) of H_2L1 (10.14 mg, 0.028 mmol) and Et_3N (7.81 μL, 0.056 mmol) was added to the filtrate, sequentially. After slow evaporation, **$[Cu^{II}_{12}]$** was obtained as green plate-like crystals.

2.2.3. Synthesis of $[Cu^{I}_4Cu^{II}_4Fe^{III}(L1)_6](BF_4)_3$ ($[Cu^{I}_4Cu^{II}_4Fe^{III}]$)

A MeOH solution (5 mL) of $AgBF_4$ (23.2 mg, 0.12 mmol) was added to a MeOH solution (5 mL) of **$[Cu_3]$** (19.3 mg, 0.025 mmol). Chloride anions were removed as AgCl by filtration. A CH_3CN solution (15 mL) of $Fe(BF_4)_2{\cdot}6H_2O$ (50.6 mg, 0.15 mmol) and a MeOH mixture (5 mL) of H_2L1 (45.8 mg, 0.13 mmol) and Et_3N (34.8 μL, 0.25 mmol) was added to the filtrate, sequentially. After slow evaporation, [**$Cu^{I}_4Cu^{II}_4Fe^{III}$**] was obtained as brown crystals.

2.2.4. Synthesis of $[Fe^{III}_{10}(L1)_6(\mu_3\text{-}O)(\mu_2\text{-}O)_4(\mu_2\text{-}HO)_5(Cl)(H_2O)_2]Cl_2$ ($[Fe^{III}_{10}]$)

A MeOH mixture (10 mL) of H_2L1 (65.8 mg, 0.18 mmol) and Et_3N (50.18 μL, 0.36 mmol) was added to a CH_3CN solution (10 mL) of $FeCl_2{\cdot}nH_2O$ (35.2 mg, 0.28 mmol). Red brown plate-like crystals of **$[Fe^{III}_{10}]$** were crystallized by diffusion with benzene.

2.2.5. Synthesis of $[Fe^{III}_5(L1)_2(\mu_3\text{-}O)_2(\mu_2\text{-}O)(HL1)(Cl)(H_2L1)_3](PF_6)_3$ ($[Fe^{III}_5]$)

A MeOH mixture (5 mL) of H_2L1 (32.9 mg, 0.09 mmol) and Et_3N (25.1 μL, 0.18 mmol) was added to a CH_3CN solution (5 mL) of $FeCl_2{\cdot}nH_2O$ (17.6 mg, 0.14 mmol). After addition of an excess amount of NH_4PF_6, **$[Fe^{III}_5]$** was obtained as red brown crystals by diffusion with *p*-xylene.

2.2.6. Synthesis of $[Mn^{II}_3Mn^{III}_2(L1)_3(\mu_3\text{-}O)(NO_3)(OMe)_2(MeOH)](NO_3){\cdot}4MeOH{\cdot}H_2O$ ($[Mn^{II}_3Mn^{III}_2]$)

To a methanolic solution (7.5 mL) of $Mn(NO_3)_2{\cdot}6H_2O$ (38.4 μL,0.24 mmol), a solution of H_2L1 (43.9 mg, 0.12 mmol) and Et_3N (33 μL, 0.24 mmol) in methanol (7.5 mL) was added. The resulting pale yellow solution was filtered, and the filtrate gradually turned red-brown. After a few days of slow evaporation, dark red-brown platelet crystals of 1 suitable for X-ray diffraction analysis were obtained. The crystals were collected by suction filtration and dried in air to afford $[Mn^{II}_3Mn^{III}_2(L)_3(\mu_3\text{-}O)(NO_3)(OMe)_2(H_2O)](NO_3){\cdot}4H_2O$. $C_{64}H_{52}Mn_5N_{24}O_{16}$ (1687.94): calcd. C 45.58, H 3.21, N 19.72; found C 45.54, H 3.11, N 19.92. IR (KBr): $\tilde{\nu}$ max = 1601 (C=N), 1566 (C=N) cm^{-1}.

2.2.7. Synthesis of $[Mn^{II}_8(L1)_6(\mu_3\text{-}Cl)_2]Cl_2\cdot 3C_2H_4Cl_2\cdot 60H_2O\cdot 2DMF$ ($[Mn^{II}_8]$)

To a suspension of $MnCl_2\cdot 4H_2O$ (35.8 mg, 0.18 mmol) in acetonitrile (10 mL) was added an acetonitrile solution (5 mL) of H_2L1 (21.9 mg, 0.06 mmol) and Et_3N (16.7 μL, 0.12 mmol). The resulting solution was heated and stirred for 15 min to afford a yellow precipitate. The crude product was collected by filtration and dissolved in DMF. The DMF solution was filtered, and 1,2-dichloroethane was diffused into this solution at 40 °C. After a few days, yellow plates of 2 were obtained. The crystals were collected by filtration and dried in air to afford $[Mn^{II}_8(L)_6(\mu_3\text{-}Cl)_2]Cl_2\cdot C_2H_4Cl_2\cdot DMF\cdot 12H_2O$. $C_{131}H_{113}Cl_6Mn_8N_{43}O_{13}$ (3149.80): calcd. C 49.95, H 3.62, N 19.12; found C 49.89, H 3.69, N 19.21. IR (KBr): $\tilde{\nu}$ max = 1601 (C=N), 1576 (C=N) cm^{-1}.

2.2.8. X-ray crystallography

The single-crystal X-ray diffraction data for the complexes were collected with a Bruker-AXS SMART APEX diffractometer with Mo-$K\alpha$ radiation (λ = 0.71073 Å) in ω-2θ scan mode. The diffraction data were corrected for Lorentz and polarization effects and for absorption using the SADABS program.[13] The structures were solved by direct methods, and the structure solution and refinement were based on $|F|^2$ using SHELX software.[14] All non-hydrogen atoms were refined with anisotropic displacement parameters, whereas all hydrogen atoms were positioned geometrically and refined with isotropic displacement parameters according to the riding model. All geometrical calculations were performed using the SHELXL-2013 software. SQUEEZE[15] treatments were applied for refinements of complex **$[Mn^{II}_8]$** owing to extreme disordering of the solvent molecules.

2.2.9. Physical measurements

Elemental analyses for carbon, hydrogen, and nitrogen were performed with a PerkinElmer CHN analyser (Model 2400). The IR spectra (KBr pellets, 4000-400 cm^{-1}) were recorded at 298 K using a Shimadzu Model IR Affinity-1 spectrometer.

2.3 Results and Discussion

2.3.1. Structures of copper systems

The structure of **[Cu$^{II}_3$]** at 100 K is shown in Figure 2.2. The crystallographic data and selected bond lengths are listed in Table 2.1 and 2.2, respectively. **[Cu$^{II}_3$]** crystallized in the monoclinic space group *C*2/c. The asymmetric unit consists of two copper ions, a half of the ligand, $L1^{2-}$, two chloride anions and one MeOH molecule and a *C*2 axis exist penetrating the central copper ion parallel to the Cu-N_{py} bond. All three coordination sites of the polypyridine ligand, $L1^{2-}$, were used for coordinating to copper ions. While the two terminal copper ions, Cu1 and Cu1*, were coordinated by one chloride anion and one MeOH, the central copper ion, Cu2, was coordinated with two chloride anions only. The terminal copper ions showed a four-coordination environment close to a square planar geometry, and the other the central copper ion had trigonal bipyramidal molecular geometry. The coordination geometry, bond lengths, and charge balance suggested that all copper ions were divalent.

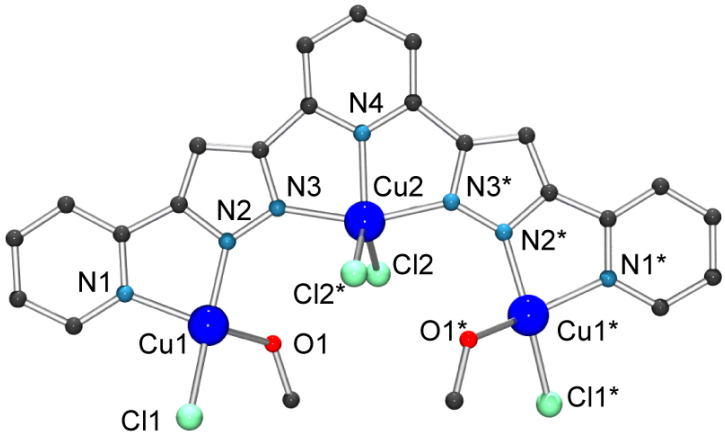

Figure 2.2. Molecular structure of **[Cu$^{II}_3$]**. Symmetry operation: *; −x. +y, 1/2−z. Hydrogen atoms, solvent molecules and counter ions are omitted for clarity. Color code: Cu^{II}, blue; N, steel blue; C, gray20; O, red; Cl, aquamarine.

The structure of **[Cu$^{II}_{12}$]** at 100 K is shown in Figure 2.3. The crystallographic data and selected bond lengths for **[Cu$^{II}_{12}$]** are listed in Table 2.1 and 2.3, respectively. **[Cu$^{II}_{12}$]** crystallized in the triclinic space group $P\bar{1}$. In the asymmetric unit, two complex units were observed and each complex unit was constructed from twelve copper ions, six ligands, six hydroxide ions, five hexafluorophosphate and one tetrafluoroborate anion. Three ligands coordinated to the metal ions from the upper and lower sides of the grid surface.

Because of the irregular coordination manner of the central ligands, twelve copper ions were assembled in a grid-like manner. All copper(II) ions have five-coordinate geometry. Copper ions in this complex were categorized into three types of coordination environment; inner shell (Cu1, Cu2, Cu3, Cu4), edge (Cu5, Cu7, Cu9, Cu11) and corner (Cu6, Cu8, Cu10, Cu12). In the four inner shell, the Cu1/Cu4 group and Cu2/Cu3 group have trigonal bipyramidal [N_3O_2] and [N_2O_3] coordination environments, respectively. On the other hand, in the edge group, Cu5 and Cu11 ions have square pyramidal [N_5] geometry and the Cu7/Cu9 ions display square planar [N_3O_1] geometry. Moreover, the four corner copper ions, Cu6, Cu8, Cu10 and Cu12, had trigonal bipyramidal geometry with [N_4O_1] coordination. The coordination geometry, bond length and charge balance suggested that all copper ions are divalent.

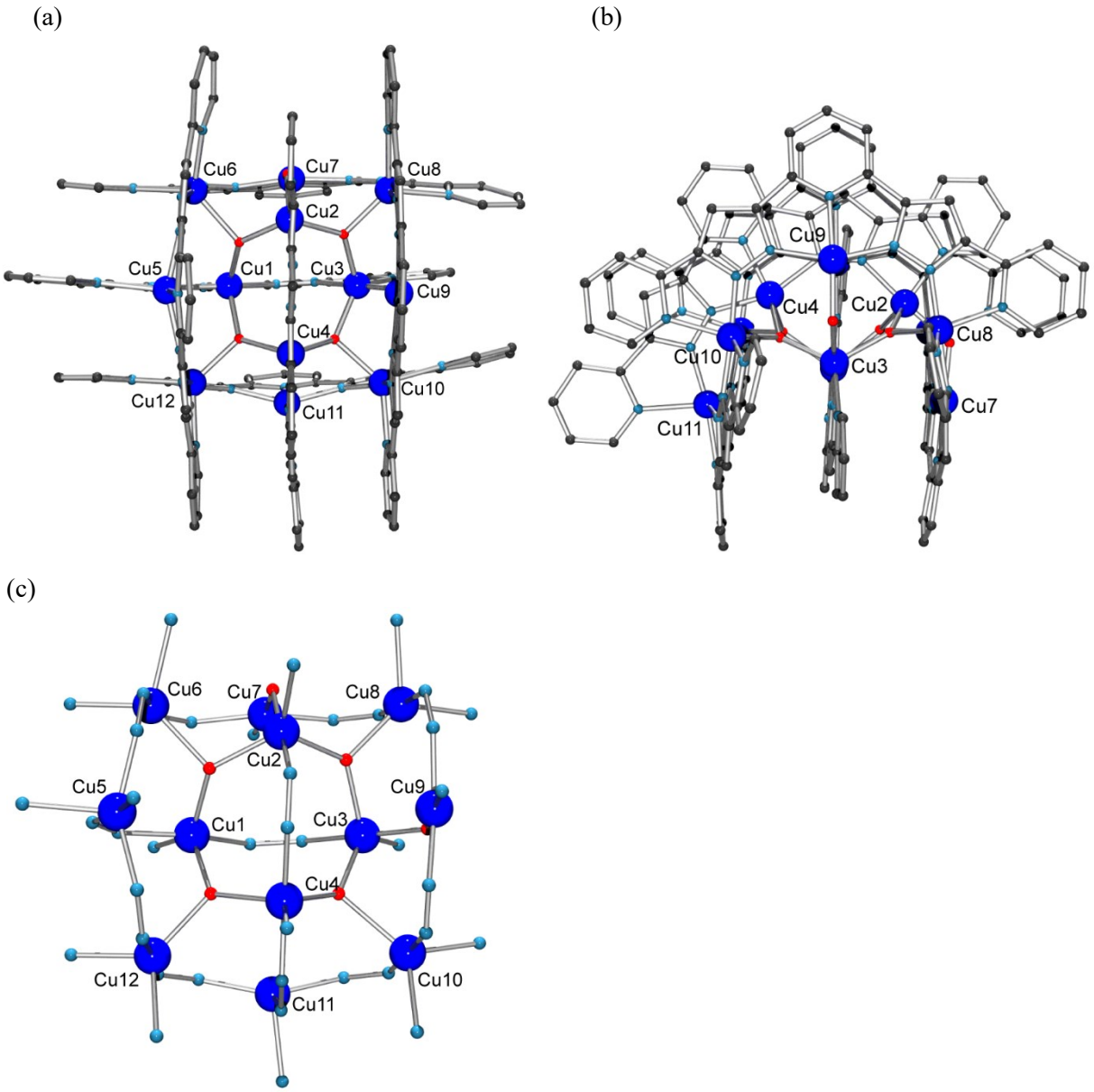

Figure 2.3. Molecular structure of **[Cu^{II}_{12}]**.
(a) overall structure (top view), (b) overall structure (side view), and (c) core structure (top view).
Hydrogen atoms, solvent molecules and counter ions are omitted for clarity.
Color code: Cu^{II}, blue; N, steel blue; C, gray20; O, red.

The structure of **[$Cu^{I}_{4}Cu^{II}_{4}Fe^{III}$]** at 100 K is shown in Figure 2.4. The crystallographic data and selected bond lengths for **[$Cu^{I}_{4}Cu^{II}_{4}Fe^{III}$]** are listed in Table 2.1 and 2.4, respectively. **[$Cu^{I}_{4}Cu^{II}_{4}Fe^{III}$]** crystallized in the monoclinic space group *C*2/c. The *C*2 axis exists along a diagonal line running through Cu4-Fe1-Cu5. The asymmetric unit of **[$Cu^{I}_{4}Cu^{II}_{4}Fe^{III}$]** consists of one half of the central iron ion, four copper ions, three ligands, and one point five tetrafluoroborate anions. Metal ions were arranged in a [3 x 3] grid like arrangement and three ligands coordinate metal ions from the upper and lower sides of the grid surface. The oxidation state of the metal ions in **[$Cu^{I}_{4}Cu^{II}_{4}Fe^{III}$]** was confirmed by the bond lengths and charge balance considerations. The central iron ion, four copper ions on the edge and corner copper ions were assigned as Fe(III), Cu(II), Cu(I) ions, respectively. Against expectations, the **[Cu^{II}_{3}]** building unit was not retained. Magnetic properties of this complex will be discussed in detail in CHAPTER III.

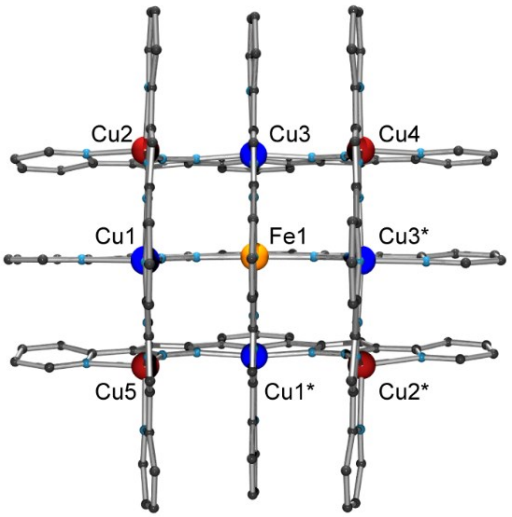

Figure 2.4. Molecular structure of **[$Cu^{I}_{4}Cu^{II}_{4}Fe^{III}$]**. Symmetry operation: *; −x. +y, 1/2−z. Hydrogen atoms, solvent molecules and counter ions are omitted for clarity. Color code: Cu^{II}, blue; Cu^{I}, scarlet; Fe^{III}, orange; N, steel blue; C, gray20.

Table 2.1. Crystallographic parameters for copper systems.

	[Cu^{II}_3]	**[Cu^{II}_{12}].**	**[$Cu^{I}_4Cu^{II}_4Fe^{III}$].**
Chemical formula	$C_{23}H_{25}Cl_4Cu_3N_7O_4$	$C_{126}H_{88}B_1Cu_{12}F_{34}N_{42}O_8P_5$	$C_{128}H_{94}B_3Cu_8F_{12}Fe_1N_{42}O_6$
Formula weight	795.92 g/mol	3892.52 g/mol	3141.05 g/mol
Temperature	100 K	100 K	100 K
Wavelength	0.71073 Å	0.71073 Å	0.71073 Å
Crystal system	Monoclinic	Triclinic	Monoclinic
Space group	*C*2/c	$P\bar{1}$	*C*2/c
a	12.077(3) Å	17.7432(16) Å	24.056(5) Å
b	23.439(7) Å	29.629(3) Å	20.511(5) Å
c	10.303(3) Å	29.908(3) Å	26.449(6) Å
α	-	111.3052(15)°	-
β	104.089(5)°	92.6439(15)°	98.568(3)°
γ	-	97.6588(17)°	-
Volume	2828.8(14) $Å^3$	14441(2) $Å^3$	2828.8(14) $Å^3$
Z	4	4	4
Density (calculated)	1.869 g/cm^3	1.790 g/cm^3	1.617 g/cm^3
Absorption coefficient	2.658 mm^{-1}	1.899 mm^{-1}	1.491 mm^{-1}
F(000)	1596	7744	6340
θ range for data collection	1.74 to 24.37°	1.164 to 20.388°	1.311 to 27.134°
Index ranges	-13≤h≤13	-17≤h≤15	-30≤h≤29
	-27≤k≤17	-29≤k≤21	-26≤k≤22
	-11≤l≤11	-29≤l≤29	-33≤l≤18
Reflections collected	6437	45475	35820
Independent reflections	2313 [*R*(int) = 0.0690]	28275 [*R*(int) = 0.0571]	14182 [*R*(int) = 0.0967]
Data / restraints / parameters	2313 / 0 / 197	28275 / 29 / 2457	14182 / 4 / 936
Goodness-of-fit on F^2	1.602	1.596	1.087
Final *R* indices [$I>2\sigma(I)$]	R_1 = 0.0945	*R*1 = 0.1119	*R*1 = 0.0760
	wR_2 = 0.2449	*wR*2 = 0.2794	*wR*2 = 0.1821
	R_1 = 0.1474	*R*1 = 0.1708	*R*1 = 0.1736
	wR_2 = 0.2688	*wR*2 = 0.3071	*wR*2 = 0.2318
Largest diff. peak and hole	3.494 and -3.912 $eÅ^{-3}$	1.761 and -1.512 $eÅ^{-3}$	1.15 and -0.61 $eÅ^{-3}$

Table 2.2. Bond lengths (Å) for **[Cu^{II}_3]**.

Cu1-N2	1.933(7)	Cu2-N4	1.983(9)
Cu1-O1	1.974(7)	Cu2-N3	1.991(6)
Cu1-N1	2.001(7)	Cu2-Cl2	2.304(11)
Cu1-Cl1	2.173(3)		

Table 2.3. Bond lengths (Å) for **[Cu^{II}_{12}]**.

Cu1-N10	1.974(14)	Cu2-O5	1.931(11)	Cu3-O6	1.947(11)
Cu1-N11	1.989(13)	Cu2-N30	1.971(14)	Cu3-N13	1.972(15)
Cu1-O1	2.032(10)	Cu2-O2	2.059(9)	Cu3-O3	2.024(11)
Cu1-N12	2.047(14)	Cu2-O1	2.064(10)	Cu3-N14	2.081(15)
Cu1-O4	2.122(9)	Cu2-N29	2.074(16)	Cu3-O2	2.080(10)
Cu4-N32	1.966(14)	Cu5-N9	1.953(14)	Cu6-N23	1.916(14)
Cu4-N33	1.970(15)	Cu5-N26	1.988(15)	Cu6-N2	1.921(14)
Cu4-N31	1.992(15)	Cu5-N25	1.994(14)	Cu6-N1	2.101(14)
Cu4-O3	2.040(11)	Cu5-N24	1.996(16)	Cu6-O1	2.173(11)
Cu4-O4	2.120(9)	Cu5-N8	2.242(14)	Cu6-N22	2.222(16)
Cu7-O5	1.914(10)	Cu8-N6	1.895(15)	Cu9-O6	1.905(11)
Cu7-N5	1.939(14)	Cu8-N37	1.909(15)	Cu9-N39	1.969(15)
Cu7-N3	1.968(15)	Cu8-O2	2.100(10)	Cu9-N38	1.973(16)
Cu7-N4	1.971(14)	Cu8-N7	2.109(17)	Cu9-N40	1.986(16)
		Cu8-N36	2.152(17)		
Cu10-N20	1.901(15)	Cu11-N34	1.963(15)	Cu12-N16	1.920(14)
Cu10-N41	1.929(15)	Cu11-N17	1.977(15)	Cu12-N27	1.946(14)
Cu10-N21	2.126(17)	Cu11-N18	1.988(14)	Cu12-N15	2.106(13)
Cu10-N42	2.169(18)	Cu11-N19	1.995(14)	Cu12-N28	2.128(15)
Cu10-O3	2.275(14)	Cu11-N35	2.267(17)	Cu12-O4	2.127(10)

Table 2.4. Bond lengths (Å) for **[$Cu^{I}_{4}Cu^{II}_{4}Fe^{III}$]**.

Fe1-N11	1.960(5)	Cu1-N15	1.968(5)	Cu2-N2	2.012(6)
Fe1-N11	1.960(5)	Cu1-N9	1.970(5)	Cu2-N13	2.016(6)
Fe1-N10	1.964(5)	Cu1-N16	1.993(6)	Cu2-N1	2.210(7)
Fe1-N10	1.964(5)	Cu1-N14	2.005(6)	Cu2-N12	2.225(6)
Fe1-N21	1.976(6)	Cu1-N8	2.284(6)		
Fe1-N21	1.976(6)				
Cu3-N20	1.956(5)	Cu4-N6	1.999(6)	Cu5-N17	1.959(6)
Cu3-N4	1.968(5)	Cu4-N6	1.999(6)	Cu5-N17	1.959(6)
Cu3-N3	1.988(6)	Cu4-N7	2.194(7)	Cu5-N18	2.197(7)
Cu3-N5	2.013(6)	Cu4-N7	2.194(7)	Cu5-N18	2.197(7)
Cu3-N19	2.273(6)				

2.3.2. Discussion on copper systems

In the reaction of H_2L1 with $CuCl_2 \cdot 2H_2O$, coordinating chloride ions induced formation of the trinuclear complex, **[Cu^{II}_3]**, which was constructed from three copper (II) ions and one ligand, L^{2-}. Coordination of chloride ions appears to prevent the formation of the grid moiety.

The neutral trinuclear copper complex **[Cu^{II}_3]** was used as a starting compound for further cluster syntheses. Chloride anions in **[Cu^{II}_3]** were easily removed by addition of $AgBF_4$ resulting in insoluble AgCl and allowing the remaining core to be used for further cluster formations. The dodecanuclear complex **[Cu^{II}_{12}]** and the nonanuclear grid-type complex **[$Cu^{I}_4Cu^{II}_4Fe^{III}$]** were obtained by the reaction of **[Cu^{II}_3]** with additional copper (II) ions and iron (II) ions, respectively. It is noted that the four copper (II) ions in the mixed metal grid were reduced to Cu(I) ions by the iron (II) ions. The previous study suggested that an intermediate $M(L1)_2$ species with two bidentate L1 was formed.[16] The bite angle of two ligands which coordinate to Cu(I) ion was about 90 °, and this might lead to stabilization of the grid framework. It should be noted that structures of multinuclear complexes were controlled not only by coordinative chloride ions but also by addition of metal ions (Scheme 2.2.).

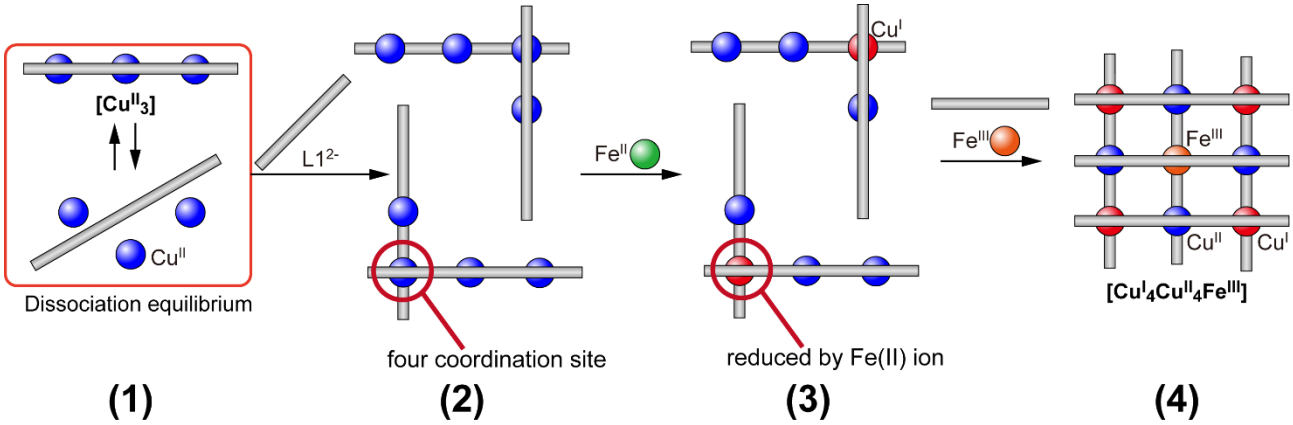

Scheme 2.2. Speculated formation process of **[$Cu^{I}_4Cu^{II}_4Fe^{III}$]** from **[$Cu^{II}_3$]**.

2.3.3. Structures of iron systems

The structure of **[Fe^{III}_{10}]** at 100 K is shown in Figure 2.5. The crystallographic data and the selected bond lengths are listed in Table 2.5 and 2.6, respectively. **[Fe^{III}_{10}]** crystallized in the triclinic space group $P\bar{1}$. The pseudo-grid like multinuclear cluster **[Fe^{III}_{10}]** was formed with six polypyridine ligands, $L1^{2-}$, five oxo ions, five hydroxide ions, two water and three chloride ions (one chloride ion coordinates to Fe9). Iron ions were bridged by oxo or hydroxo ions. The coordination geometry, bond length, BVS calculations and charge balance suggested that all iron ions were trivalent (Table 2.7). From the result of the structural analysis, the assembly mechanism is hypothesized to be as shown in Scheme 2.3. **[Fe^{III}_{10}]** was constructed from one [2 x 2] pseudo grid core (Fe1, Fe2, Fe3, and Fe4), one oxo-bridged tetrahedral tetranuclear core (Fe6, Fe7, Fe8, and Fe9), and two capping cores of Fe5 and Fe10. In the tetranuclear tetrahedral core, the Fe6 ion was linked to the Fe7, Fe8 and Fe9 ions through μ_2-oxo ions, and Fe7, Fe8, and Fe9 ions were bridged by μ_3-oxo ligands.

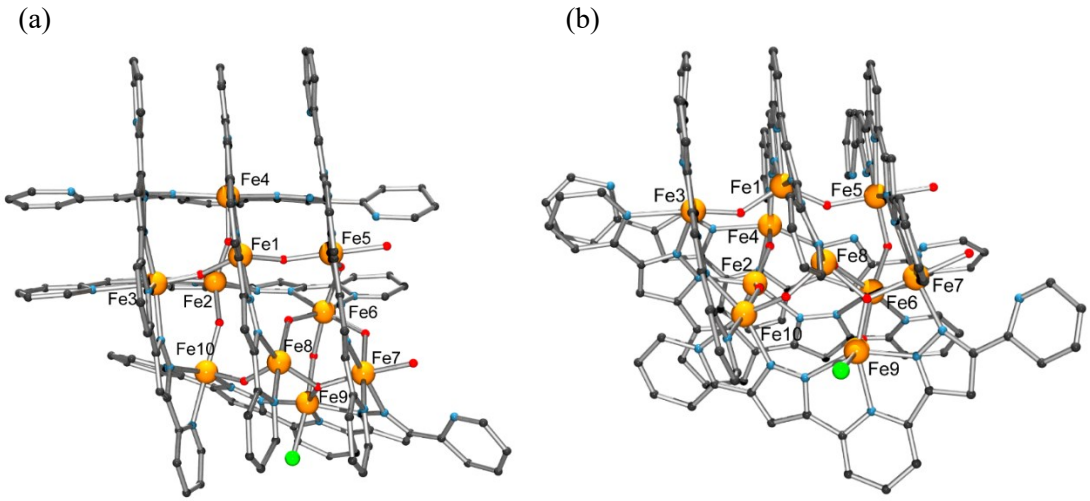

Figure 2.5. Molecular structure of **[Fe^{III}_{10}]**. ((a) top view, and (b) side view). Hydrogen atoms, solvent molecules and counter ions are omitted for clarity. Color code: Fe^{III}, orange; N, steel blue; C, gray20; O, red; Cl, green.

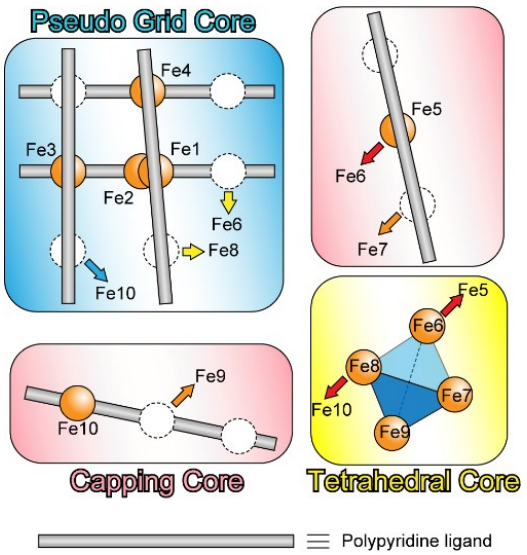

Scheme 2.3. Schematic drawing of core components in **[Fe^{III}_{10}]**.

The molecular structure of **[Fe$^{III}_5$]** at 100 K is shown in Figure 2.6. The crystallographic data and selected bond lengths for **[Fe$^{III}_5$]** are listed in Table 2.5 and 2.8, respectively. **[Fe$^{III}_5$]** crystallized in the triclinic space group $P\bar{1}$. The pseudo-grid like multinuclear cluster of **[Fe$^{III}_5$]** was composed with five iron ions, six polypyridine ligands, three oxo ions, and one chloride ion. The oxidation state of all iron ions were determined as trivalent by the coordination geometry, bond lengths, BVS calculations and charge valence (Table 2.9). The central dinuclear core was constructed from μ_3-oxo-bridged Fe1 and Fe2 ions. The Fe1 and Fe2 ions were bridged to Fe4 and Fe5 by μ_3-oxo ions, while the Fe1 ion has a further link to the Fe3 ion through a μ_2-oxo ion (Scheme 2.4.). One free ligand of L1 is located next to the **[Fe$^{III}_5$]** moiety through hydrogen bonds between pyrazole groups. The **[Fe$^{III}_5$]** cluster has a total of five coordinating sites.

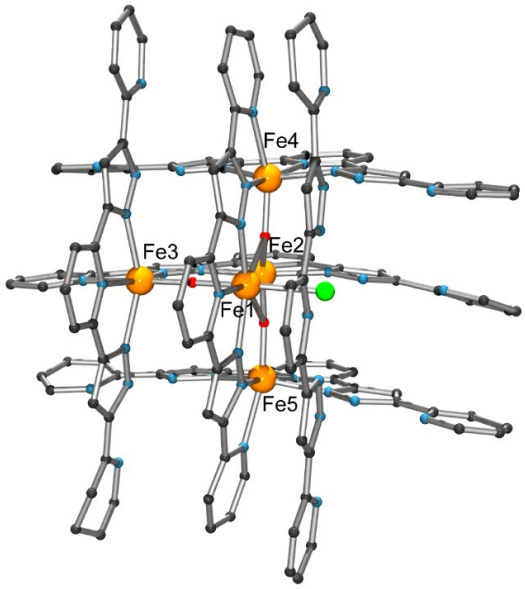

Figure 2.6. Molecular structure of **[Fe$^{III}_5$]**.
Hydrogen atoms, solvent molecules and counter ions are omitted for clarity.
Color code: Fe^{III}, orange; N, steel blue; C, gray20; O, red; Cl, green.

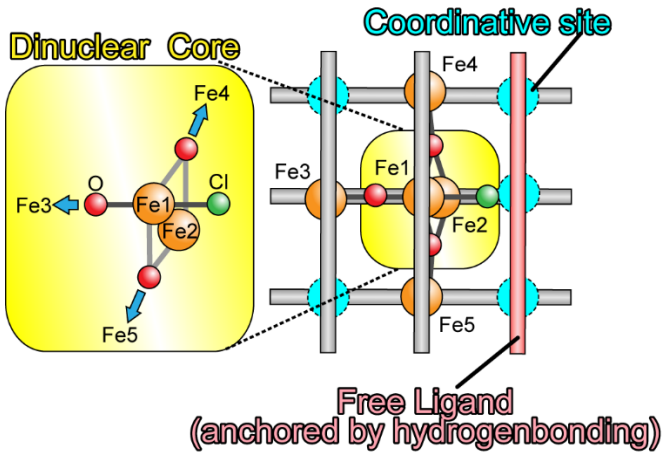

Scheme 2.4. Schematic drawing of core components in **[Fe$^{III}_5$]**.

Table 2.5. Crystallographic parameters for iron systems

	$[Fe^{III}_{10}]$	$[Fe^{III}_{5}]$.
Chemical formula	$C_{126}H_{105}Cl_3Fe_{10}N_{42}O_{21}$	$C_{127}H_{98}Cl_1F_{18}Fe_5N_{35}O_5P_3$
Formula weight	3208.36 g/mol	2944.01 g/mol
Temperature	100 K	100 K
Wavelength	0.71073 Å	0.71073 Å
Crystal system	Triclinic	Triclinic
Space group	$P\bar{1}$	$P\bar{1}$
a	17.776(4) Å	18.368(2) Å
b	20.874(4) Å	19.712(3) Å
c	23.012(5) Å	22.070(3) Å
α	84.603(3)°	106.8897(19)°
β	75.108(3)°	93.720(2)°
γ	66.401(3)°	98.4979(19)°
Volume	2828.8(14) $Å^3$	7513.0(17) $Å^3$
Z	2	2
Density (calculated)	1.409 g/cm^3	1.301 g/cm^3
Absorption coefficient	1.057 mm^{-1}	0.603 mm^{-1}
F(000)	3268	2998
θ range for data collection	1.06 to 20.83°	1.10 to 26.55°
Index ranges	-17≤h≤17	-23≤h≤20
	-20≤k≤20	-22≤k≤24
	-22≤l≤22	-16≤l≤27
Reflections collected	24741	41091
Independent reflections	15678 [*R*(int) = 0.1136]	30303 [*R*(int) = 0.0347]
Data / restraints / parameters	15678 / 628 / 1819	30303 / 0 / 1957
Goodness-of-fit on F^2	1.594	1.530
Final *R* indices [$I>2\sigma(I)$]	*R*1 = 0.1289	*R*1 = 0.1010
	*wR*2 = 0.3220	*wR*2 = 0.2672
	*R*1 = 0.2560	*R*1 = 0.1711
	*wR*2 = 0.3725	*wR*2 = 0.3014
Largest diff. peak and hole	1.247 and -0.609 $eÅ^{-3}$	1.629 and -1.345 $eÅ^{-3}$

Table 2.6. Bond lengths (Å) for **[Fe^{III}_{10}]**.

Fe1-O5	1.803(15)	Fe2-O3	1.757(11)	Fe3-O4	1.751(14)
Fe1-O4	1.809(12)	Fe2-O7	1.871(12)	Fe3-N9	2.054(17)
Fe1-N31	2.050(16)	Fe2-N10	2.082(17)	Fe3-N25	2.139(17)
Fe1-N33	2.098(17)	Fe2-N12	2.14(2)	Fe3-N24	2.155(15)
Fe1-N32	2.118(17)	Fe2-N11	2.132(16)	Fe3-N26	2.164(17)
				Fe3-N8	2.376(18)
Fe4-O3	1.793(12)	Fe5-O5	1.825(13)	Fe6-O8	1.991(17)
Fe4-N30	2.081(17)	Fe5-O6	1.984(16)	Fe6-O10	1.991(14)
Fe4-N5	2.18(2)	Fe5-O1	2.108(14)	Fe6-O9	2.006(15)
Fe4-N4	2.182(17)	Fe5-N39	2.16(2)	Fe6-O6	2.022(16)
Fe4-N3	2.193(17)	Fe5-N38	2.17(2)	Fe6-N13	2.18(2)
Fe4-N29	2.278(16)	Fe5-N40	2.33(2)	Fe6-N14	2.22(3)
Fe7-O12	1.870(17)	Fe8-O11	1.772(15)	Fe9-O12	1.898(15)
Fe7-O9	1.98(2)	Fe8-O12	1.972(16)	Fe9-O10	2.015(18)
Fe7-O2	2.01(2)	Fe8-O8	2.017(16)	Fe9-N19	2.11(3)
Fe7-N41	2.07(2)	Fe8-N34	2.21(2)	Fe9-N17	2.15(2)
Fe7-N20	2.13(2)	Fe8-N35	2.22(3)	Fe9-N18	2.24(3)
Fe7-N42	2.16(3)			Fe9-Cl1	2.306(13)
Fe10-O11	1.791(15)				
Fe10-O7	1.992(13)				
Fe10-N27	2.08(2)				
Fe10-N16	2.09(2)				
Fe10-N28	2.15(2)				
Fe10-N15	2.282(19)				

Table 2.7. Bond valence sum calculation and average bond lengths (Å) for **[Fe^{III}_{10}]**.

	average bond lengths	Fe(II)	Fe(III)
Fe1	1.98(16)	2.82	3.23
Fe2	2.00(16)	2.71	3.10
Fe3	2.11(16)	2.62	2.99
Fe4	2.12(17)	2.46	2.80
Fe5	2.10(17)	2.47	2.82
Fe6	2.07(19)	2.46	2.81
Fe7	2.04(22)	2.76	3.15
Fe8	2.04(20)	2.39	2.74
Fe9	2.12(22)	2.60	2.94
Fe10	2.06(18)	2.74	3.13

Table 2.8. Bond lengths (Å) for **[Fe^{III}_5]**.

Fe1- O2	1.787(4)	Fe2- O3	1.785(4)	Fe3- O3	1.743(4)
Fe1- O1	1.807(4)	Fe2-N31	2.104(5)	Fe3-N9	2.095(6)
Fe1-N10	2.100(5)	Fe2-N33	2.129(5)	Fe3-N26	2.186(6)
Fe1-N11	2.124(6)	Fe2-N32	2.280(6)	Fe3-N24	2.210(6)
Fe1-N12	2.157(5)	Fe2- O1	2.283(4)	Fe3-N25	2.202(6)
		Fe2-Cl1	2.4690(17)	Fe3-N8	2.228(6)
Fe4- O1	1.828(4)	Fe5- O2	1.812(4)		
Fe4-N30	2.005(5)	Fe5-N34	2.005(6)		
Fe4-N4	2.155(5)	Fe5-N17	2.124(6)		
Fe4-N3	2.155(5)	Fe5-N19	2.168(5)		
Fe4-N5	2.207(5)	Fe5-N17	2.160(6)		
Fe4-N29	2.243(5)	Fe5-N35	2.255(6)		

Table 2.9. Bond valence sum calculation and average bond lengths (Å) for **[Fe^{III}_5]**.

	average bond lengths	Fe(II)	Fe(III)
Fe1	1.995(5)	2.737	3.128
Fe2	2.175(2)	2.402	2.723
Fe3	2.111(2)	2.564	2.920
Fe4	2.099(2)	2.550	2.901
Fe5	2.087(2)	2.633	2.996

2.3.4. Discussion about formation of iron systems

The structures of the multinuclear iron complexes were controlled by the existence of the coordinative chloride ions, like in the case of the copper systems, and novel structures which differed from both the grid and helix-type were obtained. In the case of the reaction with iron ions, the chloride ions did not coordinate to all metal centers. It is considered that the affinity between the iron ions and the (hard base) oxo ions was higher than the for the chloride ions. Thus, the chloride ions coordinated to iron ions partially, allowing for the formation of asymmetrical structures like **[Fe^{III}_{10}]** and **[Fe^{III}_5]**.

In the iron systems, the choice of counter anions, chloride or hexafluorophosphate, led to the different structures. To track the process of the iron clusters formation by the time resolved ESI-MS was performed, an indicated that both **[Fe^{III}_{10}]** and **[Fe^{III}_5]** were formed in equal ratio in solution. In this case, it was suggested that the counter exchange from chloride ions to hexafluorophosphate ions contributed to the stabilization of the crystal structures, but not necessarily of the structural formation.

2.3.5. Molecular structure of manganese systems

The structure of the pentanuclear manganese complex, $[Mn_5(L1)_3(\mu_3\text{-}O)(NO_3)(OMe)_2(MeOH)](NO_3)\cdot 4MeOH\cdot H_2O$ (**$[Mn^{II}_3Mn^{III}_2]$**), is shown in Figure 2.7, and crystallographic parameters are provided in Table 2.10. **$[Mn^{II}_3Mn^{III}_2]$** crystallized in the monoclinic space group *C*c and consists of three ligands and five manganese ions with a μ_3-oxo ion, forming a pentanuclear manganese cluster with trigonal bipyramidal metal topology. The asymmetric unit is composed of one $[Mn_5(L1)_3(\mu_3\text{-}O)(NO_3)(OMe)_2(MeOH)]$ cluster unit, one nitrate ion, four methanol molecules, and one water molecule. The five manganese ions can be categorized into two types: terminal (Mn4 and Mn5) and central (Mn1, Mn2 and Mn3). All manganese ions have six-coordinate octahedral geometry. The terminal Mn4 and Mn5 ions have N_6 donor sets from three bidentate ligand sites, while the Mn1 ion in the central trinuclear unit has a N_3O_3 coordination environment derived from the tridentate site of one ligand, a μ_3-oxo group, a bridging methoxo moiety and a methanol molecule. The Mn2 ion has a monodentate nitrate ion in place of the methanol molecule that coordinates Mn1, and the Mn3 ion has a N_3O_3 coordination environment derived from the tridentate site of a ligand, the μ_3-oxo group and two bridging methoxo moieties. The Mn1, Mn2 and Mn3 ions form a planar Mn_3O core, in which the manganese ions approximately describe an isosceles triangle with Mn1···Mn2, Mn2···Mn3 and Mn3···Mn1 metal-metal separations of 3.721, 3.000 and 3.053 Å, respectively.

The manganese ions in **$[Mn^{II}_3Mn^{III}_2]$** have average coordination bond lengths of 2.148, 2.096, 2.063, 2.288, and 2.267 Å for Mn1 – Mn5, respectively. The octahedral coordination environments of all manganese ions deviate from regular octahedron, and angular distortion parameters (Σ) of Mn1 – Mn5 are calculated as 116.8, 113.1, 108.3, 139.6 and 130.9, respectively. Bond valence sum (BVS) calculations,[17] charge balance, and the appearance or absence of Jahn-Teller distortion, imply that the terminal manganese ions (Mn4 and Mn5) and one of the central manganese ions (Mn1) are divalent and the other two are trivalent. Considering the structural features and bond lengths of the three central ions, Mn2 and Mn3 ions can be assigned as trivalent. Mn1, Mn2 and Mn3 all have μ_3-O and μ_2-OMe bridges, but Mn3 has two MeO^- bridges and one μ_3-O bridge, therefore the trivalent state is likely to be stabilized. The Mn1 ion is coordinated by a monodentate methanol ligand, while Mn2 has a monodentate nitrate ion, suggesting that the Mn1 and Mn2 ions can be assigned as divalent and trivalent, respectively. M_5 helix-type complexes, with similar [1,3,1] core structures to **$[Mn^{II}_3Mn^{III}_2]$**, have been reported by our group, M.-L. Tong et al., and S. Kawata et al.[18]

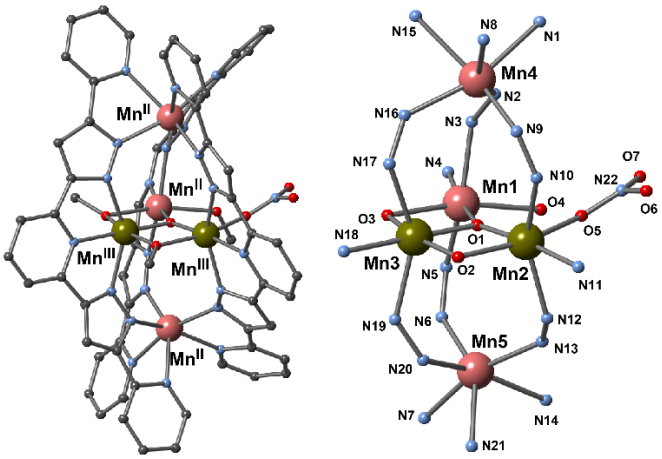

Figure 2.7. The molecular structure of **$[Mn^{II}_3Mn^{III}_2]$**. The pentanuclear cluster (left) and core structure (right). Hydrogen atoms are omitted for clarity. Color code: C, gray; N, light blue; O, red; Mn^{II}, pink; Mn^{III}, khaki.

The structure of the octanuclear cluster $[Mn_8(L1)_6(\mu_3\text{-}Cl)_2]Cl_2 \cdot 3C_2H_4Cl_2 \cdot 60H_2O \cdot 2DMF$ (**[Mn^{II}_8]**) is shown in Figure 2.8, and the crystallographic parameters are shown in Table 2.10. **[Mn^{II}_8]** crystalized in the monoclinic space group *P*2/n, and is constructed from six ligands, eight manganese ions and two μ_3-Cl anions. The asymmetric unit contains half of one octanuclear cluster, $\{Mn_4(L1)_3(\mu_3\text{-}Cl)\}$, one Cl^- anion, one and a half $C_2H_4Cl_2$ groups and four water molecules. The octanuclear cluster has a centre of symmetry, and the remaining part can be generated following the symmetry operation 1/2–x, +y, 3/2–z. The manganese ions can be classified into two distinct groups: those found in the central triangular core and those occupying the terminal N_6 coordination sites. The Mn4 ions are located in the terminal sites, and have N_6 coordination environments formed by the bidentate sites of three ligands. The Mn1, Mn2, and Mn3 ions form the triangular Mn_3Cl core, in which each manganese ion has a N_5Cl octahedral geometry derived from tridentate and bidentate capping by two ligand molecules, and coordination by a bridging chloride ion. The Mn_3Cl core is almost planar with Mn1-Mn2, Mn2-Mn3 and Mn3-Mn1 metal-metal separations of 4.311, 4.358, and 4.259 Å, respectively.

Considering the coordination bond lengths of the manganese ions, BVS calculations,[19] coordination geometries and charge balance, all manganese ions are divalent. In general, d^5 transition metal ions can form distorted octahedral geometry without restrictions of ligand field stabilization energy. In the octanuclear cluster, all manganese ions have distorted geometries due to the physical restrictions of the coordination sites, and are stabilized in their divalent state. Octanuclear clusters with the same [1,3,3,1] core structures have been reported by M.-L. Tong et al. and R.W. Saalfrank et al.[20] Analogues based on Cd and Zn ions, which have d^{10} electronic configurations and can exist comfortably in distorted octahedral geometries, have also been reported by Saalfrank group. It can be considered that the octanuclear core motif is a structure that favors d^5 and d^{10} metal ions due to the distorted nature of the metal coordination geometries.

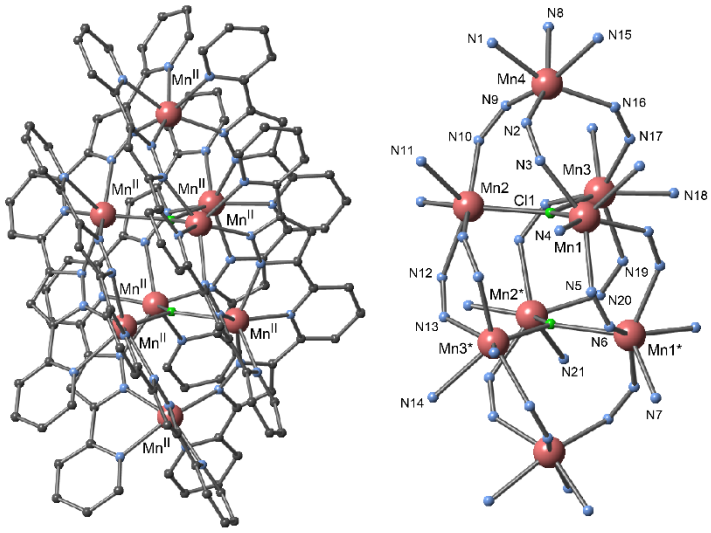

Figure 2.8. Molecular structures of **[Mn^{II}_8]**. Octanuclear cluster (left) and core structure (right). Hydrogen atoms are omitted for clarity. Color code: C, gray; N, light blue; O, red; Mn^{II}, pink; Cl, green.

Table 2.10. Crystallographic parameters for manganese systems

	$[Mn^{II}_3Mn^{III}_2]$	$[Mn^{II}_8]$
Chemical formula	$C_{70}H_{67}N_{23}O_{15}Mn_5$	$C_{140}H_{208}N_{44}C_{110}Mn_8O_{62}$
Formula weight	1745.16 g/mol	4293.51 g/mol
Temperature	100 K	100 K
Wavelength	0.71073 Å	0.71073 Å
Crystal system	Monoclinic	Monoclinic
Space group	*Cc*	*P*2/n
a	23.021(10) Å	21.806(4) Å
b	13.315(6) Å	13.968(3) Å
c	24.762(11) Å	25.921(5) Å
α		-
β	104.429(6)°	93.126(3)°
γ		-
Volume	7351(5) $Å^3$	7883(3) $Å^3$
Z	4	2
Density (calculated)	1.577 g/cm^3	1.809 g/cm^3
Absorption coefficient	0.919 mm^{-1}	0.877 mm^{-1}
F(000)	3572	3932
θ **range for data collection**	1.698 to 27.499°	1.189 to 25.499°
Index ranges	-29≤h≤29	-26≤h≤26
	-17≤k≤17	-16≤k≤16
	-14≤l≤32	-18≤l≤31
Reflections collected	20964	38956
Independent reflections	6986 [*R*(int) = 0.0644]	14655 [*R*(int) = 0.0520]
Data / restraints / parameters	10754 / 6 / 1022	14655 / 16 / 899
Goodness-of-fit on F^2	1.019	1.152
Final ***R*** **indices [**$I>2\sigma(I)$**]**	*R*1 = 0.0629	*R*1 = 0.1064
	*wR*2 = 0.1495	*wR*2 = 0.3191
R indices **(all data)**	*R*1 = 0.1112	*R*1 = 0.1429
	*wR*2 = 0.1793	*wR*2 = 0.3423
Largest diff. peak and hole	0.736 and -0.619 $eÅ^{-3}$	3.454 and -1.2.9 $eÅ^{-3}$

Table 2.11. Bond lengths (Å) for **[$Mn^{II}_3Mn^{III}_2$]**.

Mn1-O1	1.963(9)	Mn2-O1	1.892(10)	Mn3-O1	1.886(8)
Mn1-N4	2.149(8)	Mn2-O2	2.075(8)	Mn3-O3	1.905(9)
Mn1-N5	2.174(8)	Mn2-O15	2.100(10)	Mn3-O2	1.906(10)
Mn1-N3	2.192(8)	Mn2-N11	2.102(9)	Mn3-N18	2.135(9)
Mn1-O4	2.204(10)	Mn2-N12	2.197(9)	Mn3-N19	2.272(8)
Mn1-O3	2.205(7)	Mn2-N10	2.207(9)	Mn3-N17	2.273(9)
Mn4-N16	2.167(8)	Mn5-N20	2.146(8)		
Mn4-N9	2.184(8)	Mn5-N6	2.192(9)		
Mn4-N2	2.246(8)	Mn5-N13	2.205(8)		
Mn4-N1	2.319(8)	Mn5-N14	2.325(9)		
Mn4-N15	2.358(9)	Mn5-N21	2.347(8)		
Mn4-N8	2.455(8)	Mn5-N7	2.387(8)		

Table 2.12. Bond lengths (Å) for **[Mn^{II}_8]**.

Mn1-N6	2.192(6)	Mn2-N20	2.185(6)
Mn1-N4	2.251(6)	Mn2-N11	2.249(6)
Mn1-N3	2.273(6)	Mn2-N10	2.287(6)
Mn1-N5	2.329(6)	Mn2-N12	2.368(6)
Mn1-N7	2.433(6)	Mn2-N21	2.441(6)
Mn1-Cl1	2.497(2)	Mn2-Cl1	2.500(2)
Mn3-N13	2.156(6)	Mn4-N2	2.178(6)
Mn3-N18	2.248(6)	Mn4-N9	2.182(6)
Mn3-N17	2.249(5)	Mn4-N16	2.189(6)
Mn3-N19	2.353(6)	Mn4-N1	2.340(6)
Mn3-N14	2.475(6)	Mn4-N8	2.362(6)
Mn3Cl1	2.495(2)	Mn4-N15	2.384(6)

2.4 Conclusion

Counter anion variation was successfully employed to influence the self assembly process of multinuclear transition metal clusters. In the reactions of copper ions with a multidentate polypyridine ligand, H_2L1 (H_2L1 = 2,6-bis[5-(2-pyridinyl)-1H-pyrazole-3-yl]-pyridine), the chloride ions coordinate to cap the coordination sites of the copper ions, and the stable neutral trinuclear complex, $[Cu_3(L1)Cl_4(MeOH)_2]$ (**$[Cu^{II}_3]$**), was obtained. **$[Cu^{II}_3]$** was synthesized and used as a precursor for further cluster syntheses. The reaction of **$[Cu^{II}_3]$** with copper and iron ions gave a dodecanuclear copper cluster, $[Cu^{II}_{12}(L1)_6(\mu_3\text{-}OH)_4(\mu_2\text{-}OH)_2](PF_6)_5(BF_4)$ (**$[Cu^{II}_{12}]$**), and the heterometal [3 x 3] grid-type complex, $[Cu^{I}_4Cu^{II}_4Fe^{III}(L1)_6](BF_4)_3$ (**$[Cu^{I}_4Cu^{II}_4Fe^{III}]$**), respectively. In the case of iron ions, the decanuclear, $[Fe^{III}_{10}(L1)_6(\mu_3\text{-}O)(\mu_2\text{-}O)_4(\mu_2\text{-}HO)_5(Cl)(H_2O)_2]Cl_2$ (**$[Fe^{III}_{10}]$**), and pentanuclear, $[Fe^{III}_5(L1)_2(\mu_3\text{-}O)_2(\mu_2\text{-}O)(HL1)(Cl)(H_2L1)_3](PF_6)_3$ (**$[Fe^{III}_5]$**), complexes were obtained using metal chloride salts. On the other hand, two helical manganese complexes $[Mn_5(L1)_3(\mu_3\text{-}O)(NO_3)(OMe)_2(MeOH)](NO_3) \cdot 4MeOH \cdot H_2O$ (**$[Mn^{II}_3Mn^{III}_2]$**) and $[Mn_8(L1)_6(\mu_3\text{-}Cl)_2]Cl_2 \cdot 3C_2H_4Cl_2 \cdot 60H_2O \cdot 2DMF$ (**$[Mn^{II}_8]$**), were obtained by the reaction with manganese nitrate and chloride salts, respectively. The two complexes have the same μ_3-core units.

This research provided an insight into the coordination of counter anions as a controlling factor in the construction of multinuclear complexes. Halide ions were found to play a key role in the construction of multinuclear complexes with various structures.

---

[1] (a) J. E. Green, J. W. Choi, A. Boukai, Y. Bunimovich, E. Johnston-Halperin, E. DeIonno, Y. Luo, B. A. Sheriff, K. Xu, Y. S. Shin, H.-R. Tseng, J. F. Stoddart, and J. R. Heath, *Nature*, **2007**, *445*, 414. (b) E. R. Kay, D. A. Leigh, and F. Zerbetto, *Angew. Chem., Int. Ed.*, **2007**, *46*, 72. (c) G. A. Timco, S. Carretta, F. Troiani, F. Tuna, R. J. Pritchard, C. A. Muryn, E. J. L. McInnes, A. Ghirri, A. Candini, P. Santini, G. Amoretti, M. Affronte, and R. E. P. Winpenny, *Nat. Nanotechnol.*, **2009**, *4*, 173.

[2] (a) M. Ruben, J. Rojo, F. J. Romero-Salguero, L. H. Uppadine, and J.-M. Lehn, *Angew. Chem., Int. Ed.*, **2004**, *43*, 3644. (b) L. N. Dawe, K. V. Shuvaev, and L. K. Thompson, *Chem. Soc. Rev.*, **2009**, *38*, 2334. (c) G. A. Timco, T. B. Faust, F. Tuna, and R. E. P. Winpenny, *Chem. Soc. Rev.*, **2011**, *40*, 3067. (d) R. W. Saalfrank, H. Maid, and A. Scheurer, *Angew. Chem., Int. Ed.*, **2008**, *47*, 8794. (e) J. J. Bodwin, A. D. Cutland, R. Malkani, and V. L. Pecoraro, *Coord. Chem. Rev.*, **2001**, *216–217*, 489. (f) M. Affronte, S. Carretta, G. A. Timco, and R. E. P. Winpenny, *Chem. Commun.*, **2007**,1789.

[3] (a) N. Hoshino, A. M. Ako, A. K. Powell, and H. Oshio, *Inorg. Chem.*, **2009**, *48*, 3396–3407. (b) S. S. Tandon, S. D. Bunge, J. Sanchiz, and L. K. Thompson, *Inorg. Chem*., **2012**, *51*, 3270–3282. (c) C. Ding, C. Gao, S. Ng, B. Wang, and Y. Xie, *Chem. Eur. J.*, **2013**, *19*, 9961–9972. (d) L. F. Jones, A. Batsanov, E. K. Brechin, D. Collison, M. Helliwell, T. Mallah, E. J. L. McInnes, and S. Piligkos, *Angew. Chem. Int. Ed.*, **2002**, *41*, 4318–4321; *Angew. Chem.*, **2002**, *114*, 4494. (e) T. Taguchi, T. C. Stamatatos, K. A. Abboud, C. M. Jones, K. M. Poole, T. A. O'Brien, and G. Christou, *Inorg. Chem.*, **2008**, *47*, 4095–4108. (f) E. K. Brechin, M. Soler, J. Devidson, D. N. Hendrickson, S. Parsons, and G. Christou, *Chem. Commun.*, **2002**, 2252–2253. (g) C. Boskovic, E. K. Brechin, W. E. Streib, K. Folting, J. C. Bollinger, D. N. Hendrickson, and G. Christou, *J. Am. Chem. Soc.*, **2002**, *124*, 3725–3736. (h) E. K.Brechin, E. C. Sanudo, W. Wernsdorfer, C. Boskovic, J. Yoo, D. N. Hendrickson, A. Yamaguchi, H. Ishimoto, T. R. Concolino, A. L. Rheingold, and G. Christou, *Inorg. Chem.*, **2005**, *44*, 502–511. (i) D. Foguet-Albiol, T. A. O'Brien, W. Wernsdorfer, B. Moulton, M. J. Zawarotko, K. A. Abboud, and G. Christou, *Angew. Chem. Int. Ed.*, **2005**, *44*, 897–901; *Angew. Chem.* **2005**, 117, 919; j) W.-G. Wang, A.-J. Zhou, W.-X. Zhang, M.-L. Tong, X.-M. Chen, M. Nakano, C. C. Beedle, D. N. Hendrickson, J. Am. Chem. Soc. 2007, 129, 1014–1015.

[4] (a) R. Bagai, and G. Christou, *Chem. Soc. Rev*., **2009**, *38*, 1011–1026. (b) R. Inglis, L. F. Jones, C. J. Milios, S. Datta, A. Collins, S. Parsons, W. Wernsdorfer, S. Hill, S. P. Perlepes, S. Piligkos, and E. K. Brechin, *Dalton Trans.*, **2009**, 3403–3412. (c) R. Inglis, C. J. Milios, L. F. Jones, S. Piligkos, and E. K. Brechin, *Chem. Commun.*, **2012**, *48*, 181–190.

[5] (a) M. Yagi, and M. Kaneko, *Chem. Rev.*, **2001**, *101*, 21–35. (b) W. Ruettinger, M. Yagi, K. Wolf, S. Bernasek, and G. C. Dismukes, *J. Am. Chem. Soc.*, **2000**, *122*, 10353–10357.

[6] (a) R. Chakrabarty, P. S. Mukherjee, P. J. Stang, *Chem. Rev.*, **2011**, *111*, 6810−6918. (b) S. Leininger, B. Olenyuk, P. J. Stang, *Chem. Rev.*, **2000**, *100*, 853−908. (c) P. J. Stang, B. Olenyuk, *Acc. Chem. Res.*, **1997**, *30*, 502−518.

[7] (a) M. Fujita, M. Tominaga, A. Hori, B. Therrien, *Acc. Chem. Res.*, **2005**, *38*, 371−380. (b) M. Fujita, K. Umemoto, M. Yoshizawa, N. Fujita, T. Kusukawa, K. Biradha, *Chem. Commun.*, **2001**, 509−518.

[8] R. Chakrabarty, P. S. Mukherjee, and P. J. Stang, *Chem. Rev.*, **2011**, *111*, 6810–6918.

[9] (a) B. L. Schottel, H. T. Chifotides, and K. R. Dunbar, *Chem. Soc. Rev.*, **2008**, *37*, 68-83. (b) H. T. Chifotides, and K. R. Dunbar, *Acc. Chem. Res.*, **2013**, *46*, 894-906. (c) H. T. Chifotides, I. D. Giles, and K. R. Dunbar, *J. Am. Chem. Soc.*, **2013**, *135*, 3039-3055.

[10] T. Shiga, M. Noguchi, H. Sato, T. Matsumoto, G. N. Newton, and H. Oshio, *Dalton Trans.,* **2013**, *42*, 16185-16193.

[11] (a) T. Shiga, M. Matsumoto, M. Noguchi, T. Onuki, N. Hoshiono, G. N. Newton, M. Nakao, and H. Oshio, *Chem. Asian J.*, **2009**, *4*, 1660-1663. (b) H. Sato, L. Miya, K. Mitsumoto, T. Matsumoto, T. Shiga, G. N. Newton, and H. Oshio, *Inorg. Chem.*, **2013**, *52*, 9714-9716.

[12] H. Sato, M. Yamaguchi, T. Onuki, M. Noguchi, G. N. Newton, T. Shiga, and H. Oshio, *Eur. J. Inorg. Chem.*, **2015**, 2193-2198.

[13] G.M. Sheldrick, SADABS, Bruker AXS, Madison, USA, **1997**.

[14] G.M. Sheldrick, SHELXS97 and SHELXL97, University of Göttingen, Germany, **1997**.

[15] P. v.d. Sluis, and A. L. Spek, *Acta Cryst*, **1990**, *A46*, 194-201.

[16] G. N. Newton, T. Onuki, T. Shiga, M. Noguchi, T. Matsumoto, J. S. Mathieson, M. Nihei, M. Nakao, L. Cronin, and H. Oshio, *Angew. Chem. Int. Ed.*, **2011**, *50*, 4844-4848.

[17] BVS caluculation for **1**: 2.58 for Mn1, 1.97 for Mn4, and 2.07 for Mn5, assuming Mn^{II}. 2.74 for Mn2, and 3.11 for Mn3, assuming Mn^{III}.

[18] (a) X. Bao, W. Liu, J.-L. Liu, S. Gómez-Coca, E. Ruiz, M.-L. Tong, *Inorg. Chem.*, **2013**, *52*, 1099-1107. (b) R. Ishikawa, M. Nakano, A. Fuyuhiro, T. Takeuchi, S. Kimura, T. Kashiwagi, M. Hagiwara, K. Kindo, S. Kaizaki, S. Kawata, *Chem. Eur. J.*, **2010**, *16*, 11139-11144.

[19] BVS calculation for **2**: 1.959, 1.921, 1.987, and 2.038 for Mn1-Mn4, respectively, assuming Mn^{II}.

[20] (a) R.W. Saalfrank, N. Löw, S. Trummer, G.M. Sheldrick, M. Teichert, D. Stalke, *Eur. J. Inorg. Chem.*, **1998**, 559-563. (b) S. Romain, J. Rich, C. Sens, T. Stoll, J. Benet-Buchholz, A. Llobet, M. Rodriguez, I. Romero, R. Clérac, C. Mathonière, C. Duboc, A. Deronzier, M.-N. Collomb, *Inorg. Chem.*, **2011**, *50*, 5427-8436. (c) J.-Z. Hou, M. Li, Z. Li, S.-Z. Zhan, X.-C. Huang, D. Li, *Angew. Chem., Int. Ed.*, **2008**, *47*, 1711-1714.

CHAPTER 3

Control of Electronic States

3.1 Introduction

Multinuclear metal complexes show physical properties that can be altered upon the application of external stimuli such as temperature, light, electric field, and external magnetic field, and have attracted great attention due to their potential to function as molecular devices in future technologies.[1] The electronic states of transition metal ions and the interactions between neighboring centers can also be affected by external stimuli. Multinuclear systems with dynamic physical properties are therefore highly sought-after as useful molecular units. For example, the mixed valence manganese Keggin-type cluster, $[Mn^{IV}Mn^{III}_{12}O_6(OH)_2(OMe)_4(bemp)_6]^{4+}$ (**$[Mn_{13}]^{4+}$**, H_3bemp = 2,6-bis[*N*-(2-hydroxyethyl)iminomethyl]- 4-methylphenol) showed four quasi-reversible redox waves (Figure 3.1.). The initial state, **$[Mn_{13}]^{4+}$**, and its one and two electron oxidized states showed slow magnetic relaxation, and single molecule magnet (SMMs) behavior. The hysteresis loops at 0.04 K are amplified as the clusters are oxidized. This result indicated that the magnetic properties of multinuclear clusters clearly depend on their oxidation states.[2]

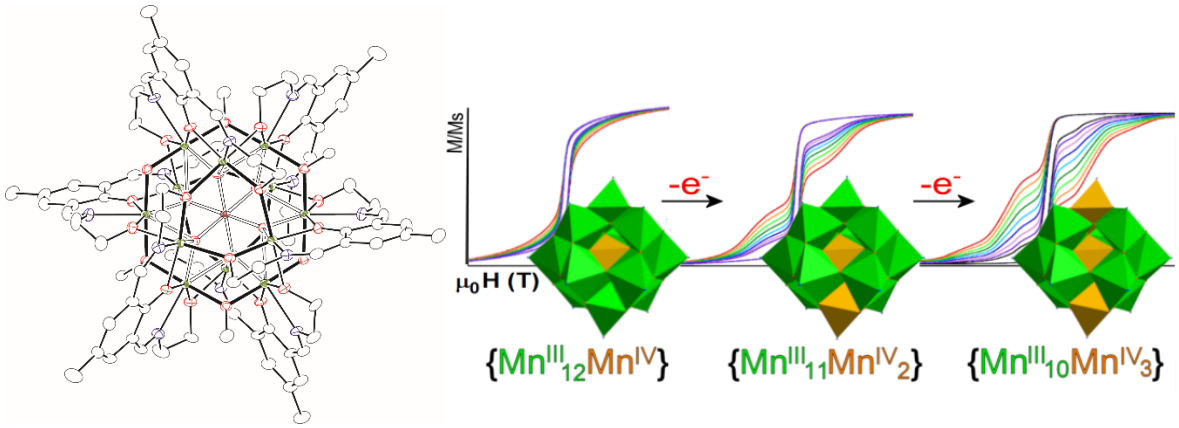

Figure 3.1. The structure and magnetic properties of $[Mn^{III}_{12}Mn^{IV}O_6(OH)_4(OMe)_2(bemp)_6](NO_3)_4$

When attempting to design molecular devices, the use of multidentate ligands is an excellent tactic as desirable multinuclear systems with regular arrays of metal ions can be designed and synthesized with a degree of confidence. Grid-type complexes are a good example of the artificial alignment of metal ions,[3] and Lehn and coworkers are pioneers in the research of such species, reporting many [*n* x *n*] grids,[4] including a tetranuclear iron(II) grid complex showing multi-step spin-cross over behavior.[5] Thompson et al. also investigated magnetic grid-type clusters using flexible amide ligands,[6] and recently, Mayer et al. and Sato et al. reported multi-step iron(II) spin-crossover (SCO) grids.[7] Tong et al. reported the syntheses and magnetic properties of hetero-metal grids,[8] while Hou et al. studied the ion-sensing and metal-exchange properties of copper grids.[9] Grid complexes can have many stable states due to the large number of metal ions, each of which has the potential to change electronic state. One of the advantage of such grid-type architectures is to provide an unusual coordination environment for the constituent metal ions. On this account, the development of new grid-type complexes is an important area of research.

In previous research, a series of metal complexes with a polypyridine multidentate ligand, H_2L1 (= 2,6-bis-[5-(2-pyridinyl)-1H-pyrazol-3-yl]-pyridine) showed various type of structures and physical properties which were dependent on the choice of metal ions and counter anions, as shown in the CHAPTER 2. H_2L1

has three distinct binding sites (one tridentate and two bidentate), and provides three different coordination environments to the [3 x 3] grid-type framework (central: six-coordinated octahedral geometry, edge: five-coordinated squarepyramidal geometry, corner: four-coordinated tetrahedral geometry). Metal ions which have different electronic states can be assembled into the grid molecule based on these three different coordination geometries. For instance, the nonanuclear cobalt [3 x 3] grid-type complex had three different electronic states of cobalt (Co^{III}_{HS}, Co^{II}_{LS} and Co^{II}_{HS}), and these different ions were located at the grid centre, edge and corner, respectively. This difference results in ferrimagnetic interactions between cobalt ions, leading to single molecular magnet (SMMs) behavior.[10]

In this research, the magnetic/electronic interactions between metal ions were probed with respect to their different redox states. Future targets of this research are to develop [3 x 3] grid-type complexes with various electronic states which may have properties such as switchable electronic states applicable to molecular devices. In the previous research on the homo-metal nonanuclear copper grid-type complexes, $[Cu^{II}_9(L1)_6](BF_4)_6$ (**$[Cu^{II}_9]$**), it was revealed that the coordination geometry at the grid center was altered by the oxidation state of the copper ions at the grid corners.[11] On the other hand, hetero-metallic copper and iron [3 x 3] grid complexes, $[Cu^{I}_2Cu^{II}_6Fe^{III}(L1)_6](BF_4)_5$ (**$[Cu^{I}_2Cu^{II}_6Fe^{III}]$**), showed five-step reversible redox processes.[11(c)] Considering the previous research into [3 x 3] grid systems and the redox properties of the constituent transition metal ions, copper and iron ions can be considered as promising candidates for the construction of stable, redox active materials. In this CHAPTER, the physical properties of redox isomers are investigated. The syntheses, structures, redox and detailed physical properties of homo-metallic **$[Cu_9]$** and hetero-metallic **$[Cu_8Fe]$** grids were studied. In the research on the homo-metal copper grids, the two-electron and four-electron reduced forms were isolated and their structures and magnetic properties were investigated. In the hetero-metal **$[Cu_8Fe]$** grids, two and three electron reduced forms and two electron oxidized forms were isolated and their single crystal structure analyses and magnetic measurements were carried out. SCO behavior in the **$[Cu_8Fe]$** grid is also investigated from the viewpoint of redox control.

Most of the reported grid-type complexes were constructed from homo-metal ions, and studies on redox-switchable physical properties are rare. The advantage of hetero-metal gird-type complexes is that the grid has not only different valence states but also a variety of magnetic properties which are due to the different constituent ions. In this research, an iron ion was introduced into a copper grid. The iron ion gives additional redox states to the grid, and different magnetic behavior was observed in its various oxidations states.

3.2 Experiments

3.2.1. Synthesis of $[Cu^{II}_9(L1)_6](BF_4)_6\cdot 3CH_3CN\cdot 1\text{-}PrOH\cdot 13H_2O$ ($[Cu^{II}_9]$)

To a solution of $Cu^{II}(BF_4)_2\cdot nH_2O$ (0.09 mmol, 28.7 mg) in 1-PrOH (1.5 mL) was added a mixture of H_2L1 (0.06 mmol, 22.3 mg) and triethylamine (0.095 mmol, 13.3 μL) in 1-PrOH (1.5 mL). The green suspension reaction mixture was stirred for 20 min. After addition of acetonitrile (7 mL) to the mixture the green suspension became a clear green solution. The resulting solution was filtered and left to stand for a few days after which green lozenge crystals of **$[Cu^{II}_9]$**$\cdot 3CH_3CN\cdot$1-PrOH$\cdot 13H_2O$ were obtained, and dried at ambient temperature (yield 20%). Anal. Calcd. for $C_{129}H_{96}N_{42}B_6F_{24}O_6Cu_9$ (**$[Cu^{II}_9]$**$\cdot$1-PrOH$\cdot 5H_2O$): C, 45.26; H, 2.83; N, 17.19. Found: C, 45.08; H, 2.72; N, 17.19. IR (KBr pellet, cm^{-1}): 3425.3, 1608.5, 1564.2, 1440.7, 1326.9, 781.1, 1037.6, 1083.9.

3.2.2. Synthesis of $[Cu^{I}_2Cu^{II}_7(L1)_6](PF_6)_4\cdot 4CH_3CN\cdot 2MeOH\cdot 2H_2O$ ($[Cu^{I}_2Cu^{II}_7]$) ($2e^-$ Reduced state)

Under strict anaerobic conditions, to a solution of $Cu^{II}(BF_4)_2\cdot nH_2O$ (0.09 mmol, 28.7 mg) and $[Cu^{I}(CH_3CN)_4](BF_4)$ (0.30 mmol, 95.9 mg) in MeOH (25 mL) was added a mixture of H_2L1 (0.40 mmol, 146.2 mg) and triethylamine (0.80 mmol, 111.5 mL) in MeOH (25 mL). After addition of acetonitrile (25 mL) to the stirred mixture, a dark yellowish-green solution was obtained. NH_4PF_6 (3.0 mmol 489 mg) was added to the solution and the resulting solution was allowed to stand at 40 °C. Brown lozenge crystals of **$[Cu^{I}_2Cu^{II}_7]$** $\cdot 4CH_3CN\cdot 2$MeOH$\cdot 2H_2O$ were obtained after a few days and were collected by suction filtration and air-dried (yield 15%). Anal. Calcd. for $C_{126}H_{84}N_{42}P_4F_{24}O_3Cu_9$ (**$[Cu^{I}_2Cu^{II}_7]$**$\cdot 3H_2O$): C, 44.69; H, 2.50; N, 17.37. Found: C, 44.67; H, 2.66; N, 17.37. IR (KBr pellet, cm^{-1}): 3447.5, 1600.8, 1565.1, 1437.8, 1327.9, 773.4, 845.7.

3.2.3. Synthesis of $[Cu^{I}_4Cu^{II}_5(L1)_6](PF_6)_2\cdot 8CH_2Cl_2\cdot 8H_2O$ ($[Cu^{I}_4Cu^{II}_5]$) ($4e^-$ Reduced state)

A dichloromethane solution (60 mL) of **$[Cu^{I}_2Cu^{II}_7]$** (6.78 mg, 0.002 mmol) was electrolyzed at 1.0 μA with *n*-Bu_4NPF_6 (38.74 g, 0.10 mmol). After few days, the light brown needle like crystals of **$[Cu^{I}_4Cu^{II}_5]$** were appeared on the Pt electrode.

3.2.4. Synthesis of $[Cu^{I}_2Cu^{II}_6Fe^{III}(L1)_6](BF_4)_5\cdot 9H_2O\cdot$MeOH ($[Cu^{I}_2Cu^{II}_6Fe^{III}]$)

Under strict anaerobic conditions, to a solution of $Cu^{II}(BF_4)_2\cdot nH_2O$ (0.08 mmol, 25.4 mg) and $Fe^{II}(BF_4)_2\cdot 6H_2O$ (0.12 mmol, 40.5 mg) in MeOH (7.5 mL) was added a mixture of H_2L1 (0.06 mmol, 21.9 mg) and triethylamine (0.12 mmol, 16.7 μL) in MeOH (5 mL). After addition of acetonitrile (6.5 mL) to the stirred mixture, a dark green solution was obtained. The resulting solution was slow evaporated for a few days after which green lozenge crystals of **$[Cu^{I}_2Cu^{II}_6Fe^{III}]\cdot 9H_2O\cdot$MeOH** were obtained and were collected by suction filtration and air-dried (yield 6.58 %). Anal. Calcd. for $C_{127}H_{100}B_5Cu_8F_{20}Fe_1N_{42}O_{10}$ (**$[Cu^{I}_2Cu^{II}_6Fe^{III}]\cdot 9H_2O\cdot$MeOH**): C, 45.23 (45.09); H, 2.99 (2.69); N, 17.44 (17.45).

3.2.5. Synthesis of $[Cu^{II}_8Fe^{III}(L1)_6](PF_6)_7\cdot 4H_2O\cdot$MeOH$\cdot 3CH_2Cl_2$ ($[Cu^{II}_8Fe^{III}]$) ($2e^-$ Oxidized state)

A dichloromethane solution (60 mL) of **$[Cu^{I}_2Cu^{II}_6Fe^{III}]$** (25.27 mg, 0.0080 mmol) was electrolyzed at +1.1 V vs. SCE with *n*-Bu_4NPF_6 (2.3460 g, 6.06 mmol). After electrolysis, the resulting mixture were allowed to stand for a day, affording the dark purple needle like crystals of **$[Cu^{II}_8Fe^{III}]$**. Yield 19.8 mg (66.3 %). Anal. Calcd. for $C_{130}H_{108}Cu_8F_{42}Fe_1N_{42}O_{11}P_7$ (**$[Cu^{II}_8Fe^{III}]$**$\cdot$4MeOH$\cdot 7H_2O$): C, 39.17 (38.90); H, 2.74 (2.71); N, 14.65 (14.66)%.

3.2.6. Synthesis of $[Cu^{I}_{4}Cu^{II}_{4}Fe^{III}(L1)_6](PF_6)_3\cdot 2H_2O\cdot 2MeOH\cdot 8CH_2Cl_2$ ($[Cu^{I}_{4}Cu^{II}_{4}Fe^{III}]$) ($2e^-$ Reduced state)

A dichloromethane solution (50 mL) of **$[Cu^{I}_{2}Cu^{II}_{6}Fe^{III}]$** (22.5 mg, 0.0071 mmol) was electrolyzed at -0.05 V vs. SCE with *n*-Bu_4NPF_6 (2.2952 g, 5.92 mmol). The brown block crystals of **$[Cu^{I}_{4}Cu^{II}_{4}Fe^{III}]$** was obtained by standing for one day. Yield 7.93 mg, (35.2 %). Anal. Calcd. for $C_{127}H_{86}Cu_8F_{18}Fe_1N_{42}O_3P_3$ ($[Cu^{I}_{4}Cu^{II}_{4}Fe^{III}]\cdot 2H_2O\cdot MeOH$): C, 47.19 (46.97); H, 2.78 (2.67); N, 17.97 (18.12)%.

3.2.7. Synthesis of $[Cu^{I}_{4}Cu^{II}_{4}Fe^{II}(L1)_6](PF_6)_2\cdot 5MeOH\cdot H_2O$ ($[Cu^{I}_{4}Cu^{II}_{4}Fe^{II}]$) ($3e^-$ Reduced state)

A dichloromethane solution (60 mL) of **$[Cu^{I}_{2}Cu^{II}_{6}Fe^{III}]$** (16.79 mg, 0.0053 mmol) was electrolyzed at −0.6 V vs. SCE with *n*-Bu_4NPF_6 (2.3096 g, 5.96 mmol). After electrolysis, standing gave light brown needle-like crystals of **$[Cu^{I}_{4}Cu^{I}_{4}Fe^{II}]$**. Yield 6.5 mg (40.6 %). Anal. Calcd. for $C_{131}H_{100}Cu_8F_{12}Fe_1N_{42}O_6P_2$ ($[Cu^{I}_{4}Cu^{II}_{4}Fe^{II}]\cdot 5MeOH\cdot H_2O$): C, 49.10 (48.98); H, 3.17 (3.14); N, 18.19 (18.31)%.

3.2.8. X-ray crystallography

A crystal was mounted on a MiTeGen Dual-Thickness MicroMounts, and data were collected using a Bruker SMART APEX II CCD Systems with Mo-$K\alpha$ radiation at 100 K (λ = 0.71073 Å).

3.2.9. Physical properties

Bulk electrolysis was carried out in a bulk electrolysis cell under nitrogen gas at room temperature with a porous carbon working electrode, a platinum-wire counter electrode, and an SCE reference electrode using a BAS 620A electrochemical analyzer. The measurements were performed in acetonitrile with 0.1 M tetra-*n*-butylammonium hexafluorophosphate (*n*-Bu_4NPF_6) as the electrolyte. Magnetic susceptibility data were collected using a Quantum Design MPMS-5S SQUID magnetometer. Magnetic data were corrected for the diamagnetism of the sample holder and for the diamagnetism of the sample using Pascal's constants. Mössbauer experiments were carried out using a ^{57}Co/Rh source in a constant-acceleration transmission spectrometer (Topologic System) equipped with an Iwatani HE05/CW404 Cryostat. The spectrum was recorded at 20 K. The spectrometer was calibrated using a standard α-Fe foil. UV-Vis-NIR absorption spectra were recorded on Shimadzu UV-3150 spectrometer.

3.3 Results and Discussion

3.3.1. Structures of copper grids

The reaction of $Cu(BF_4)_2{\cdot}nH_2O$ with H_2L and Et_3N in methanol/acetonitrile solution (3:7) yielded the nonanuclear grid complex $[Cu^{II}_9(L1)_6](BF_4)_6{\cdot}3CH_3CN{\cdot}1\text{-}PrOH{\cdot}13H_2O$ (**$[Cu^{II}_9]$**). The mixed-valence nonanuclear grid-type complex, $[Cu^{I}_2Cu^{II}_7(L1)_6](PF_6)_4{\cdot}4CH_3CN\cdot2MeOH{\cdot}2H_2O$ (**$[Cu^{I}_2Cu^{II}_7]$**), was prepared by the reaction of $[Cu(CH_3CN)_4](BF_4)$[12] with H_2L1, Et_3N, and NH_4PF_6 in methanol/acetonitrile solution under a nitrogen atmosphere. The two-electron reduced form of **$[Cu^{I}_2Cu^{II}_7]$**, $[Cu^{I}_4Cu^{II}_5(L1)_6](PF_6)_2{\cdot}8CH_2Cl{\cdot}8H_2O$ (**$[Cu^{I}_4Cu^{II}_5]$**) was prepared from **$[Cu^{II}_9]$** by constant-current electrolysis in dichloromethane solution with the $TBAPF_6$ as the electrolyte.

Single crystal X-ray structural analyses revealed that **$[Cu^{II}_9]$**, **$[Cu^{I}_2Cu^{II}_7]$** and **$[Cu^{I}_4Cu^{II}_5]$** have similar [3 x 3] grid-like structures, composed of six ligands and nine copper ions (Figure 3.2, Table 3.1). In the [3 x 3] grid, there are three different classes of coordination site: the central, the edge, and the corner positions. The central copper ion has an octahedral coordination geometry with six nitrogen atoms coordinating from two tridentate ligand sites. The copper ions on the edges have square-pyramidal coordination environments with one tridentate and one bidentate ligand site, while the corner copper ions are coordinated by two bidentate sites in a highly distorted tetrahedral manner. Bond valence sum calculations (Table 3.5) and charge balance considerations conclude that **$[Cu^{II}_9]$** were constructed by nine divalent copper ions, while two and four monovalent copper ions were included in **$[Cu^{I}_2Cu^{II}_7]$** and **$[Cu^{I}_4Cu^{II}_5]$**, respectively.

Overall grid shapes of **$[Cu^{II}_9]$**, **$[Cu^{I}_2Cu^{II}_7]$** and **$[Cu^{I}_4Cu^{II}_5]$** are substantially different, with **$[Cu^{II}_9]$** and **$[Cu^{I}_4Cu^{II}_5]$** possessing a regular square framework, and **$[Cu^{I}_2Cu^{II}_7]$** a distorted rhombic structure. The distortion originates from different coordination modes of the corner copper ions. All four copper ions in **$[Cu^{II}_9]$** and **$[Cu^{I}_4Cu^{II}_5]$** have similar geometries, while two of the copper ions on opposing corners of **$[Cu^{I}_2Cu^{II}_7]$** are especially distorted. The distortion parameters, τ_4, of the corner copper ions were calculated according to the following formula,[13]

$$\tau_4 = (360-(\alpha+\beta))/141,$$

where α and β are the two largest θ angles in a four-coordinate species, with $\tau_4 = 1$ a perfect tetrahedron, and $\tau_4 = 0$ perfect square planar geometry. In **$[Cu^{II}_9]$**, all τ_4 values are 0.60. The τ_4 values in **$[Cu^{I}_4Cu^{II}_5]$** are 0.63 for Cu3 and 0.67 for Cu5 and Cu6, while the τ_4 values in **$[Cu^{I}_2Cu^{II}_7]$** are in the range of 0.49-0.63; τ_4 = 0.56 for Cu3, 0.63 for Cu5, 0.49 for Cu7, and 0.62 for Cu9. The τ_4 values in **$[Cu^{I}_2Cu^{II}_7]$** suggest that Cu5 and Cu9 are close to tetrahedral, while Cu3 and Cu7 are more square planar. The coordination bond lengths about Cu3 and Cu7 ions are shorter than those of Cu5 and Cu9. These results imply that Cu5 and Cu9 are monovalent ions. The distortion of the overall square shape induces distortion of the coordination geometry of the central copper ion. In **$[Cu^{II}_9]$**, the central Cu1 has a compressed-type Jahn-Teller distortion along with bonds of the pyridine groups (N11 and N22) of the two central ligands. The center Cu1 ion of **$[Cu^{I}_4Cu^{II}_5]$** showed compressed-type Jahn-Teller distortion, same as **$[Cu^{II}_9]$**. On the other hand, the Cu1 ion of **$[Cu^{I}_2Cu^{II}_7]$** has an elongated Jahn-Teller distortion along with the pyrazolate groups (N31 and N33) and copper bond. Changing the oxidation states of the corner ions appears to induce different Jahn-Teller distortions of the copper nonanuclear [3 x 3] grid-type system.

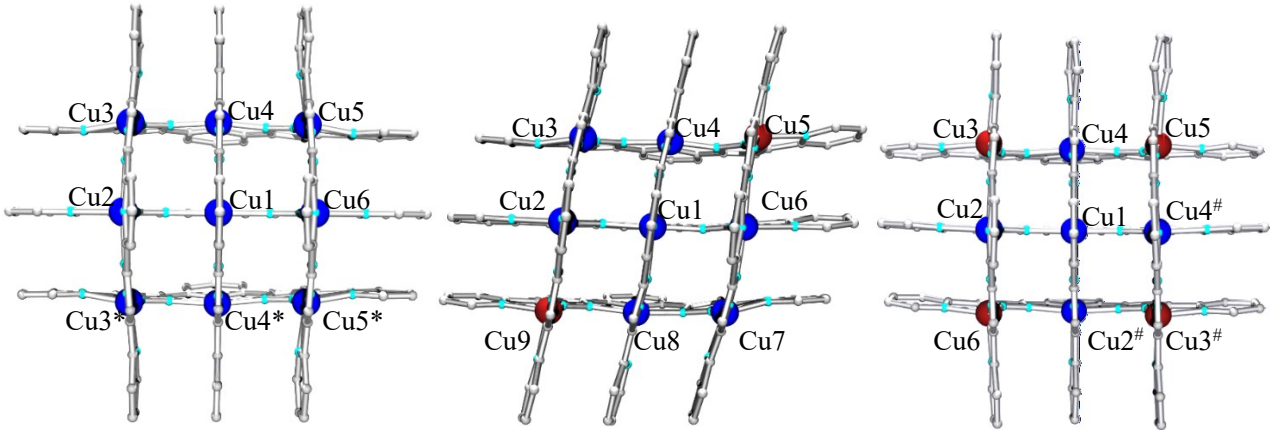

Figure 3.2. Crystal structures of **[Cu^{II}_9]** (left), **[$Cu^{I}_2Cu^{II}_7$]** (middle) and **[$Cu^{I}_4Cu^{II}_5$]** (left). Symmetry operation: *; +x, −y, +z; #; 1−x, +y, 1/2−z. Counter ions and solvent molecules were omitted for clarity. Color code: C, white; N, cyan; Cu^{II}, blue; Cu^{I}, scarlet.

3.3.2. Physical properties of the copper grid systems

Cyclic voltammetry of **[Cu^{II}_9]** and **[$Cu^{I}_2Cu^{II}_7$]** was measured in dichrolomethane solution (Figure 3.3) and both showed quasi-reversible four-step redox behavior. In the CV data of **[Cu^{II}_9]** and **[$Cu^{I}_2Cu^{II}_7$]**, the redox potentials of Cu(I)/Cu(II) are similar, implying that the electrochemically generated species from **[Cu^{II}_9]** and **[$Cu^{I}_2Cu^{II}_7$]** are identical in the same oxidation states. The rest potentials of **[Cu^{II}_9]** and **[$Cu^{I}_2Cu^{II}_7$]** were 0.50 V and 0.15 V, respectively, suggesting that **[$Cu^{I}_2Cu^{II}_7$]** is the two electron reduced species of **[Cu^{II}_9]**. Coulometry measurements of **[Cu^{II}_9]** and **[$Cu^{I}_2Cu^{II}_7$]** suggested that in **[$Cu^{I}_2Cu^{II}_7$]** electrolyses at -0.50 V and +0.80 V each corresponded to two electron processes. Thus, the redox waves at +0.44 V, +0.34 V, +0.09 V, and −0.04 V were assigned to [Cu^{II}_9] / [$Cu^{I}Cu^{II}_8$], [$Cu^{I}Cu^{II}_8$] / [$Cu^{I}_2Cu^{II}_7$], [$Cu^{I}_2Cu^{II}_7$] / [$Cu^{I}_3Cu^{II}_6$], and [$Cu^{I}_3Cu^{II}_6$] / [$Cu^{I}_4Cu^{II}_5$] processes, respectively. The CV data suggests that the two electron reduced species of **[$Cu^{I}_2Cu^{II}_7$]** is well-stabilized with a comproportionation constant K_c = 1.8 x 10^4. Observation of four reversible one electron redox processes implies the existence of electronic interactions between neighboring copper ions.

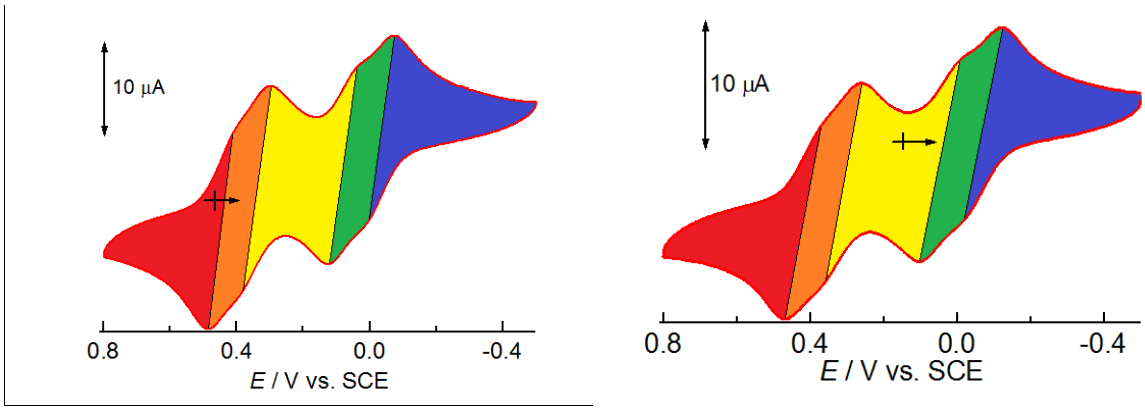

Figure 3.3. CV data of **[Cu^{II}_9]** (left) and **[$Cu^{I}_2Cu^{II}_7$]** (right) in $n$$Bu_4NPF_6$ / CH_2Cl_2. Reference electrode: SCE, working electrode: Pt, counter electrode: GC.

Magnetic susceptibilities of each oxidation state of copper grids were collected in the temperature range of 1.8 – 300 K (Figure 3.4). The $\chi_m T$ values for **[Cu$^{II}_9$]**, **[Cu$^{I}_2$Cu$^{II}_7$]** and **[Cu$^{I}_4$Cu$^{II}_5$]** at 300 K were 3.37, 3.10 and 1.87 emu mol^{-1} K, which were close to the expected values (3.38, 2.63 and 1.88 emu mol^{-1} K for g = 2.0) of nine and seven magnetically isolated Cu^{II} ions respectively. As the temperature was lowered, the $\chi_m T$ values decreased reaching 0.27, 0.40 and 0.83 emu mol^{-1} K at 1.8 K, respectively. The temperature dependence of both samples implied that antiferromagnetic interactions were dominant between Cu^{II} ions. Spin models (Figure 3.5) were applied to analyze magnetic data.[14] The resulting fitting parameters for **[Cu$^{II}_9$]** were g = 2.12, J_1 = -48 K, and J_2 = 0 K, in which J_2 was fixed to zero due to the complete non-overlap of magnetic orbitals. In general, Cu^{II} ions with compressed Jahn-Teller distortion have an unpaired electron in the d_z^2 orbital.[15] In **[Cu$^{II}_9$]**, the magnetic path defined as J_2 relates to the interaction between the equatorial ($d_{x^2-y^2}$) orbital of a Jahn-Teller compressed Cu^{II} ion (Cu1) with the Jahn-Teller elongated axial (d_z^2) orbitals of the edge Cu^{II} ions. The interacting orbitals are fully occupied and thus J_2 should be negligible. The best fitting parameters for **[Cu$^{I}_2$Cu$^{II}_7$]** were g = 2.16, J_1 = -40 K, and J_2 = -10 K. In this case, J_2 is non-negligible, as magnetic interactions between the equatorial plane of an elongated Cu^{II} ion (Cu1) and the axial orbital of elongated edge Cu^{II} ions (Cu2 & Cu6) are operative. The J_1 value is of similar order to that of **[Cu$^{II}_9$]** and due to the similarity of the magnetic interaction paths.

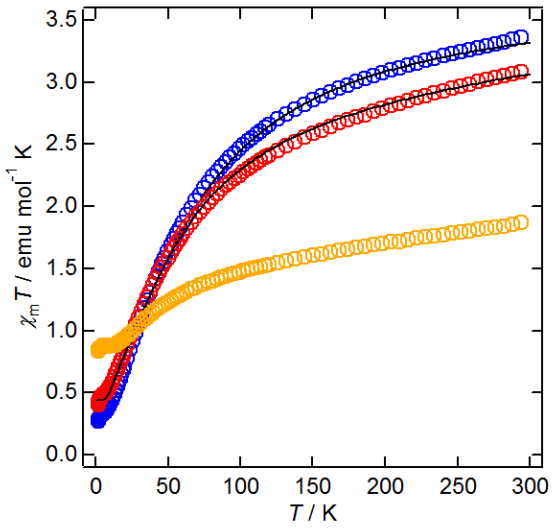

Figure 3.4. Magnetic susceptibilities of **[Cu$^{II}_9$]** (blue), **[Cu$^{I}_2$Cu$^{II}_7$]** (red) and **[Cu$^{I}_4$Cu$^{II}_5$]** (yellow) with fitting curves.

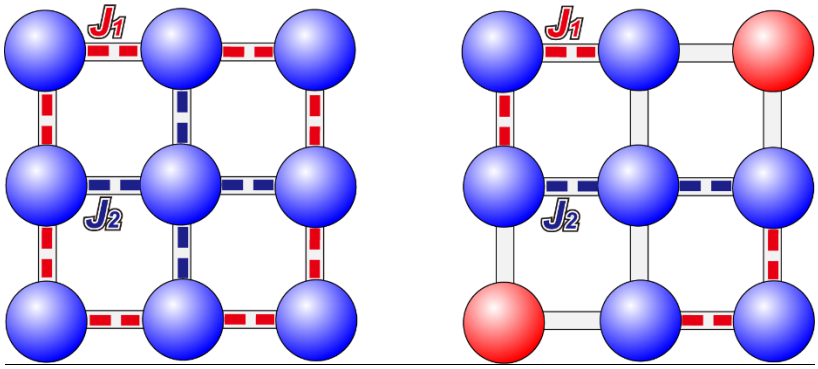

Figure 3.5. The spin models of **[Cu$^{II}_9$]** (left) and **[Cu$^{I}_2$Cu$^{II}_7$]** (right).

Table 3.1. Crystallographic parameters for copper systems.

	$[Cu^{II}_9]$	$[Cu^{I}_2Cu^{II}_7]$	$[Cu^{I}_4Cu^{II}_5]$.
Chemical formula	$C_{135}H_{78}N_{45}B_6F_{24}O_{14}Cu_9$	$C_{136}H_{90}N_{46}F_{24}O_4P_4Cu_9$	$C_{130}H_{78}Cl_8Cu_9F_{12}N_{42}O_5P_2$
Formula weight	3647.14g/mol	3584.28 g/mol	3453.74 g/mol
Temperature	100 K	100 K	100 K
Wavelength	0.71073 Å	0.71073 Å	0.71073 Å
Crystal system	Monoclinic	Monoclinic	Monoclinic
Space group	*C*2/m	$P2_1/c$	*C*2/c
A	28.890(2) Å	28.489(10) Å	25.551(10) Å
B	20.0394(16) Å	17.429(6) Å	19.424(8) Å
C	25.453(2) Å	30.812(11) Å	30.528(12) Å
α	-	-	-
β	94.5490(10)°	113.184(5)°	105.255(6) °
γ	-	-	-
Volume	14689(2) $Å^3$	14064(8) $Å^3$	14617(10) $Å^3$
Z	4	4	4
Density (calculated)	1.649 g/cm^3	1.693 g/cm^3	1.569 g/cm^3
Absorption coefficient	1.384 mm^{-1}	1.483 mm^{-1}	1.533 mm^{-1}
F(000)	7288	7188	6908
θ range for data collection	0.80 to 27.50°	2.34 to 22.05°	1.33 to 23.90 °
Index ranges	$-23 \le h \le 37$	$-31 \le h \le 31$	$-26 \le h \le 29$
	$-23 \le k \le 25$	$-19 \le k \le 19$	$-14 \le k \le 22$
	$-32 \le l \le 33$	$-34 \le l \le 27$	$-33 \le l \le 34$
Reflections collected	45543	57019	30543
Independent reflections	16895 [*R*(int) = 0.0429]	20494 [*R*(int) = 0.1212]	11283 [*R*(int) = 0.1903]
Data / restraints / parameters	16895 / 169 / 1119	20494 / 446 / 2118	11283 / 0 / 981
Goodness-of-fit on F^2	1.070	1.062	1.180
Final *R* indices [$I>2\sigma(I)$]	$R_1 = 0.0827$	*R*1 = 0.0814	*R*1 = 0.1229
	$wR_2 = 0.2375$	*wR*2 = 0.1887	*wR*2 = 0.2521
***R indices* (all data)**	$R_1 = 0.1161$	*R*1 = 0.1498	*R*1 = 0.2574
	$wR_2 = 0.2632$	*wR*2 = 0.2240	*wR*2 = 0.2970
Largest diff. peak and hole	1.439 and -1.090 $eÅ^{-3}$	1.679 and -0.673 $eÅ^{-3}$	1.825 and -1.210 $eÅ^{-3}$

Table 3.2. Bond lengths (Å) for $[Cu^{II}_9]$.

Cu1-N11	1.982(7)	Cu2-N9	1.979(8)	Cu3-N24	1.876(6)
Cu1-N22	1.992(6)	Cu2-N26	1.984(9)	Cu3-N2	1.877(6)
Cu1-N12	2.108(6)	Cu2-N25	2.011(6)	Cu3-N1	2.041(6)
Cu1-N14	2.132(7)	Cu2-N25	2.011(6)	Cu3-N23	2.044(7)
Cu1-N21	2.152(5)	Cu2-N8	2.294(8)		
Cu1-N21	2.152(5)				
Cu4-N20	1.977(5)	Cu5-N6	1.882(5)	Cu6-N13	1.967(7)
Cu4-N4	1.986(5)	Cu5-N16	1.902(5)	Cu6-N18	1.992(8)
Cu4-N5	2.002(5)	Cu5-N7	2.042(5)	Cu6-N17	2.017(5)
Cu4-N3	2.011(5)	Cu5-N15	2.066(6)	Cu6-N17	2.017(5)
Cu4-N19	2.283(6)			Cu6-N14	2.271(7)

Table 3.3. Bond lengths (Å) for **[$Cu^{I}_{2}Cu^{II}_{7}$]**.

Cu1-N11	1.974(9)	Cu2-N9	1.969(8)	Cu3-N37	1.866(9)
Cu1-N32	2.003(8)	Cu2-N39	1.986(8)	Cu3-N2	1.897(10)
Cu1-N10	2.069(8)	Cu2-N40	2.010(8)	Cu3-N1	2.041(9)
Cu1-N12	2.095(8)	Cu2-N38	2.012(9)	Cu3-N36	2.046(8)
Cu1-N31	2.149(8)	Cu2-N8	2.263(8)		
Cu1-N33	2.177(8)				
Cu4-N30	1.962(8)	Cu5-N6	1.918(8)	Cu6-N13	1.944(8)
Cu4-N4	1.985(8)	Cu5-N23	1.924(8)	Cu6-N25	1.978(9)
Cu4-N5	1.996(9)	Cu5-N22	2.132(9)	Cu6-N24	2.004(8)
Cu4-N3	1.997(9)	Cu5-N7	2.172(9)	Cu6-N26	2.015(8)
Cu4-N29	2.295(8)			Cu6-N14	2.301(9)
Cu7-N20	1.887(9)	Cu8-N34	1.953(8)	Cu9-N41	1.923(8)
Cu7-N27	1.890(9)	Cu8-N18	1.982(9)	Cu9-N16	1.923(9)
Cu7-N28	1.999(8)	Cu8-N17	2.005(9)	Cu9-N15	2.112(9)
Cu7-N21	2.000(9)	Cu8-N19	2.008(9)	Cu9-N42	2.139(9)
		Cu8-N35	2.337(9)		

Table 3.4. Bond lengths (Å) for **[$Cu^{I}_{4}Cu^{II}_{5}$]**.

Cu1-N11	2.038(11)	Cu2-N9	1.967(11)	Cu3-N16	1.894(14)
Cu1-N11	2.038(11)	Cu2-N18	1.998(12)	Cu3-N2	1.903(13)
Cu1-N12	2.117(12)	Cu2-N19	2.022(13)	Cu3-N1	2.139(15)
Cu1-N12	2.117(12)	Cu2-N17	2.024(14)	Cu3-N15	2.161(15)
Cu1-N10	2.130(13)	Cu2-N8	2.344(13)		
Cu1-N10	2.130(13)				
Cu4-N13	1.938(11)	Cu5-N6	1.923(13)	Cu6-N20	1.920(12)
Cu4-N5	1.992(14)	Cu5-N6	1.923(13)	Cu6-N20	1.920(12)
Cu4-N4	1.997(11)	Cu5-N7	2.158(14)	Cu6-N21	2.069(15)
Cu4-N3	2.013(14)	Cu5-N7	2.158(14)	Cu6-N21	2.069(15)
Cu4-N14	2.355(13)				

Table 3.5. Bond valence sum calculation and average bond lengths (Å) for copper systems.

		average bond length	Cu(I)	Cu(II)
$[Cu^{II}_9]$	Cu1	2.086(6)	1.78	2.23
	Cu2	2.056(7)	1.65	2.07
	Cu3	1.960(6)	1.68	2.11
	Cu4	2.052(5)	1.67	2.09
	Cu5	1.973(5)	1.62	2.03
	Cu6	2.053(7)	1.66	2.07
$[Cu^{I}_2Cu^{II}_7]$	Cu1	2.078(8)	1.82	2.28
	Cu2	2.048(8)	1.68	2.10
	Cu3	1.963(9)	1.67	2.09
	Cu4	2.047(8)	1.70	2.13
	Cu5	2.037(9)	1.40	1.75
	Cu6	2.048(8)	1.70	2.13
	Cu7	1.944(9)	1.73	2.17
	Cu8	2.057(9)	1.67	2.10
	Cu9	2.024(9)	1.43	1.79
$[Cu^{I}_4Cu^{II}_5]$	Cu1	2.095(12)	1.72	2.15
	Cu2	2.071(13)	1.61	2.01
	Cu3	2.024(14)	1.46	1.83
	Cu4	2.059(13)	1.68	2.10
	Cu5	2.041(14)	1.39	1.73
	Cu6	1.995(14)	1.52	1.91

3.3.4. Structure and electrochemical properties of $[Cu^{I}_{2}Cu^{II}_{6}Fe^{III}]$

Single crystal X-ray structural analyses revealed that **$[Cu^{I}_{2}Cu^{II}_{6}Fe^{III}]$** has a [3 x 3] grid-like structure, composed of six ligands, eight copper ions and one iron ion (Figure 3.6, left). In the [3 x 3] grid structure, the central metal ion has an octahedral coordination geometry and was assigned as an Fe(III) ion from bond lengths and bond valence sum calculations[16]. Two Cu(I) ions and Cu(II) ions were located at the grid corners in the opposite sites, while the edge sites of the grid were all Cu(II) ions. The cyclic voltammetry of **$[Cu^{I}_{2}Cu^{II}_{6}Fe^{III}]$** was measured in dichloromethane (Figure 3.6, right) and showed quasi-reversible five-step redox behavior. The rest potentials was +0.45 V. Comparing with the CV of **$[Cu^{I}_{2}Cu^{II}_{7}]$**, the four redox waves between +0.74 V and +0.27 V were assigned to the redox of copper ions located at the grid corners, while the redox wave observed at −0.13 V was the redox of Fe(III)/Fe(II).

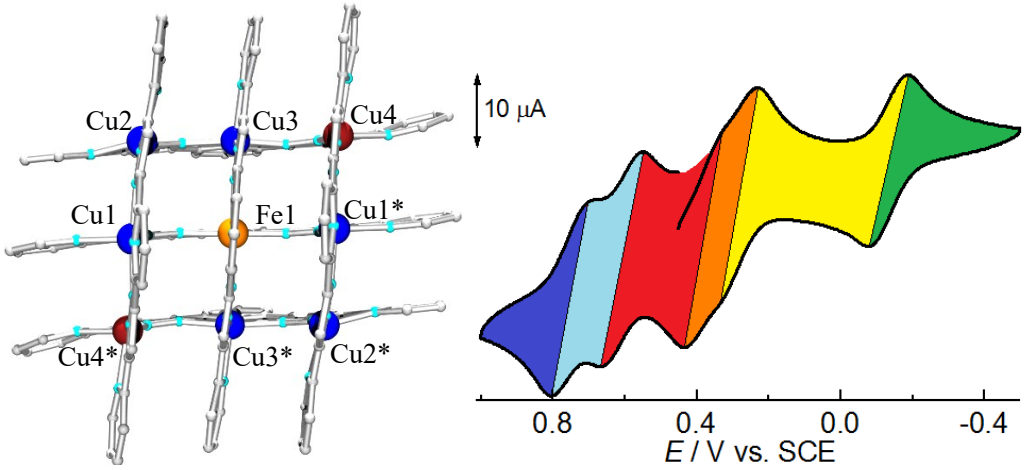

Figure 3.6. Molecular structures of **$[Cu^{I}_{2}Cu^{II}_{6}Fe^{III}]$** (left) and cyclic voltammogram (right). (Symmetry operation: *; 2−x, +y, 3/2−z. Counter ions and solvent molecules were omitted for clarity. Color code: C, white; N, cyan; Cu^{II}, blue; Cu^{I}, scarlet; Fe^{III}, orange)

Table 3.6. Bond lengths (Å) for **$[Cu^{I}_{2}Cu^{II}_{6}Fe^{III}]$**.

Fe1-N15	1.962(7)	Cu1-N19	1.974(5)	Cu2-N17	1.913(5)
Fe1-N11	1.958(6)	Cu1-N9	1.977(5)	Cu2-N2	1.912(5)
Fe1-N14	1.980(5)	Cu1-N20	1.992(5)	Cu2-N1	2.038(6)
Fe1-N14	1.980(5)	Cu1-N18	2.002(5)	Cu2-N16	2.046(6)
Fe1-N10	1.986(5)	Cu1-N8	2.234(5)		
Fe1-N10	1.986(5)				
Cu3-N4	1.970(5)	Cu4-N21	1.989(5)		
Cu3-N13	1.968(5)	Cu4-N6	1.986(5)		
Cu3-N5	1.995(5)	Cu4-N22	2.188(6)		
Cu3-N3	2.021(5)	Cu4-N7	2.216(6)		
Cu3-N12	2.251(5)				

3.3.5. Characterization of discrete electronic states

The structures of three electronic states of **[$Cu^{II}_8Fe^{III}$]** (2e⁻ Oxidized state), **[$Cu^{I}_4Cu^{II}_4Fe^{III}$]** (2e⁻ Reduced state), and **[$Cu^{I}_4Cu^{II}_4Fe^{II}$]** (3e⁻ Reduced state) at 100 K are shown in Figure 3.7. The crystallographic data and selected bond lengths for these complexes are listed in Tables 3.7 - 3.11, respectively. **[$Cu^{II}_8Fe^{III}$]** and **[$Cu^{I}_4Cu^{II}_4Fe^{II}$]** crystallized in the monoclinic space group *C*c, while **[$Cu^{I}_4Cu^{II}_4Fe^{III}$]** crystallized in the monoclinic space group *C*2/c. All compounds have similar [3x3] grid structures. The cationic unit of **[$Cu^{II}_8Fe^{III}$]** and **[$Cu^{I}_4Cu^{II}_4Fe^{II}$]** consisted of one crystallographically independent iron ion, eight copper ions and six ligands, while **[$Cu^{I}_4Cu^{II}_4Fe^{III}$]** consisted of half of a crystallographically independent iron ion, four copper ions and three ligands due to the existence of a C_2 axis at the grid centre, perpendicular to the grid surface. Seven, three and two hexafluorophosphate anions were observed in **[$Cu^{II}_8Fe^{III}$]**, **[$Cu^{I}_4Cu^{II}_4Fe^{III}$]** and **[$Cu^{I}_4Cu^{II}_4Fe^{II}$]**, respectively. These three oxidation states have similar [3 x 3] grid frameworks; metal ions were organized in a [3 x 3] grid like arrangement and three ligands coordinated to the metal ions from the upper and lower sides of the grid surface, respectively. While the metal ion located at the grid centers had a six-coordinate octahedral geometry, four grid edge sites were found to be in five-coordinate square pyramidal geometries, and the four corner sites in four-coordinate tetrahedral geometries, respectively. The coordination bond lengths, BVS calculations and charge valence suggested that metal ions on the edge positions were divalent copper ions. On the other hand, the central metal ion was a trivalent iron ion in **[$Cu^{II}_8Fe^{III}$]** and **[$Cu^{I}_4Cu^{II}_4Fe^{III}$]**, whereas a divalent iron ion was located at the grid centre in **[$Cu^{II}_4Cu^{II}_4Fe^{II}$]**. All metal ions located at the grid corners are divalent copper ions in **[$Cu^{II}_8Fe^{III}$]** and monovalent copper ions in **[$Cu^{I}_4Cu^{II}_4Fe^{III}$]** and **[$Cu^{I}_4Cu^{II}_4Fe^{II}$]**, respectively. All valence states of the four redox isomers including the initial state of **[$Cu^{I}_2Cu^{II}_6Fe^{III}$]** were summarized in Scheme 3.1. In comparison with **[$Cu^{I}_2Cu^{II}_6Fe^{III}$]** (initial state), the [3 x 3] grid framework is retained and close to a square shape due to the fact that the oxidation state of the grid corner ions equalizing.

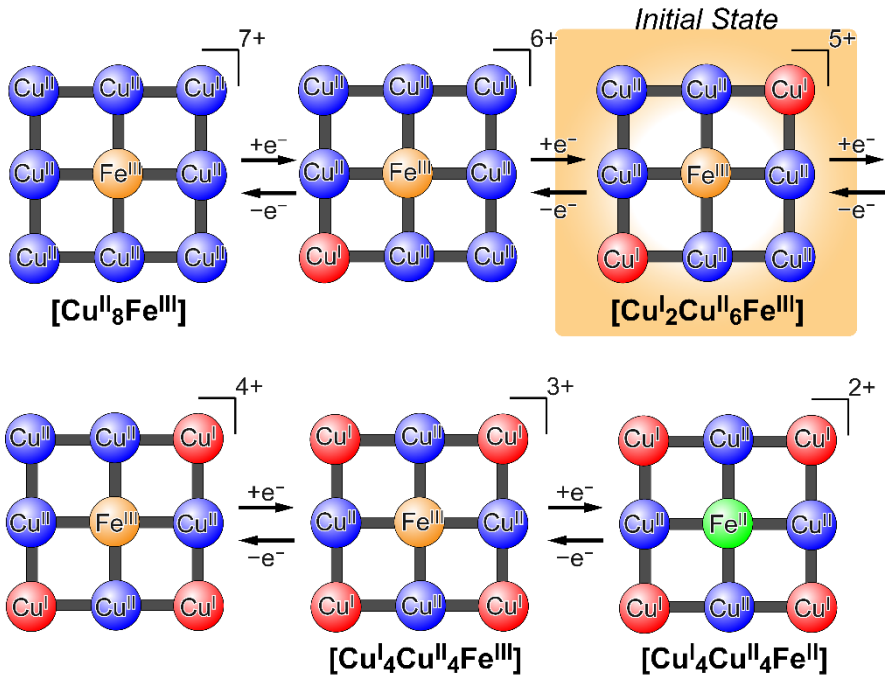

Scheme 3.1. Summary of valence state of four redox isomers.

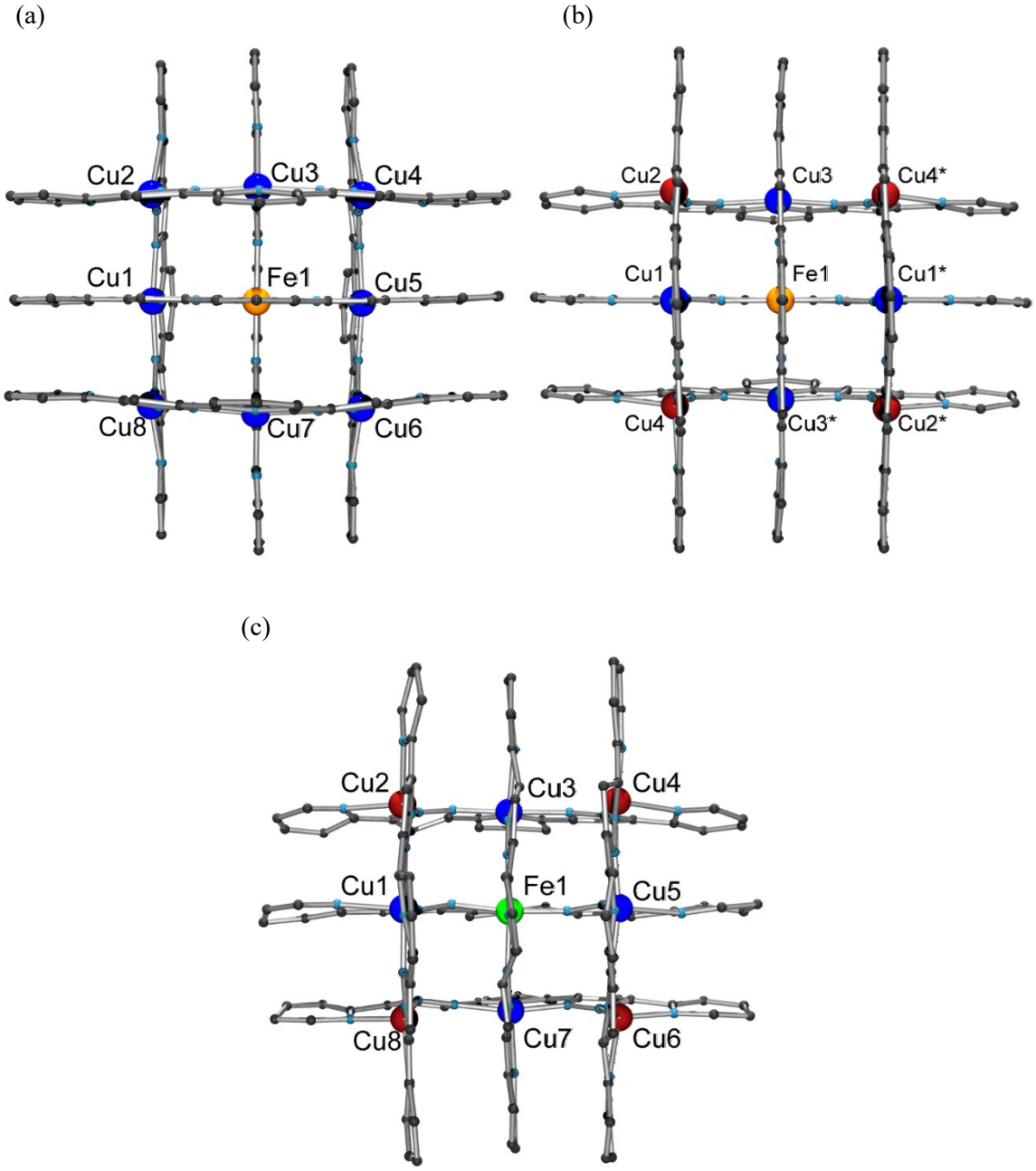

Figure 3.7. Molecular structure of (a) **[$Cu^{II}_8Fe^{III}$]**, (b) **[$Cu^{I}_4Cu^{II}_4Fe^{III}$]**, and (c) **[$Cu^{I}_4Cu^{II}_4Fe^{II}$]**. Symmetry operation: *; 1−x, +y, 1/2−z. Hydrogen atoms, solvent molecules and counter ions are omitted for clarity. Color code: blue, Cu(II), scarlet, Cu(I), orange, Fe(III), green, Fe(II), steelblue, N, gray20, C.

Table 3.7. Crystallographic parameters for copper-iron systems.

	$[Cu^{II}_8Fe^{III}]$	$[Cu^{I}_2Cu^{II}_6Fe^{III}]$	$[Cu^{I}_4Cu^{II}_4Fe^{III}]$	$[Cu^{I}_4Cu^{II}_4Fe^{II}]$.
Chemical formula	$C_{129}H_{78}Cu_8F_{42}FeN_{43}O_{10}P_7$	$C_{132}H_{84}B_5Cu_8F_{20}FeN_{44}O_7$	$C_{135}H_{104}Cl_{14}Cu_8F_{18}Fe_1N_{42}O_4P_3$	$C_{136}H_{120}B_2Cl_{12}Cu_8F_8FeN_{42}O_{11}$
Formula weight	3839.26 g/mol	3396.65 g/mol	3873.98 g/mol	3681.92 g/mol
Temperature	100 K	100 K	100 K	100 K
Wavelength	0.71073 Å	0.71073 Å	0.71073 Å	0.71073 Å
Crystal system	Monoclinic	Monoclinic	Monoclinic	Monoclinic
Space group	*C*c	*C*2/c	*C*2/c	*C*c
a	24.325(3) Å	20.503(3) Å	29.404(14) Å	23.73(3) Å
b	24.467(3) Å	28.300(4) Å	18.803(9) Å	20.54(3) Å
c	29.500(3) Å	25.100(3) Å	29.896(15) Å	26.77(3) Å
α	-	-	-	-
β	104.3780(14)°	95.352(2)°	116.291(7)°	97.12(2)°
γ	-	-	-	-
Volume	17007.(3) $Å^3$	14501(3) $Å^3$	14819.(13) $Å^3$	12950.(30) $Å^3$
Z	4	4	4	4
Density (calculated)	1.499 g/cm^3	1.556 g/cm^3	1.736 g/cm^3	1.889 g/cm^3
Absorption coefficient	1.233 mm^{-1}	1.342 mm^{-1}	1.597 mm^{-1}	1.740 mm^{-1}
F(000)	7636	6812	7772	7448
θ **range for data collection**	1.20 to 26.37°	1.423 to 28.757°	1.33 to 23.65°	1.32 to 20.87°
Index ranges	$-30 \le h \le 22$	$-22 \le h \le 27$	$-23 \le h \le 23$	$-12 \le h \le 23$
	$-30 \le k \le 28$	$-37 \le k \le 33$	$-20 \le k \le 20$	$-19 \le k \le 20$
	$-36 \le l \le 32$	$-33 \le l \le 32$	$-33 \le l \le 31$	$-26 \le l \le 24$
Reflections collected	43975	42795	30131	20882
Independent reflections	23666 [R(int) = 0.0566]	16436 [R(int) = 0.0627]	10975 [R(int) = 0.2085]	9673 [R(int) = 0.8415]
Data / restraints / parameters	23666 / 772 / 2116	16436 / 10 / 1042	10975 / 8 / 1057	9673 / 196 / 979
Goodness-of-fit on F^2	1.518	1.105	1.078	0.891
Final *R* indices [$I>2\sigma(I)$]	$R_1 = 0.0815$	$R_1 = 0.0772$	$R_1 = 0.1365$	$R_1 = 0.1413$
	$wR_2 = 0.2282$	$wR_2 = 0.2330$	$wR_2 = 0.3601$	$wR_2 = 0.2476$
R indices **(all data)**	$R_1 = 0.0875$	$R_1 = 0.1425$	$R_1 = 0.2484$	$R_1 = 0.4504$
	$wR_2 = 0.2314$	$wR_2 = 0.2821$	$wR_2 = 0.4206$	$wR_2 = 0.4027$
Largest diff. peak and hole	1.580 and -1.318 $eÅ^{-3}$	1.86 and -1.19 $eÅ^{-3}$	1.725 and -1.297 $eÅ^{-3}$	1.205 and -0.700 $eÅ^{-3}$

Table 3.8. Bond lengths (Å) for **[$Cu^{II}_8Fe^{III}$]**.

Fe1-N32	1.937(9)	Cu1-N9	1.969(9)	Cu2-N37	1.899(9)
Fe1-N11	1.947(9)	Cu1-N39	1.978(9)	Cu2-N2	1.900(9)
Fe1-N33	1.995(8)	Cu1-N40	1.982(9)	Cu2-N1	2.047(9)
Fe1-N31	1.987(8)	Cu1-N38	1.992(8)	Cu2-N36	2.042(9)
Fe1-N10	1.993(8)	Cu1-N8	2.244(9)		
Fe1-N12	1.995(9)				
Cu3-N4	1.953(10)	Cu4-N6	1.918(10)	Cu5-N13	1.940(9)
Cu3-N30	1.958(9)	Cu4-N23	1.932(10)	Cu5-N25	1.955(11)
Cu3-N3	1.996(9)	Cu4-N7	2.068(11)	Cu5-N24	1.972(9)
Cu3-N5	1.997(9)	Cu4-N22	2.079(9)	Cu5-N26	2.001(9)
Cu3-N29	2.218(9)			Cu5-N14	2.236(10)
Cu6-N20	1.904(12)	Cu7-N34	1.961(9)	Cu8-N16	1.904(10)
Cu6-N27	1.908(12)	Cu7-N18	1.967(10)	Cu8-N41	1.889(9)
Cu6-N28	2.050(11)	Cu7-N19	1.997(9)	Cu8-N15	2.038(9)
Cu6-N21	2.073(11)	Cu7-N17	2.007(9)	Cu8-N42	2.057(9)
		Cu7-N35	2.226(9)		

Table 3.9. Bond lengths (Å) for **[$Cu^{I}_4Cu^{II}_4Fe^{III}$]**.

Fe1-N10	1.947(16)	Cu1-N15	1.948(15)	Cu2-N13	1.964(14)
Fe1-N10	1.947(16)	Cu1-N16	1.960(15)	Cu2-N3	1.988(15)
Fe1-N22	1.968(19)	Cu1-N9	1.974(15)	Cu2-N1	2.127(16)
Fe1-N21	1.981(14)	Cu1-N15	2.023(16)	Cu2-N12	2.156(15)
Fe1-N21	1.981(14)	Cu1-N8	2.231(17)		
Fe1-N11	1.98(2)				
Cu3-N20	1.929(14)	Cu4-N17	1.936(18)		
Cu3-N4	1.940(12)	Cu4-N6	1.966(17)		
Cu3-N2	1.985(16)	Cu4-N18	2.099(15)		
Cu3-N5	2.005(15)	Cu4-N7	2.132(18)		
Cu3-N19	2.212(15)				

Table 3.10. Bond lengths (Å) for **[$Cu^{I}_4Cu^{II}_4Fe^{II}$]**.

Fe1-N31	1.94(19)	Cu1-N38	1.94(11)	Cu2-N37	2.05(11)
Fe1-N33	1.93(15)	Cu1-N39	1.95(14)	Cu2-N2	2.09(12)
Fe1-N11	1.90(13)	Cu1-N9	2.04(12)	Cu2-N1	2.16(14)
Fe1-N32	1.96(19)	Cu1-N40	2.13(10)	Cu2-N36	2.24(13)
Fe1-N10	2.02(14)	Cu1-N8	2.19(13)		
Fe1-N12	2.21(17)				
Cu3-N3	1.94(13)	Cu4-N6	1.97(9)	Cu5-N24	1.97(11)
Cu3-N30	2.1(2)	Cu4-N22	2.06(10)	Cu5-N25	1.99(13)
Cu3-N5	2.10(14)	Cu4-N23	2.1(3)	Cu5-N13	2.08(9)
Cu3-N4	2.07(16)	Cu4-N7	2.5(2)	Cu5-N26	2.15(13)
Cu3-N29	2.4(2)			Cu5-N14	2.37(15)
Cu6-N27	1.76(17)	Cu7-N18	2.00(14)	Cu8-N15	1.87(12)
Cu6-N28	2.06(15)	Cu7-N34	1.88(14)	Cu8-N16	1.99(10)
Cu6-N21	2.34(15)	Cu7-N17	1.98(16)	Cu8-N41	2.03(17)
Cu6-N20	2.4(2)	Cu7-N19	2.24(14)	Cu8-N42	2.39(14)
		Cu7-N35	2.42(14)		

Table 3.11. Bond valence sum calculation and average bond lengths (Å) for copper-iron systems.

		average bond length	Cu(I)	Cu(II)	Fe(II)	Fe(III)
	Fe1	1.976(9)	-	-	3.44	3.89
	Cu1	2.033(9)	1.74	2.50	-	-
	Cu2	1.972(9)	1.62	2.32	-	-
	Cu3	2.024(9)	1.78	2.55	-	-
$[Cu^{II}_8Fe^{III}]$	Cu4	1.999(10)	1.51	2.16	-	-
	Cu5	2.021(10)	1.81	2.59	-	-
	Cu6	1.984(11)	1.57	2.25	-	-
	Cu7	2.032(9)	1.74	2.50	-	-
	Cu8	1.972(9)	1.62	2.32	-	-
	Fe1	1.975(6)	-	-	3.44	3.89
	Cu1	2.036(5)	1.72	2.47	-	-
$[Cu^{I}_2Cu^{II}_6Fe^{III}]$	Cu2	1.977(6)	1.59	2.28	-	-
	Cu3	2.041(5)	1.71	2.45	-	-
	Cu4	2.095(6)	1.19	1.70	-	-
	Fe1	1.967(16)	-	-	3.51	3.98
	Cu1	2.027(16)	1.77	2.54	-	-
$[Cu^{I}_4Cu^{II}_4Fe^{III}]$	Cu2	2.059(15)	1.29	1.85	-	-
	Cu3	2.014(14)	1.83	2.62	-	-
	Cu4	2.033(17)	1.38	1.98	-	-
	Fe1	1.95(9)	-	-	3.69	4.18
	Cu1	2.04(8)	1.73	2.48	-	-
	Cu2	2.09(8)	1.20	1.72	-	-
	Cu3	2.07(8)	1.60	2.30	-	-
$[Cu^{I}_4Cu^{II}_4Fe^{II}]$	Cu4	2.13(12)	1.17	1.67	-	-
	Cu5	2.08(10)	1.54	2.21	-	-
	Cu6	2.06(9)	1.30	1.86	-	-
	Cu7	2.04(8)	1.78	2.55	-	-
	Cu8	2.03(8)	1.54	2.21	-	-

3.3.6. Structures of $[Cu^{II}_8Fe^{III}]$, $[Cu^{I}_2Cu^{II}_6Fe^{III}]$, $[Cu^{I}_4Cu^{II}_4Fe^{III}]$ and $[Cu^{II}_4Cu^{II}_4Fe^{II}]$

The maximum and minimum bond lengths around metal ions in **$[Cu^{II}_8Fe^{III}]$**, **$[Cu^{I}_2Cu^{II}_6Fe^{III}]$**, **$[Cu^{I}_4Cu^{II}_4Fe^{III}]$** and **$[Cu^{I}_4Cu^{II}_4Fe^{II}]$** are listed in Table 3.12.

Mössbauer spectra suggested that the iron ion in **$[Cu^{I}_4Cu^{II}_4Fe^{II}]$** was low-spin divalent and the other iron ions in **$[Cu^{II}_8Fe^{III}]$**, **$[Cu^{I}_2Cu^{II}_6Fe^{III}]$** and **$[Cu^{I}_4Cu^{II}_4Fe^{III}]$** were low-spin trivalent. However, the coordination bond lengths around the iron ions showed similar values, characteristic of low-spin iron(II) and iron(III) species. Coordination bond lengths about copper ions (Cu1, Cu3, Cu5 and Cu7) in the four sides of the grids are in the range of 1.91 – 2.30 Å, characteristic of Jahn-Teller distortion. However, those for the corner copper ions (Cu2, Cu4, Cu6 and Cu8) become longer upon reduction.

Table 3.12. The minimum and maximum bond lengths (Å).

		$[Cu^{II}_8Fe^{III}]$	$[Cu^{I}_2Cu^{II}_6Fe^{III}]$	$[Cu^{I}_4Cu^{II}_4Fe^{III}]$	$[Cu^{I}_4Cu^{II}_4Fe^{II}]$
Fe1	Min.	1.937(9)	1.957(7)	1.947(16)	1.90(7)
	Max	1.995(9)	1.986(5)	1.981(14)	1.99(8)
Cu1	Min.	1.969(9)	1.971(5)	1.948(15)	1.93(8)
	Max	2.244(9)	2.239(6)	2.231(17)	2.24(7)
Cu2	Min.	1.899(9)	1.902(6)	1.964(14)	1.92(7)
	Max	2.047(9)	2.043(6)	2.156(15)	2.21(10)
Cu3	Min.	1.953(10)	1.971(5)	1.929(14)	1.97(7)
	Max	2.218(9)	2.246(6)	2.212(15)	2.28(9)
Cu4	Min.	1.918(10)	1.986(5)	1.936(18)	1.90(7)
	Max	2.079(9)	2.209(6)	2.132(18)	2.36(12)
Cu5	Min.	1.940(9)	1.971(5)	1.948(15)	1.97(9)
	Max	2.236(10)	2.239(6)	2.231(17)	2.27(10)
Cu6	Min.	1.904(12)	1.902(6)	1.964(14)	1.91(8)
	Max	2.073(11)	2.043(6)	2.156(15)	2.18(9)
Cu7	Min.	1.961(9)	1.971(5)	1.929(14)	1.85(8)
	Max	2.226(9)	2.246(6)	2.212(15)	2.29(9)
Cu8	Min.	1.889(9)	1.986(5)	1.936(18)	1.81(8)
	Max	2.057(9)	2.209(6)	2.132(18)	2.37(7)

3.3.7. ^{57}Fe Mössbauer spectrum

The Mössbauer spectra of **[$Cu^{II}_8Fe^{III}$]** ($2e^-$ Oxidation state), **[$Cu^{I}_4Cu^{II}_4Fe^{III}$]** ($2e^-$ Reduction state) and **[$Cu^{I}_4Cu^{II}_4Fe^{II}$]** ($3e^-$ Oxidation state) at 20 K are depicted in Figure 3.8 and their Mössbauer parameters are listed in Table 3.13, respectively. Each of the Mössbauer spectra showed a quadrupole doublet. The values of isomer shift (δ) and quadrupole splitting (ΔE_Q) parameters for the central iron ions are in the LS-Fe^{III}, LS-Fe^{III}, and LS-Fe^{II} states for **[$Cu^{II}_8Fe^{III}$]**, **[$Cu^{I}_4Cu^{II}_4Fe^{III}$]** and **[$Cu^{I}_4Cu^{II}_4Fe^{II}$]**, respectively.

Table 3.13. Mössbauer parameters.

	δ (mm s^{-1})	ΔE_Q (mm s^{-1})	Area fraction (%)	Assign
[$Cu^{II}_8Fe^{III}$]	0.23	3.11	100	Fe^{III}_{LS}
[$Cu^{I}_4Cu^{II}_4Fe^{III}$]	0.20	2.99	100	Fe^{III}_{LS}
[$Cu^{I}_4Cu^{II}_4Fe^{II}$]	0.38	0.40	100	Fe^{II}_{LS}

Parameters are relative to the metallic iron.

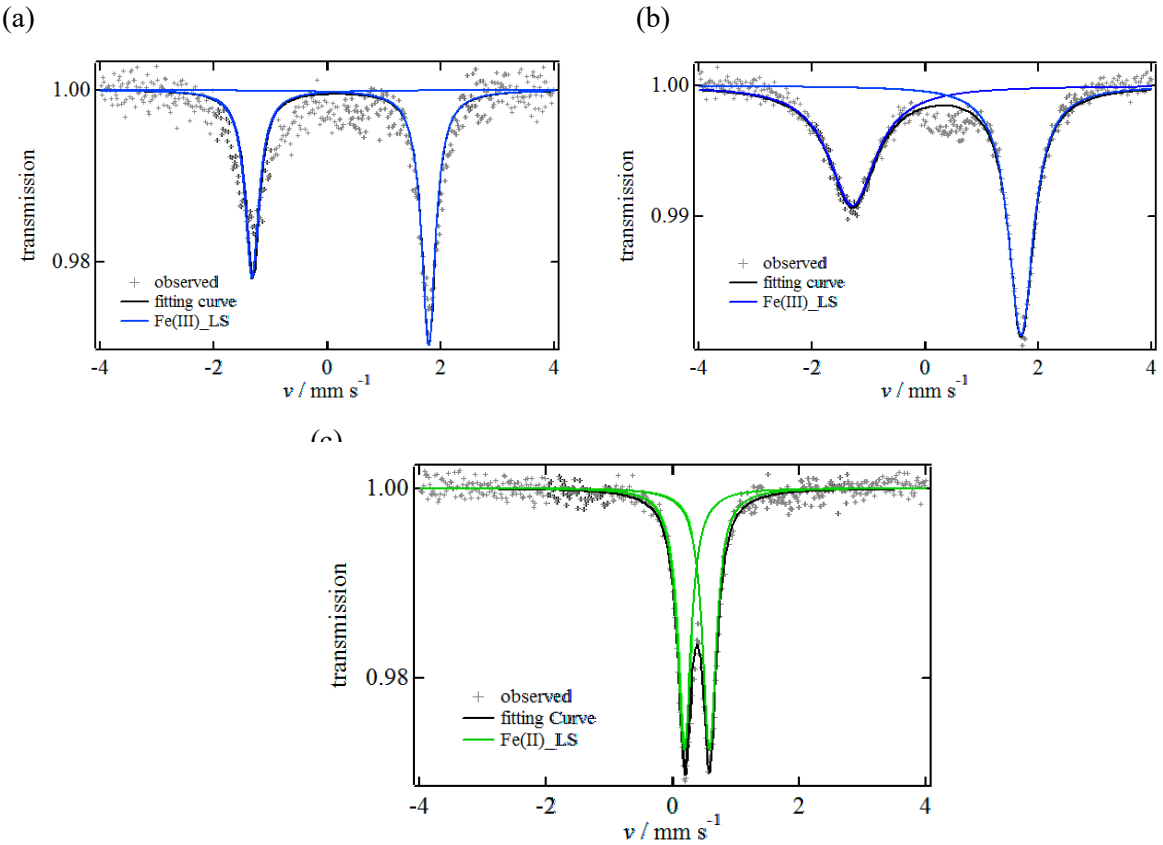

Figure 3.8. Mössbauer spectrum (a) **[$Cu^{II}_8Fe^{III}$]**, (b) **[$Cu^{I}_4Cu^{II}_4Fe^{III}$]**, (c) **[$Cu^{I}_4Cu^{II}_4Fe^{II}$]**.

3.3.8. Magnetic properties of $[Cu^{II}_8Fe^{III}(L1)_6](PF_6)_7$ (2 e^- Oxidized State)

The temperature dependence of magnetic susceptibility of **$[Cu^{II}_8Fe^{III}]$** was measured in the temperature range of 1.8 - 300 K under a magnetic field of 2 T, and the χ_mT versus T plots are shown in Figure 3.9(a). The χ_mT value at 300 K was 4.73 emu mol^{-1} K which is larger than the spin only value (3.375 emu mol^{-1} K) expected for one uncorrelated LS Fe^{III} ($S = 1/2$, $g_{Fe} = 2.0$) and eight Cu^{II} ($S = 1/2$, $g_{Cu} = 2.0$) ions. The gradual increase of the χ_mT values above 200 K suggests the occurrence of spin crossover for the central trivalent iron ion. The χ_mT values gradually decreased with decreasing temperature and reached a minimum value of 0.53 emu mol^{-1} K at 1.8 K. This suggests the occurrence of antiferromagnetic interactions between metal ions in **$[Cu^{II}_8Fe^{III}]$** and the spin ground state of $S = 1/2$ at the lowest temperature for **$[Cu^{II}_8Fe^{III}]$**. The magnetic data in the temperature range of 1.8 – 200 K were analyzed by MAGPACK[17] where the spin Hamiltonian was expressed as $H = -2J_1(S_1 \cdot S_2 + S_1 \cdot S_4 + S_1 \cdot S_6 + S_1 \cdot S_8) - 2J_2(S_2 \cdot S_3 + S_3 \cdot S_4 + S_4 \cdot S_5 + S_5 \cdot S_6 + S_6 \cdot S_7 + S_7 \cdot S_8 + S_8 \cdot S_9 + S_9 \cdot S_2)$. Note exchange coupling constants used were summarized in Scheme 3.2. The isotropic exchange constants, J_1 and J_2, signify exchange between the Fe^{III} and Cu^{II} pairs and Cu^{II} and Cu^{II} pairs, respectively. The solid curves in Figure 3.9(a) were drawn using parameters of $J_1 = -1.0$ K, $J_2 = -47$ K and $g_{ave.} = 2.38$. The field-dependence of magnetization data at 1.8 K is shown in Figure 3.9(b). The saturated value of 1.01 $N\beta$ at 5 T suggested that the ground state is $S = 1/2$.

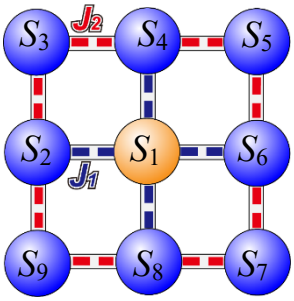

Fe^{III}_{LS}: $S_1 = 1/2$

Cu^{II}: $S_2 = S_3 = S_4 = S_5 = S_6 = S_7 = S_8 = S_9 = 1/2$

Scheme 3.2. Spin Hamiltonian model.

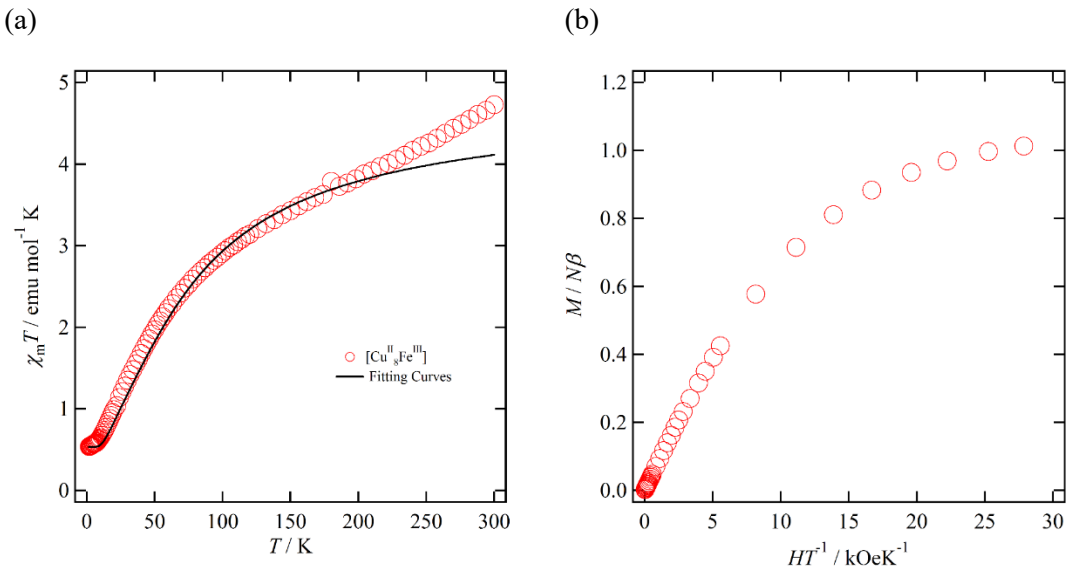

Figure 3.9. (a) Temperature dependence of magnetic susceptibility and (b) Field-dependence of magnetization curves at 1.8 K for **$[Cu^{II}_8Fe^{III}]$**.

3.3.9. Magnetic properties of $[Cu^{I}_{4}Cu^{II}_{4}Fe^{III}(L1)_6](PF_6)_3$ (2 e^- Reduced State)

The temperature dependence of the magnetic susceptibility data for **$[Cu^{I}_{4}Cu^{II}_{4}Fe^{III}]$** were collected in the temperature range of 1.8-300 K under a magnetic field of 2 T, and the $\chi_m T$ versus T plots are shown in Figure 3.10(a). The $\chi_m T$ value at 300 K was 1.99 emu mol^{-1} K which is close to the spin only value of 1.875 emu mol^{-1} K expected for one uncorrelated LS Fe^{III} (S = 1/2, g_{Fe} = 2.0) and four Cu^{II} (S = 1/2, g_{Cu} = 2.0) ions. The $\chi_m T$ values gradually decreased as the temperature was decreased and the value reached the minimum value of 1.12 emu mol^{-1} K at 1.8 K. The magnetic data suggests the occurrence of antiferromagnetic interactions between the Fe^{III} ion and Cu^{II} ions, and the spin ground state of **$[Cu^{I}_{4}Cu^{II}_{4}Fe^{III}]$** is S = 1/2 + 1/2 + 1/2. The magnetic data was analyzed by MAGPACK with the spin Hamiltonian of $H = -2J_1(S_1 \cdot S_2 + S_1 \cdot S_4 + S_1 \cdot S_6 + S_1 \cdot S_8)$, where the isotropic exchange constant, J_1, signifies exchange between the Fe^{III} and Cu^{II} pairs (Scheme 3.3). The solid curves in Figure 3.10(a) were drawn by using parameters of J_1 = −1.0 K and $g_{ave.}$ = 2.06. The field-dependence of magnetization data at 1.8 K is shown in Figure 3.10(b). The saturated value of 3.38 $N\beta$ at 5 T suggested that the ground state is S = 1/2 + 1/2 + 1/2.

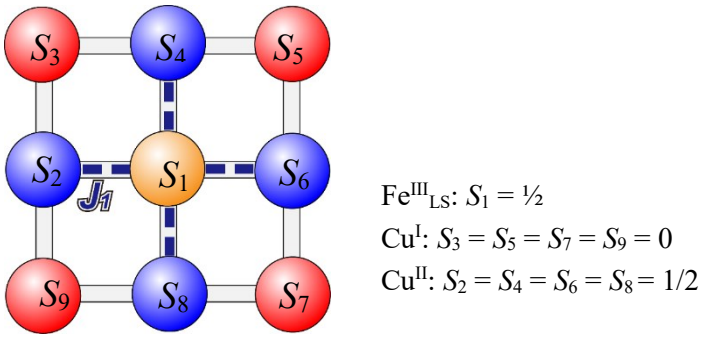

Scheme 3.3. Spin Hamiltonian model.

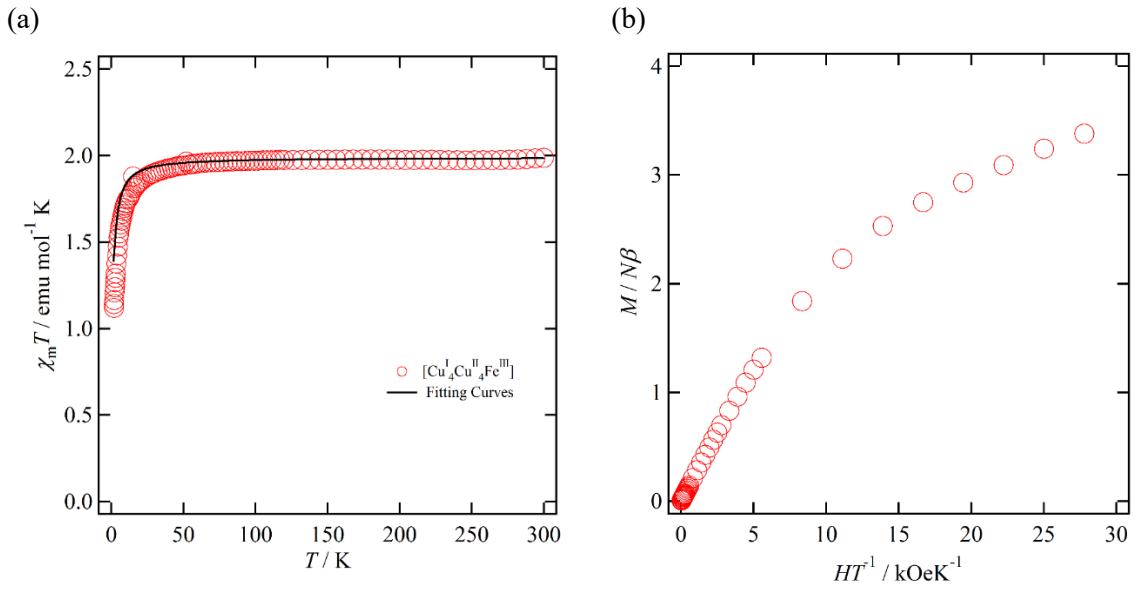

Figure 3.10. (a) Temperature dependence of magnetic susceptibility and (b) Field-dependence of magnetization curves at 1.8 K for **$[Cu^{I}_{4}Cu^{II}_{4}Fe^{III}]$**.

3.3.10. Magnetic properties of $[Cu^{I}_{4}Cu^{II}_{4}Fe^{II}(L1)_6](PF_6)_2$ (3 e^- Reduced State)

The temperature dependent magnetic susceptibility of **$[Cu^{I}_{4}Cu^{II}_{4}Fe^{II}]$** was measured in the temperature range of 2.0 - 300 K under a magnetic field of 1 T, and the $\chi_m T$ versus T plots are shown in Figure 3.11(a). The $\chi_m T$ value at 300 K was 1.63 emu mol^{-1} K which is close to the spin only value of 1.65 emu mol^{-1} K, which was expected for four uncorrelated Cu^{II} ions (S = 1/2, g_{Cu} = 2.1). The $\chi_m T$ values are almost constant at all temperatures measured. This suggests that the four paramagnetic Cu^{II} ions, located at the grid edges, are magnetically independent, isolated by diamagnetic Cu^{I} and Fe^{II} ions. The spin ground state of **$[Cu^{I}_{4}Cu^{II}_{4}Fe^{II}]$** can be expressed as S = 1/2 + 1/2 + 1/2 + 1/2 (Scheme 3.4). The field-dependence of magnetization data at 2.0 K is shown in Figure 3.11(b). The unsaturated value of 3.43 $N\beta$ at 4 T, agrees with the ground state of S = 1/2 + 1/2 + 1/2 + 1/2.

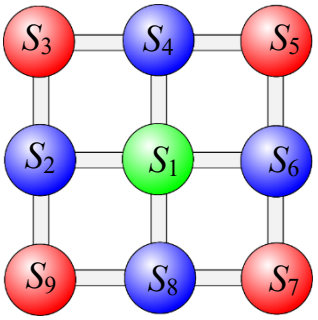

Fe^{II}_{LS}: $S_1 = 0$
Cu^{I}: $S_3 = S_5 = S_7 = S_9 = 0$
Cu^{II}: $S_2 = S_4 = S_6 = S_8 = 1/2$

Scheme 3.4. Spin Hamiltonian model.

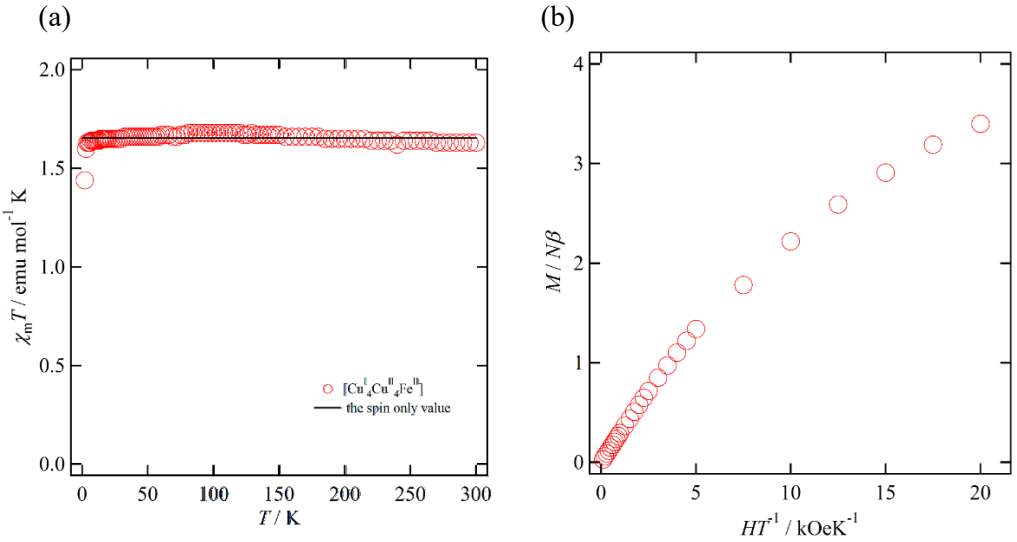

Figure 3.11. (a) Temperature dependence of magnetic susceptibility and (b) Field-dependence of magnetization curves at 1.8 K for **$[Cu^{I}_{4}Cu^{II}_{4}Fe^{II}]$**.

3.3.11. Spin Crossover behavior of $[Cu^{II}_8Fe^{III}(L1)_6](PF_6)_7$ (2 e^- Oxidized State)

Magnetic data for **$[Cu^{II}_8Fe^{III}]$** suggested the occurrence of spin crossover above 200 K, and we decided to measure variable temperature Mössbauer spectra. The results are shown in Figure 3.12 and Mössbauer parameters are listed in Table 3.14. Mössbauer spectrum at 20 K composed of a quadrupole doublet (δ= 0.23 mm s^{-1} with ΔE_Q = 3.11 mm s^{-1}), characteristic of LS-Fe^{III} state. After increasing temperature to 300 K, an additional doublet of HS-Fe^{III} (δ = 0.14 mm s^{-1} with ΔE_Q = 0.39 mm s^{-1}) appeared, which confirmed the occurrence of the spin crossover at the central Fe^{III} ion.

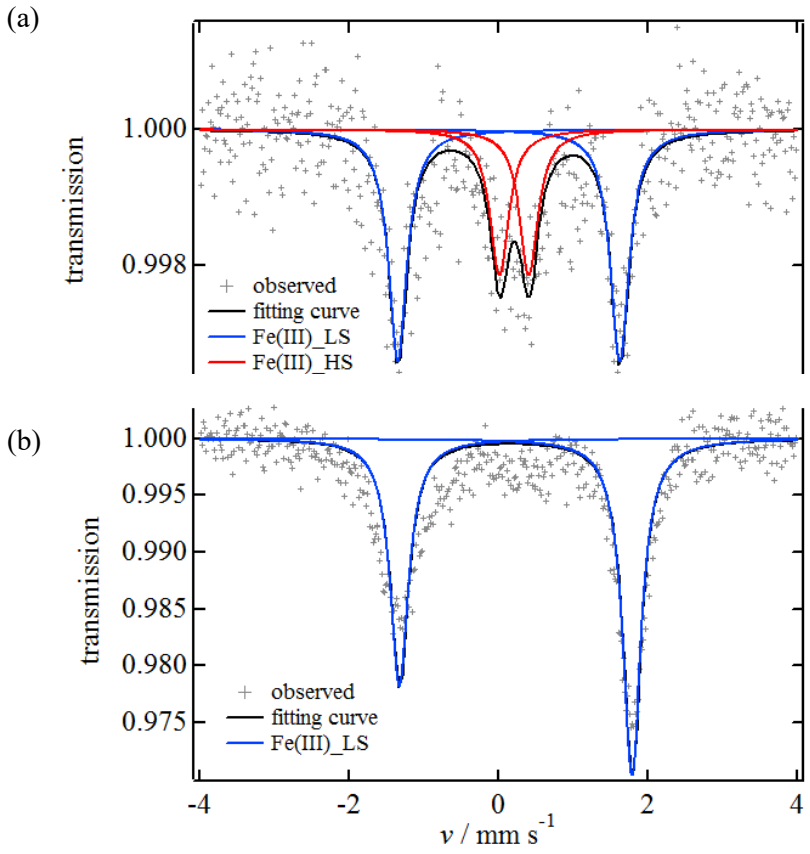

Figure 3.12. Variable temperature Mössbauer spectrum of **$[Cu^{II}_8Fe^{III}]$**.
((a) 300 K and (b) 20 K)

Table 3.14. Mössbauer parameters of **$[Cu^{II}_8Fe^{III}]$**.

	δ (mm s^{-1})		ΔE_Q (mm s^{-1})		Area fraction (%)	
T (K)	LS-Fe^{III}	HS-Fe^{III}	LS-Fe^{III}	HS-Fe^{III}	LS-Fe^{III}	HS-Fe^{III}
300	0.21	0.14	2.97	0.39	61	39
20	0.23	-	3.11	-	100	-

3.3.12. UV-vis spectra of $[Cu^{II}_8Fe^{III}]$, $[Cu^{I}_2Cu^{II}_6Fe^{III}]$ and $[Cu^{I}_4Cu^{II}_4Fe^{III}]$

UV-vis spectra of **$[Cu^{II}_8Fe^{III}]$**, **$[Cu^{I}_2Cu^{II}_6Fe^{III}]$** and **$[Cu^{I}_4Cu^{II}_4Fe^{III}]$** were measured (Figure 3.13). **$[Cu^{II}_8Fe^{III}]$**, **$[Cu^{I}_2Cu^{II}_6Fe^{III}]$** and **$[Cu^{I}_4Cu^{II}_4Fe^{III}]$** showed ligand-to- metal charge transfer (LMCT) band (from the pyrazolate group to the Fe(III) ion) at 639, 624, 606 nm, respectively. The observed redshift resulted from the weakened ligand field strength around the central Fe(III) ion upon oxidation of copper ions at the grid corners, causing the electron density on the pyrazolate ligands to shift towards the copper ions at the grid corners. In addition, coordination bond lengths between the central Fe(III) ion and the N donor (pyrazolate group) became longer (Table 3.15). It can be suggested that weakened ligand field on the central iron ion was derived from the oxidation of the copper ions and this is responsible for the occurrence of the spin crossover behavior of the central iron ion in **$[Cu^{II}_8Fe^{III}]$**.

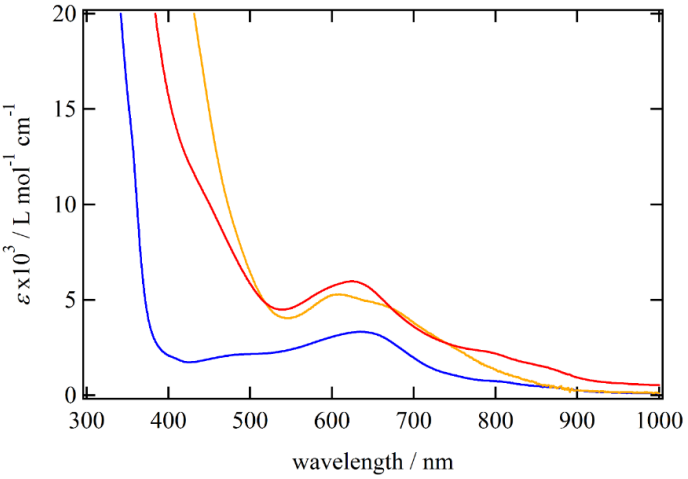

Figure 3.13. UV-Vis spectra of **$[Cu^{II}_8Fe^{III}]$** (blue), **$[Cu^{I}_2Cu^{II}_6Fe^{III}]$** (Red) and **$[Cu^{I}_4Cu^{II}_4Fe^{III}]$** (orange).

Table 3.15. Comparison of bond lengths (Å) around centre Fe(III) ion, and Σ value, which is distortion parameter about octahedral coordination environment.

		$[Cu^{II}_8Fe^{III}]$	$[Cu^{I}_2Cu^{II}_6Fe^{III}]$	$[Cu^{I}_4Cu^{II}_4Fe^{III}]$
Pyrazole	Fe-N1	1.993(8)	1.986(5)	1.937(16)
	Fe-N2	1.995(9)	1.986(5)	1.937(16)
	Fe-N3	1.987(8)	1.982(5)	1.974(13)
	Fe-N4	1.995(9)	1.982(5)	1.974(13)
Pyridine	Fe-Nα	1.947(9)	1.959(7)	2.00(2)
	Fe-Nβ	1.937(9)	1.957(7)	1.946(16)
Σ		97	95.76	90.8

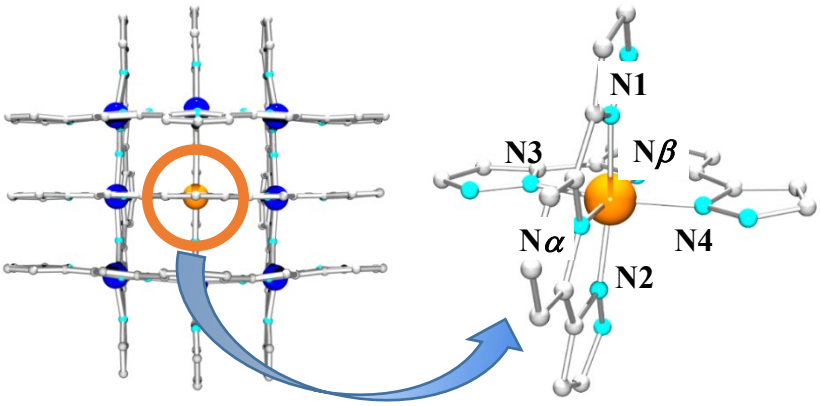

Scheme 3.5. Coordination environment around iron ion located at grid center.

3.4 Conclusion

In summary, three grid-type nonanuclear copper complexes, **[Cu^{II}_9]**, **[$Cu^{I}_2Cu^{II}_7$]** and **[$Cu^{I}_4Cu^{II}_5$]**, were synthesized using the multidentate polypyridine ligand H_2L1. Each compound has a similar [3 x 3] grid structure, but the distortion of the grids was different. The Jahn-Teller distortions of the central Cu^{II} ions of **[Cu^{II}_9]**, **[$Cu^{I}_2Cu^{II}_7$]** and **[$Cu^{I}_4Cu^{II}_5$]** differ due to the differences in the shape of the grid. The overall magnetic interactions can be explained by considering the effective magnetic orbitals based on the electronic configurations of Jahn-Teller distorted Cu^{II} centers. The electrochemical properties of **[Cu^{II}_9]** and **[$Cu^{I}_2Cu^{II}_7$]** were investigated by cyclic voltammetry and coulometry and both showed four-step reversible redox behavior.

In the hetero metal grid-type complex system, a series of redox isomers of **[$Cu^{II}_8Fe^{III}$]** ($2e^-$ Oxidation state), **[$Cu^{I}_4Cu^{II}_4Fe^{III}$]** ($2e^-$ Reduction state) and **[$Cu^{I}_4Cu^{II}_4Fe^{II}$]** ($3e^-$ Reduction state) were synthesized and the structures and electronic states were investigated. The electronic states of the copper ions at the grid corners and the central iron ion were characterized by means of X-ray structural analysis and Mössbauer spectral measurements. The magnetic properties were studied and the antiferromagnetic interactions or negligibly small interactions were suggested in the grids. It should be noted that the **[$Cu^{II}_8Fe^{III}$]** showed spin crossover behavior on the central trivalent iron ion, which was due to the varied ligand field strength accompanied with oxidation of the surrounding copper ions. The results suggest that the rigid multinuclear complexes with regular arrays of metal ions may function as switchable molecular units and have potential applications in molecular devices.

---

[1] (a) J. E. Green, J. W. Choi, A. Boukai, Y. Bunimovich, E. Johnston-Halperin, E. DeIonno, Y. Luo, B. A. Sheriff, K. Xu, Y. S. Shin, H.-R. Tseng, J. F. Stoddart, and J. R. Heath, *Nature*, **2007**, *445*, 414-417. (b) E. R. Kay, D. A. Leigh, and F. Zerbetto, *Angew. Chem. Int. Ed.*, **2007**, *46*, 72-191. (c) C. S. Lent, *Science*, **2000**, *288*, 1597-1599. (d) O. Sato, J. Tao, and Y.-Z. Zhang, *Angew. Chem. Int. Ed.*, **2007**, *46*, 2152-2187. (e) G. N. Newton, M. Nihei, and H. Oshio, *Eur. J. Inorg. Chem.*, **2011**, *20*, 3031-3042. (f) G. A. Timco, S. Carretta, F. Troiani, F. Tuna, R. J. Pritchard, C. A. Muryn, E. J. L. McInnes, A. Ghirri, A. Candini, P. Santini, G. Amoretti, M. Affronte, and R. E. P. Winpenny, *Nat. Nanotech.*, **2009**, *4*, 173-178.

[2] G. N. Newton, S. Yamashita, K. Hasumi, J. Matsuno, N. Yoshida, M. Nihei, T. Shiga, M. Nakao, H. Nojiri, W. Wernsdorfer, and H. Oshio, *Angew. Chem. Int. Ed.*, **2011**, *50*, 5716-5720.

[3] (a) M. Ruben, J. Rojo, F. J. Romero-Salguero, L. H. Uppadine, and J.-M. Lehn, *Angew. Chem. Int. Ed.*, **2004**, *43*, 3644-3662. (b) L. K. Thompson, O. Waldmann, and Z. Xu, *Coord. Chem. Rev.*, **2005**, *249*, 2677-2690. (c) L. N. Dawe, K. V. Shuvaev, and L. K. Thompson, *Chem. Soc. Rev.*, **2009**, *38*, 2334-2359.

[4] (a) G.S. Hanan, D. Volkmer, U. S. Schubert, J. M. Lehn, G. Baum, and D. Fenske, *Angew. Chem. Int. Ed. Engl.*, **1997**, *36*, 1842-1844. (b) M. Ruben, E. Breuning, E. Barboiu, J.-P. Gisselbrecht, and J.-M. Lehn, *Chem. Eur. J.*, **2003**, *9*, 291-299. (c) A. R. Stefankiewicz, G. Rogez, J. Harrowfield, A. N. Sobolev, A. Madalan, J. Huuskonen, K. Rissanen, and J.-M. Lehn, *Dalton Trans.*, **2012**, *41*, 13848-13855.

[5] M. Ruben, E. Breuning, J.-M. Lehn, V. Ksenofontov, F. Renz, P. Gütlich, and G. Vaughan, *Chem. Eur. J.*, **2003**, *9*, 4422-4429.

[6] (a) M. U. Anwar, L. K. Thompson, L. N. Dawe, F. Habibb, and M. Murugesu, *Chem. Commun.*, **2012**, *48*, 4576-4578. (b) M. U. Anwar, K. V. Shuvaev, L. N. Dawe, and L. K. Thompson, *Inorg. Chem.*, **2011**, *50*, 12141-12154.

[7] (a) B. Schneider, S. Demeshko, S. Dechert, and F. Meyer, *Angew. Chem. Int. Ed.*, **2010**, *49*, 9274-9277. (b) D.-Y. Wu, Y. Einaga, and C.-Y. Duan, *Angew. Chem. Int. Ed.*, **2009**, *48*, 1475-1478.

[8] X. Bao, W. Liu, L.-L. Mao, S.-D. Jiang, J.-L. Liu, Y.-C. Chen, M.-L. Tong, *Inorg. Chem.*, **2013**, *52*, 6233-6235.

[9] Y. Han, N. F. Chilton, M. Li, C. Huang, H. Xu, H. Hou, B. Moubaraki, S. K. Langley, S. R. Batten, Y. Fan, K. S. Murray, *Chem. Eur. J.*, **2013**, *19*, 6321-6328.

[10] (a) T. Shiga, T. Matsumoto, M. Noguchi, T. Onuki, N. Hoshino, G. N. Newton, M. Nakano, and H. Oshio, *Chem. Asian J.*, **2009**, *4*, 1660-1663. (b) G. N. Newton, T. Onuki, T. Shiga, M. Noguchi, T. Matsumoto, J. S. Mathieson, M. Nihei, L Cronin, and H Oshio, *Angew. Chem. Int. Ed.*, **2011**, *50*, 4844-4848.

[11] (a) M. Noguchi, Master Thesis, University of Tsukuba, 2008. (b) L. Miya, Bachelor Thesis, University of Tsukuba, 2009. (c) H. Sato, Master Thesis, University of Tsukuba, 2012.

[12] G. J. Kubas, *Inorg. Synth.*, **1979**, *19*, 90.

[13] L. Yang, D. R. Powell, and R. P. Houser, *Dalton Trans.* **2007**, 955.

[14] J. J. Borras-Almenar, J. M. Clemente-Juan, E. Coronado, and B. S. Tsukerblat, *J. Comput. Chem.* **2001**, *22*, 985.

[15] (a) M. A. Halcrow, *Chem. Soc. Rev.*, **2013**, *42*, 1784. (b) N. K. Solanki, E. J. L. E McInnes, F. E. Mabbs, S. Radojevic, M. McPartlin, N. Feeder, J. E. Davies, M. A. Halcrow, *Angew. Chem., Int. Ed.*, **1998**, *37*, 2221. (c) A. J. Bridgeman, M. A. Halcrow, M. Jones, E. Krausz, N. K. Solanki, *Chem. Phys. Lett.*, **1999**, *314*, 176.

[16] I. D. Brown, D. Altermatt, *Acta Cryst.*, **1985**, *B41*, 244-247.

[17] J. J. Borràs-Almenar, J. M. Clemente-Juan, E. Coronado, and B. S. Tsukerblat, *J. Comout. Chem.*, **2001**, *22*, 985.

CHAPTER 4

Further Exploration of Grids

4.1 Introduction

A mixed valence complex shows interesting physical properties depending on the delocalization of electrons between metal ions. It is well-known that strong light absorption in the near-infrared region[1], unusually strong magnetic interactions[2] and specific electronic conductivity[3] are specific physical properties that can be associated with charge transfer between hetero-valent metal ions. Therefore, discrete mixed valence complexes have been studied from a fundamental viewpoint, as well as a more applied perspective with a view to the development of prototype molecular devices.[4] To date, various classes of discrete mixed valence complexes have been reported and the strength of intramolecular electronic communication investigated.[5] Polyferrocenyl species and carboxylate bridged ruthenium complexes are among of the most famous mixed valence systems.[6] In these systems, control of electronic interactions can be achieved by modulation of the bridging and auxiliary ligands, but there are some structural restrictions and some limitations of electronic interactions. Against such a background, the exploration and construction of new mixed valence systems is very important for development of novel functional molecular devices.

The ruthenium multinuclear complex, known as the Creutz-Taube ion, $[Ru(NH_3)_5\text{-pz-}Ru(NH_3)_5]^{5+}$ (pz = pyrazine, Figure 4.1) is the archetypal mixed valence system.[7] The oxidation state of this complex can be described as $[Ru^{II}\text{-}Ru^{III}]$, but the complex also has two energetically equivalent redox states, $Ru^{II}\text{-}Ru^{II}$ and $Ru^{III}\text{-}Ru^{III}$, therefore, electron transfer can occur freely between the hetero-valent ruthenium ions. The Creutz-Taube complex was classified as a Class III mixed valence compound based on the Robin-Day classification.[8] Thus, the valence states of both ruthenium ions were considered as $Ru^{+2.5}$. Such mixed valence state has been studied by various optical measurements, and electron delocalization between ruthenium ions in the mixed valence Creutz-Taube complex was confirmed by existence of an IVCT (= Intervalence charge transfer) band in the near infrared region. Many mixed valence ruthenium polynuclear complexes were studied and synthetic strategies for mixed valence systems have been established. Ruthenium complexes have been used for research in multi-electron transfers (Figure 4.2)[9] and water oxidation catalysts.[10] In this research, a ruthenium ion was selected to build a unique mixed-valence state grid compound.

In this work, grid molecules were selected for building mixed valence systems where substantial electronic interactions are expected between ruthenium ions in a grid. In the previous research as shown CHAPTER III, the [3 x 3] grid-type complex with the polypyridine ligand H_2L1 (= 2,6-bis-[5-(2-pyridinyl)-1H-pyrazol-3-yl]-pyridine) has three different coordination sites, and the grid-type complexes with H_2L1 have three different types of coordination sites. This structural limitation would interfere with the electron transfer between ruthenium ions, with metal ions in the different coordination environments having different orbital energies. It can be presumed that the frontier energy level between metal ions and bridging ligands does not so much for charge transfer interactions. This was confirmed as the mixed valence [3 x 3] grid-type complexes in the previous sections did not show charge transfer bands between hetero-valent metal ions. In this research, the polypyridine multidentate ligand, HL2 (=2-phenyl-4,5-bis{6-(3,5-dimethylpyrazol-1-yl)pyrad-2-yl}-1H-imidazole, Figure 4.3)[11] which provides equivalent coordination sites were used for the construction of a new ruthenium [2 x 2] grid-type complex. It is, therefore, expected that strong electronic interactions between mixed valence ruthenium ions through imidazolate anion will be operative. In this work, a tetranuclear ruthenium [2 x 2] grid-type complex was synthesized, and its structure and redox properties were

investigated.

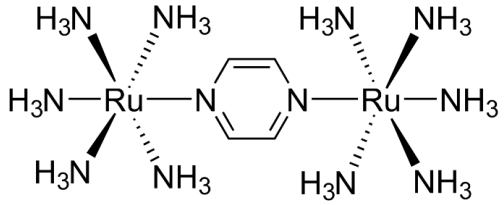

Figure 4.1. Structure of Creutz-Taube complex.

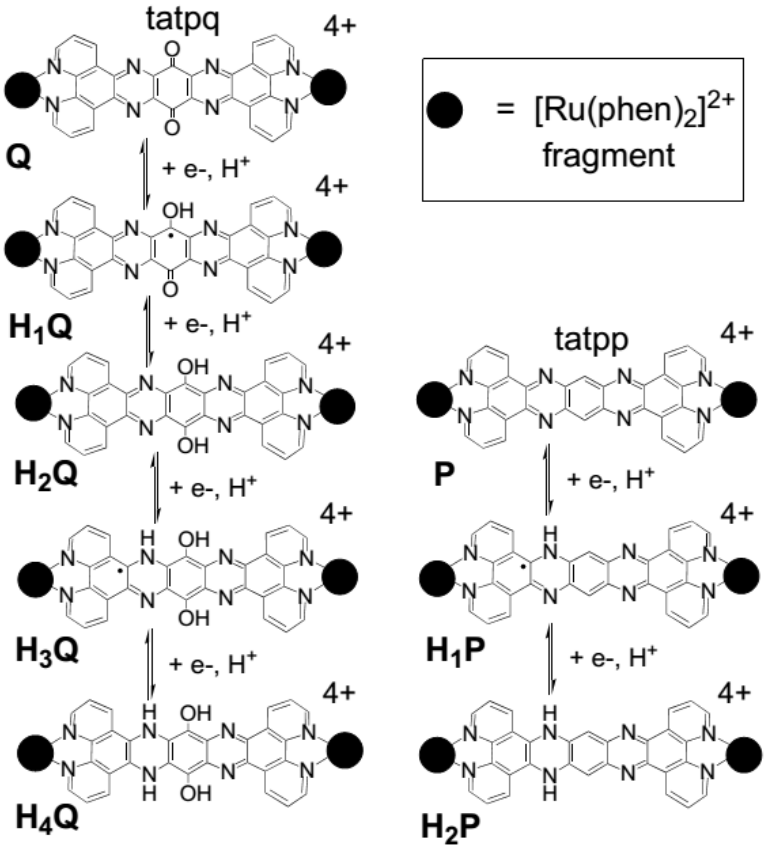

Figure 4.2. Photo-induced $4e^{-}$-$4H^{+}$ transfer of a dinuclear ruthenium complex.

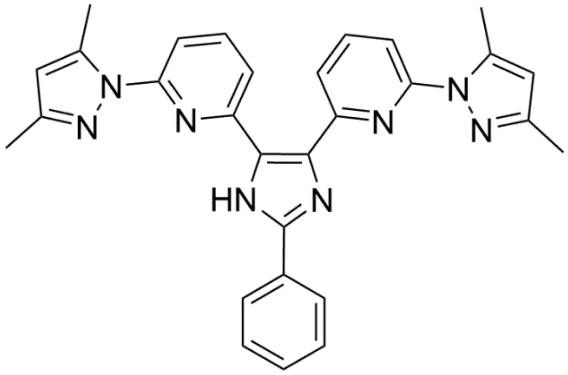

Figure 4.3. Polypyridine multidentate ligand, HL2.

4.2 Experiments

4.2.1. Synthesis of $[Ru^{II}_4(L2)_4](PF_6)_4$ ($[Ru^{II}_4]$)

An EtOH solution (5 mL) of $RuCl_3 \cdot nH_2O$ (12.6 mg, 0.06 mmol) was added to an EtOH solution (2 mL) of $AgBF_4$ (35.4 mg, 0.18 mmol) solution under dark conditions. After overnight stirring, chloride anions were removed as AgCl by filtration. An EtOH mixture (10 mL) of HL2 (58.4 mg, 0.12 mmol) and Et_3N (16.7 μL, 0.12 mmol) was added to the filtrate and the reaction solution was refluxed about 30 hours. Slow evaporation with an excess of NH_4PF_6 gave brown crystals of **$[Ru^{II}_4]$**.

4.2.2. X-ray crystallography

A crystal was mounted on a MiTeGen Dual-Thickness MicroLoops LD, and data was collected using a Bruker SMART APEX II CCD Systems with Mo-$K\alpha$ radiation at 100 K (λ = 0.71073 Å).

4.2.3. Physical properties

Electrochemical measurements were carried out in a standard one-compartment cell under nitrogen gas at room temperature with a glassy carbon (GC) working electrode, a platinum-wire counter electrode, and an SCE reference electrode using a BAS 620A electrochemical analyzer. The measurements were performed in acetonitrile with 0.1 M tetra-*n*-butylammonium hexafluorophosphate (*n*-Bu_4NPF_6) as the electrolyte. UV-Vis-NIR absorption spectra were recorded on a Shimadzu UV-3150 spectrometer. Controlled potential spectroscopy was measured in a 0.5 mm path length quartz cell under a nitrogen atmosphere. The Shimadzu UV-3150 spectrometer was used for the recording of controlled potential spectra, and the BAS 620A electrochemical analyzer was also used as a potentiostat. The measurements were performed in acetonitrile with 0.1 M tetra-*n*-butylammonium hexafluorophosphate (*n*-Bu_4NPF_6) as the supporting electrolyte. The electrolysis was performed in a three-electrode cell with a platinum-mesh working electrode, a platinum-wire counter electrode and a SCE reference electrode.

4.3 Results and Discussion

4.3.1. Molecular structure of $[Ru^{II}_4]$

The structure of **$[Ru^{II}_4]$** at 100 K is shown in Figure 4.4. Selected bond lengths and the crystallographic data for **$[Ru^{II}_4]$** are listed in Tables 4.1 and 4.2, respectively. **$[Ru^{II}_4]$** crystallized in the orthorhombic space group *P*nna. In **$[Ru^{II}_4]$**, four ruthenium ions were bound in a [2 x 2] grid like arrangement and two ligands coordinated to the ruthenium ions from the upper and lower sides. All ruthenium ions were in octahedral geometry. The bond lengths around the ruthenium ions and charge balance considerations suggest that all ruthenium ions are divalent. Ruthenium ions are bridged by the imidazolate group of the ligand ($L2^-$), and the interatomic distance of Ru1 and Ru2 is 6.359(3) - 6.365(3) Å. In the crystal, the complex cations make a layer along the *bc* plane parallel with the counter anion layer.

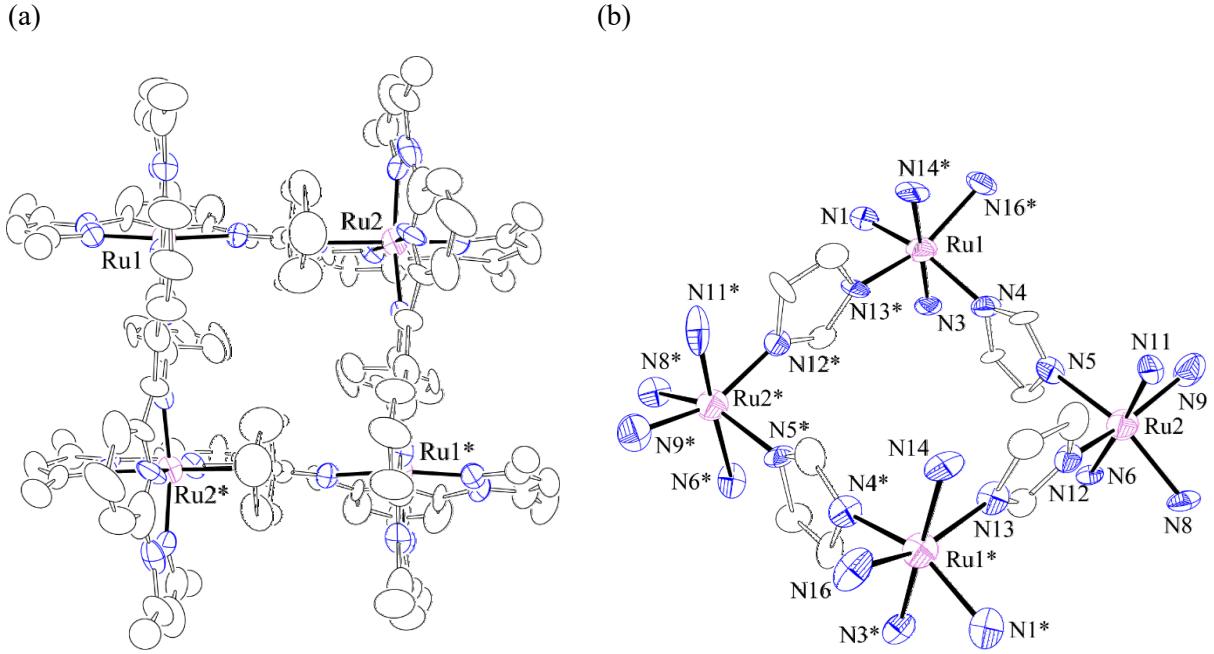

Figure 4.4. ORTEP diagram of **$[Ru^{II}_4]$** at 100 K. Thermal ellipsoids are at 30 % probability. Counter anions, hydrogen atoms and solvent molecules are omitted for clarity. (a) overall structure, and (b) core structure.

Table 4.1. Bond lengths (Å) for **$[Ru^{II}_4]$**.

Ru1-N4	2.04(2)	Ru2-N11	1.95(2)
Ru1-N14	2.06(2)	Ru2-N6	2.05(2)
Ru1-N1	2.06(2)	Ru2-N12	2.07(2)
Ru1-N3	2.07(1)	Ru2-N9	2.07(2)
Ru1-N13	2.07(2)	Ru2-N8	2.09(2)
Ru1-N16	2.10(2)	Ru2-N5	2.13(2)

Table 4.2. Crystallographic parameters for **[Ru^{II}_4]**.

	[Ru^{II}_4]
Chemical formula	$C_{118}H_{60}F_{24}N_{32}P_4Ru_4$
Formula weight	2910.14 g/mol
Temperature	100 K
Wavelength	0.71073 Å
Crystal system	Orthorhombic
Space group	*P*nna
a	24.749(7) Å
b	20.837(6) Å
c	21.709(6) Å
α	-
β	-
γ	-
Volume	11195.(5) $Å^3$
Z	4
Density (calculated)	1.727 g/cm^3
Absorption coefficient	0.695 mm^{-1}
***F*(000)**	5776
θ range for data collection	1.25 to 18.41°
Index ranges	$-21 \le h \le 21$
	$-18 \le k \le 11$
	$-19 \le l \le 19$
Reflections collected	26192
Independent reflections	4129 [R(int) = 0.1700]
Data / restraints / parameters	4129 / 0 / 832
Goodness-of-fit on F^2	1.129
Final *R* indices [$I>2\sigma(I)$]	R_1 = 0.0662,
	wR_2 = 0.1535
***R indices* (all data)**	R_1 = 0.1435
	wR_2 = 0.1981
Largest diff. peak and hole	0.485 and -0.365 $eÅ^{-3}$

4.3.2. Electrochemical properties

Cyclic voltammetry (CV) of **[Ru$^{II}_4$]** was conducted in acetonitrile solution (Figure 4.5) and the results are summarized in Table 4.3. **[Ru$^{II}_4$]** exhibited quasi-reversible four-step redox behavior at the redox potentials ($E_{1/2}$) of +0.61, +0.71, 0.92 and +1.06 V (vs. SCE), which are attributed solely to the ruthenium ions in the grid. The peak to peak separations (ΔE_p) were 42, 16, 89, and 31 mV, respectively. The open-circuit potential of **[Ru$^{II}_4$]** was +0.29 V. The observed four-step redox behavior is assigned as the divalent to trivalent oxidation peaks of the ruthenium ions. Thus, the redox processes are assigned as **[Ru$^{II}_3$Ru^{III}]/[Ru$^{II}_4$]**, **[Ru$^{II}_2$Ru$^{III}_2$]/[Ru$^{II}_3$Ru^{III}]**, **[Ru$^{III}_4$]/[Ru^{II}Ru$^{III}_3$]**. The valence state in the grid can be represented in Scheme 4.1. The comproportionation constants for **[Ru$^{II}_3$Ru^{III}]**, **[Ru$^{II}_2$Ru$^{III}_2$]** and **[Ru^{II}Ru$^{III}_3$]** species are calculated as K_c = 4.97 x 10, 3.44 x 10^3 and 1.93 x 10^2, respectively.

It can be expected that the *trans*-Ru$^{II}_2$-Ru$^{III}_2$ arrangement in **[Ru$^{II}_2$Ru$^{III}_2$]** is stabilized due to the electric repulsion between the ruthenium ions, similar to the behavior seen in the iron [2 x 2] grid.[11]

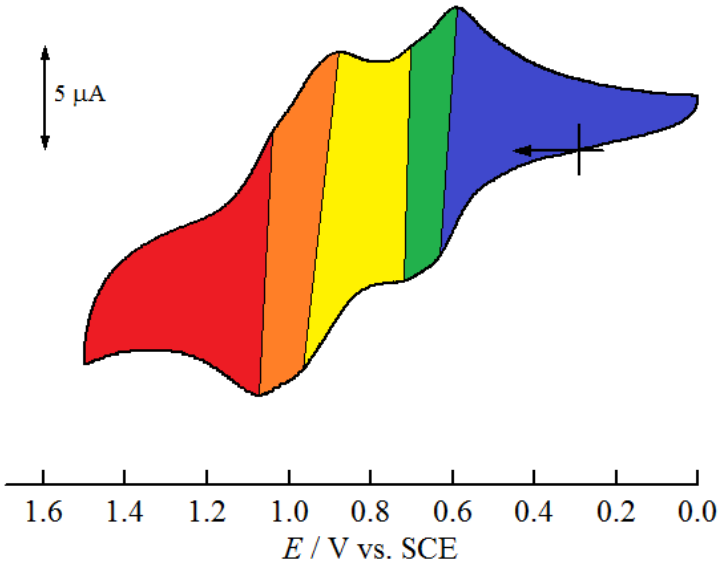

Figure 4.5. CV of **[Ru$^{II}_4$]** in CH_3CN in the presence of *n*-Bu_4NPF_6 (0.1 M) as an electrolyte.

Table 4.3. Cyclic voltammetry data.

E_{pa} a) (V)	E_{pc} a) (V)	$E_{1/2}$ a, b) (V)	ΔE_p a, c) (mV)
0.589	0.631	0.61	42
0.703	0.719	0.71	16
0.877	0.966	0.92	89
1.042	1.073	1.06	31

a) vs. SCE, b) $E_{1/2} = (E_{pa} + E_{pc})/2$, c) $\Delta E_p = E_{pa} - E_{pc}$

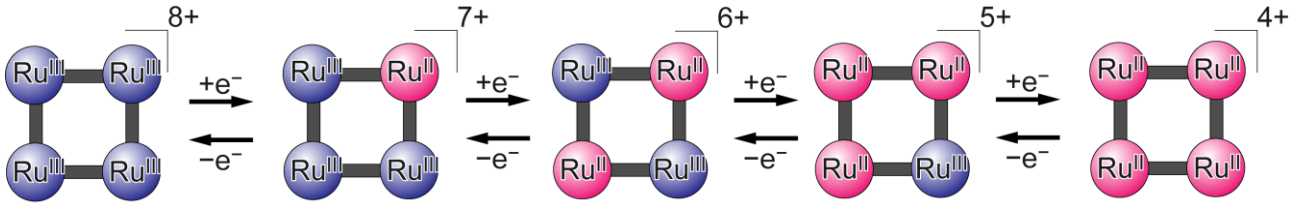

Scheme 4.1. Schematic drawings of the redox processes of **[Ru$^{II}_4$]**.

4.3.3. Controlled potential spectra

The controlled potential UV-Vis-NIR spectra of **[Ru$^{II}_4$]** were measured in acetonitrile, and the absorption bands associated with all accessible redox states were tracked (Figure 4.6). Two-electron oxidation from **[Ru$^{II}_4$]** to **[Ru$^{II}_2$Ru$^{III}_2$]** caused the Ru^{II} MLCT band (λ_{max} = 435 nm) to weaken, while new absorption bands appeared at 863 nm and 2459 nm assigned as Ru^{III} LMCT band and Ru^{II}-Ru^{III} IVCT band, respectively. Four-electron oxidation to **[Ru$^{III}_4$]** caused the IVCT band at 2459 nm to disappear while the LMCT band at 863 nm remained. Moreover, the peak at 543 nm was assigned to a LMCT band which appeared with the shift of π-π* band resulting from the reduction in π back donation.

From the controlled potential spectra, the Ru^{II}-Ru^{III} IVCT band was observed at $\tilde{\nu}_{max}$ = 3697.8 cm^{-1}, ε_{max} = 4709.8 M^{-1} cm^{-1}, $\Delta\tilde{\nu}_{1/2}$ = 4387.6 cm^{-1}. The delocalization parameters were calculated from Hush theory[12] as H_{ab} = 891 cm^{-1}, α^2 = 0.058.[13] Thus, two-electron oxidized state, **[Ru$^{II}_2$Ru$^{III}_2$]** is regarded as a Robin-Day class II electron delocalized mixed-valence complex.

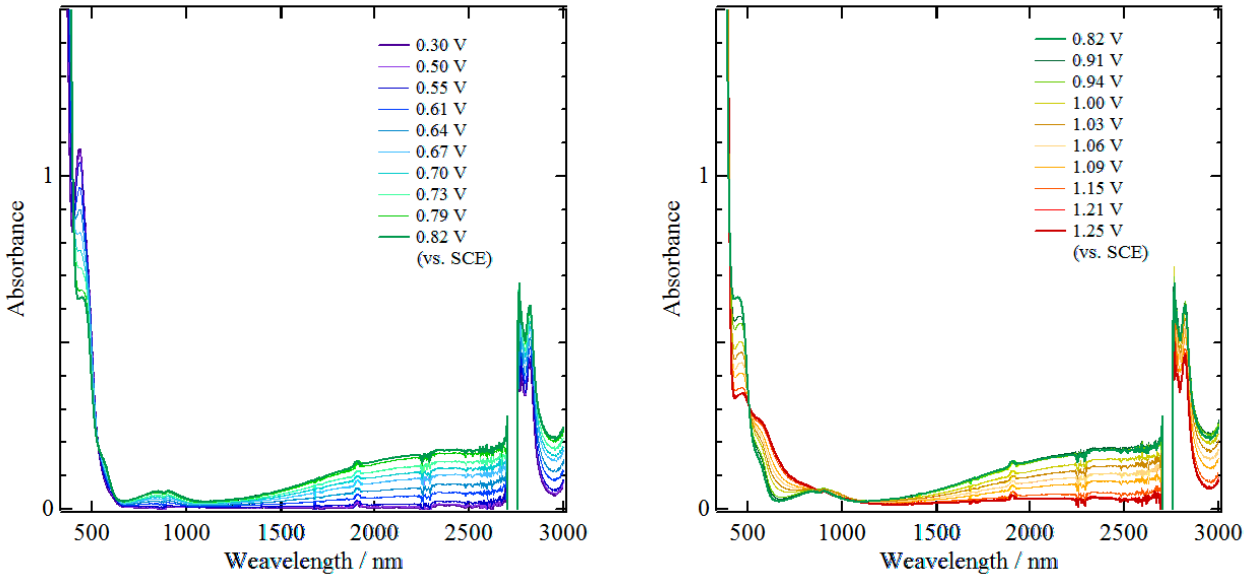

Figure 4.6. Controlled potential absorption spectra of **[Ru$^{II}_4$]** between (a) 0.30 V-0.82 V (vs. SCE) and (b) 0.82 V-1.25 V (vs. SCE) in acetonitrile at 293 K.

4.3.4. The mixed-valence in [Ru$_4$]

The mixed valence parameters were estimated from their controlled potential electronic spectra and CV measurements for the related compounds, and the values are summarized in Table 4.4. The iron [2 x 2] grid (**[Fe$^{II}_2$Fe$^{III}_2$]**[11]) showed a smaller H_{ab} value than that for **[Ru$^{II}_2$Ru$^{III}_2$]**, while the comproportionation constant for **[Fe$^{II}_2$Fe$^{III}_2$]** was higher than that **[Ru$^{II}_2$Ru$^{III}_2$]**. It should be noted that ruthenium(II) dπ orbitals are higher in energy than those of iron(II) ions, and the former is closer to the ligand π* orbitals. This is expected to lead to the stronger intermetallic interaction for ruthenium ions.

On the other hand, the imidazolate bridged dinuclear ruthenium complex, [{Ru(bpy)$_2$}$_2$(μ-dpi)] (bpy = 2,2′-Bipyridine, dpi = 4,5-di(2-pyridyl)imidazolate) showed stronger electronic interaction between mixed valence metal ions. This is due to the closer intermetallic distances (**[Ru$^{II}_2$Ru$^{III}_2$]**: 6.362 Å, [{Ru(bpy)$_2$}$_2$(μ-dpi)]: 6.160) and lower energy π* orbitals of the bridging ligands.

Table 4.4. the parameters relative to mixed-valence complexes.

complex	ν_{max} (cm^{-1})	$\Delta\nu_{1/2}$ (cm^{-1})	ε_{max} ($M^{-1}cm^{-1}$)	H_{ab} (cm^{-1})	α^2	ΔE (mV)	K_c	Class
[Ru$^{II}_2$Ru$^{III}_2$]	3697.9	4387.6	4709.8	890.74	0.058	210	3.4 x 10^3	II
[Fe$^{II}_2$Fe$^{III}_2$][7]	4060	1600	1400	320	0.006	290	9.8 x 10^4	II
[{Ru(bpy)$_2$}$_2$(μ-dpi)][14]	4475	2866	6630	2238	-	349	6.5 x 10^5	III
[{(NH$_3$)$_5$Ru}$_2$(μ-pym)][15]	7150	6000	41	143	-	150	340	II

4.4 Conclusion

The tetranuclear ruthenium [2 x 2] grid-type complex (**[Ru^{II}_4]**) was synthesized using a polypyridine multidentate ligand, HL2. CV showed four-step, four-electron pseudo-reversible redox behavior. The mixed valence state of **[Ru^{II}_4]** was studied by means of CV, and controlled potential UV-Vis-NIR spectra.

In comparison with the iron [2 x 2] grid-type complex[11], this ruthenium grid has stronger electronic interaction between the hetero-valent metal ions, and hence, a more delocalized electronic state. Such strong electronic interactions can be achieved by bridging ligand modifications based on frontier orbital designs. The present results might lead to the development of novel multi-bistable systems whose electronic states are controlled by external stimuli. Furthermore, a hetero-metal ruthenium/iron grid-type complex may show novel physical properties based on the correlation between mixed-valence states and iron spin crossover behavior.

[1] (a) M. H. Chisholm, and N. J. Patmore, *Acc. Chem. Res.*, **2007**, *40*, 19-27. (b) M. Abe, Y. Sasaki, T. Yamaguchi, and T. Ito, *Bull. Chem. Soc. Jpn.*, **1992**, *65*, 1585-1590. (c) M. Abe, Y. Sasaki, Y. Yamada, K. Tsukahara, S. Yano, T. Yamaguchi, M. Tominaga, I. Taniguchi, and T. Ito, *Inorg. Chem.*, **1996**, *35*, 6724-6734.
[2] T. Beissel, F. Birkelbach, E. Bill, T. Glaser, F. Kesting, C. Krebs, T. Weyhermüller, K. Wieghardt, C. Butzlaff, and A. X. Trautwein, *J. Am. Chem. Soc.*, **1996**, *118*, 12376-12390.
[3] (a) H. Okamoto, and M. Yamashita, *Bull. Chem. Jpn. Soc.*, **1998**, *71*, 2023-2039. (b) A. Kobayashi, and H. Kitagawa, *J. Am. Chem. Soc.*, **2006**, *128*, 12066-12067.
[4] S. B. Braun-Sand and O. Wiest, *J. Phys. Chem. A*, **2003**, *107*, 285-291.
[5] (a) M. Nihei, M. Ui, N. Hoshino, and H. Oshio, *Inorg. Chem.*, **2008**, *47*, 6106-6108. (b) V. C. Lau, L. A. Berben, and J. R. Long, *J. Am. Chem. Soc.*, **2002**, *124*, 6042-6043.
[6] (a) A. K. Diallo, C. Absalon, J. Ruiz, and D. Astruc, *J. Am. Chem. Soc.*, **2011**, *133*, 629-641. (b) S. T. Wilson, R. F. Bondurant, T. J. Meyer, and D. J. Salmon, *J. Am. Chem. Soc.*, **1975**, *97*, 2285-2287. (c) N. D. Jones, M. O. Wolf, and D. M. Giaquinta, *Organometallics*, **1997**, *16*, 1352-1354. (d) Y. Zhu, O. Clot, M. O. Wolf, and G. P. A. Yap, *J. Am. Chem. Soc.*, **1998**, *120*, 1812-1821. (e) B. Xi, G.-L. Xu, P. E. Fanwick, and T. Ren, *Organometallics*, **2009**, *28*, 2338-2341. (f) T. Ito, T. Hamaguchi, H. Nagino, T. Yamaguchi, H. Kido, I. S. Zavarine, T. Richmond, J. Washington, and C. P. Kubiak, *J. Am. Chem. Soc.*, **1999**, *121*, 4625-4632.
[7] (a) C. Creutz and H. Taube, *J. Am. Chem. Soc.*, **1969**, *91*, 3988-3989. (b) C. Creutz, H. Taube, *J. Am. Chem. Soc.*, **1973**, *95*, 1086-1084.
[8] (a) J. K. Beattie, N. S. Hush, P. R. Taylor, *Inorg. Chem.*, **1976**, *15*, 992-993. (b) N. S. Hush, *Chem. Phys.*, **1975**, 10, 361-366. (c) K. D. Demadis, C. M. Hartshorn, T. J. Meyer, *Chem. Rev.*, **2001**, *101*, 2655-2685.
[9] (a) M. Carano, P. Ceroni, C. Fontanesi, M. Marcaccio, F. Paolucci, C. Paradisi, and S. Roffia, *Electrochim. Acta*, **2001**, *46*, 3199-3206. (b) R. Konduri. H. Ye, F. M. MacDonnell, S. Serroni, S. Campagna, and K. Rajeshwar, *Angew. Chem. Int. Ed.*, **2002**, *41*, 3185-3187.
[10] (a) S. W. Gersten, G. J. Samuels, and T. J. Meyer, *J. Am. Chem. Soc.*, **1982**, *104*, 4029-4030. (b) J. J. Concepcion, J. W. Jurss, J. L. Templeton, and T. J. Meyer, *J. Am. Chem. Soc.*, **2008**, *130*, 16462-16463.
[11] T. Matsumoto, G. N. Newton, T. Shiga, S. Hayami, Y. Matsui, H. Okamoto, R. Kumai, Y. Murakami, and H. Oshio, *Nature Commun.*, **2014**, *5*, 3865/1-3865/8.
[12] (a) N. S. Hush, *Prog. Inorg. Chem.*, **1967**, *8*, 391-444. (b) C. Creutz, *Prog. Inorg. Chem.*, **1983**, *30*, 1-73.
[13] M. B. Robin and P. Day, *Adv. Inorg. Chem. Radiochem.*, **1967**, *10*, 247-422.
[14] J. W. Slater, D. M. D'Alessandro, F. R. Keene, and P. J. Steel, *Dalton Trans.*, **2006**, 1954-1962.
[15] D. E. Richardson and H. Taube, *J. Am. Chem. Soc.*, **1983**, *105*, 40-51.

List of Publications

CHAPTER 2

1) Pentanuclear and Octanuclear Manganese Helices
Hiroki Sato, Momoyo Yamaguchi, Tatsuya Onuki, Mao Noguchi, Graham N. Newton, T. Shiga, and Hiroki Oshio
Eur. J. Inorg. Chem., **2015**, 2193-2198.

2) Triple-stranded ferric helices: a π–π interaction-driven structural hierarchy of Fe_5, Fe_7, and Fe_{17} clusters
Takuya Shiga, Mao Noguchi, Hiroki Sato, Takuto Matsumoto, Graham N. Newton, and Hiroki Oshio
Dalton Trans., **2013**, *42*, 16185-16193.

CHAPTER 3

1) Multiredox Active [3 x 3] Copper Grids
Hiroki Sato, Lisa Miya, Kiyotaka Mitsumoto, Takuto Matsumoto, Takuya Shiga, Graham N. Newton, and Hiroki Oshio
Inorg. Chem., **2013**, *52*, 9714-9716.

Other Publications

1) Stepwise replacement of nickel with cobalt ions in a $[Ni_6]$ cluster
Graham N. Newton, Hiroki Sato, Takuya Shiga, and Hiroki Oshio
Dalton Trans., **2013**, *42*, 6701-6704.

2) A rectangular Ni–Fe cluster with unusual cyanide bridges
Christoph Krüger, Hiroki Sato, Takuto Matsumoto, Takuya Shiga, Graham N. Newton, Franz Renz, and Hiroki Oshio
Dalton Trans., **2012**, *41*, 11270-11272.

3) A series of tetranuclear [2×2] grid complexes derived from an asymmetric ligand: structural differences based on metal ion affinities
Takuya Shiga, Mao Noguchi, Takuto Matsumoto, Hiroki Sato, Hirotaka Tahira, Graham N. Newton, and Hiroki Oshio
Pure Appl. Chem., **2011**, *83*, 1721-1729.

ACKNOWLEDGEMENT

The research reported in this thesis has been performed under supervision of Prof. Hiroki Oshio. The author would like to express the deepest appreciation to Prof. Hiroki Oshio for appropriate suggestions, continue directions and encouragement. The author is very indebted to Dr. Masayuki Nihei, Dr. Takuya Shiga, and Dr. Graham Neil Newton for their kind advices and valuable discussion throughout this study. The author is grateful to Prof. Takahiko Kojima, Prof. Tatsuya Nabeshima, and Prof. Kazuya Saito for reviewing his thesis and many valuable suggestions. The author would like to thank all member of Oshio's laboratory for their friendship. Finally, the author would like to show my greatest appreciation to his family for financial support and encouragement.